INTERNATIONAL SCIENTIFIC JOURNAL

"MATERIAL SCIENCE"

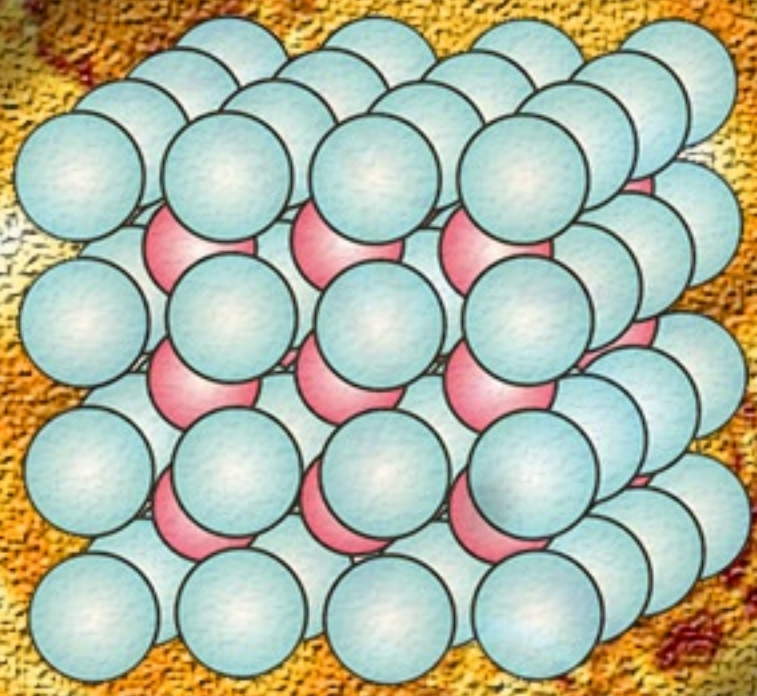

„NONEQUILIBRIUM PHASE TRANSFORMATIONS"

YEAR III, ISSUE 2/2017

ISSN PRINT 2367-749X
ISSN WEB 2534-8477

PUBLISHER: SCIENTICIC TECHNICAL UNION OF MECHANICAL ENGINEERING INDUSTRY 4.0

108 Rakovski str., 1000 Sofia, Bulgaria
tel./fax (+359 2) 986 22 40, tel. (+359 2) 987 72 90,
office@stumejournals.com, www.stumejournals.com

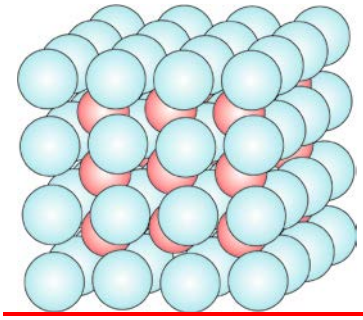

INTERNATIONAL SCIENTIFIC JOURNAL

MATERIALS SCIENCE. NON-EQUILIBRIUM PHASE TRANSFORMATIONS

PUBLISHER:

SCIENTIFIC TECHNICAL UNION OF MECHANICAL ENGINEERING

108, Rakovski Str., 1000 Sofia, Bulgaria
tel. (+359 2) 987 72 90,
tel./fax (+359 2) 986 22 40,
office@stumejournals.com

ISSN PRINT 2367-749X, ISSN WEB 2534-8477
YEAR III, ISSUE 2 / 2017

EDITORIAL BOARD

C O N T E N T S

INNOVATIVE DEVELOPMENTS OF THE INSITUTINS OF METALLURGICAL PROFILE OF THE RUSSIAN ACADEMY OF SCIENCES
Dr of Sci., Prof., Academician of Russian Academy of Sciencecs L.I. Leontiev 40

IMPROVEMENT OF OPTICAL CHARACTERISTICS OF COMPONENTS OF OPTOELECTRONIC DEVICES IN THE HARSH CONDITIONS OF THEIR FUNCTIONING BY USING ELECTRON BEAM TECHNOLOGY
PhD, Ass. Prof. Yacenko I. V. , d. Eng. Sc., Prof. Antoniuk V. C., d. Eng. Sc., Assoc. Professor Kyrychenko O. V. ,
d. Eng. Sc. Gordienko V. I., d. Eng. Sc. , Prof. Vashchenko V. A. 42

ADHESION STRENGTH EVALUATION OF CERAMIC COATINGS ON CAST AND SELECTIVE LASER MELTED Co-Cr DENTAL ALLOYS USING TENSILE SPECIMENS
Assoc. Prof. Ts. Dikova, Assoc. Prof. N.A. Dolgov, Assist. Prof. Dzh. Dzhendov, Assos. Prof. M. Simov 49

PECULIARITIES OF METALIZED SURFACES MODIFICATION OF SILICON ELEMENTS OF MICROELECTROMECHANICAL SYSTEMS WITH LOW-POWER ELECTRONIC FLOW
PhD. Bondarenko M., PhD Bondarenko I., Prof. dr. eng. Antonyuk V., Telezhynskyi D., Andriienko V. 53

DEVELOPMENT OF MATHEMATICAL MODELS OF THERMAL PLASMA PROCESSES
Prof. Frolov V. D.Sc., Ivanov D. Ph.D. 56

INVESSTIGATION OF MICROSTRUCTURAL AND MECHANICAL PROPERTIES OF DIFFERENT TYPE OF CASTINGS
Prof. Dr Cvetkovski. S. PhD. Prof. Dr Kozinakov. D. PhD 60

CORROSION BEHAVIOR OF COMMERCIALLY-PURE TITAMIUM WITH DIFFERENT MICROSTRUCTURES
Lead. Res., Dr. Semenov V.I., Prof., Dr. Huang S.-J., Prof. Tontchev N., Jun. Res. Valiev R.R., Jun. Res. Belov P.A.,
PhD Stud. Bogale D., PhD Stud. Wang A. 65

MICROALLOYED STEEL UNDER TENSION AND BENDING CONDITION
Doc. Ing. PhD. Mihaliková M., Ing. Lišková A., Ing. PhD. Elena Čižmárová E. 70

FINITE ELEMENT MODELING OF INCREMENTAL SHEET METAL FORMING OF ALUMINUM ALLOY AL 1100
Samad Nadimi Bavil Oliaei, PhD., Mahmoudreza Eivazzadeh, M.Sc., Samad Dadvandipour, PhD. 74

INNOVATIVE DEVELOPMENTS OF THE INSITUTINS OF METALLURGICAL PROFILE OF THE RUSSIAN ACADEMY OF SCIENCES

ИННОВАЦИОННЫЕ РАЗРАБОТКИ ИНСТИТУТОВ МЕТАЛЛУРГИЧЕСКОГО ПРОФИЛЯ РОССИЙСКОЙ АКАДЕМИИ НАУК

Dr of Sci., Prof., Academician of Russian Academy of Sciencecs L.I. Leontiev
Presidium RAS, Moscow, Russia

Abstract: *In the present work, examples of the successful development of new materials and technologies on the basis of fundamental research by members of the Russian Academy of Sciences are outlined. The topics include anticorrosive protective coatings based on ultrafine Zn powders; catalytic converters for vehicle exhaust gases; nanostructured stents for endovascular operations; and corrosion and wear resistant coatings and corresponding methods of plasma application. Methods have been developed for recycling of oily scale; for special electroproduction of steel for the power industry; synthesis of massive monocrystalline samples of transition metal nitrides and nanopowders of W, Pt, and Ti and their carbides and nitrides and others.*

KEYWORDS*:* NEW MATERIALS, TECHNOLOGIES, NANOPOWDERS, WEAR RESISTANT COATINGS

1. Introduction

In the present work, examples of the successful development of new materials and technologies on the basis of fundamental research by members of the Russian Academy of Sciences are outlined.

2. Examples of developments

Institute of Metallurgy of Ural Branch of the Russian Academy of Sciences, Yekaterinburg City (IM) founded the Innovative Technology Centre "Akademicheskii", with 10 000 m^2 total area. 12 Innovative Enterprises are working in this Centre.

Corrosion and wear-resistant coatings developed at IM, which are applied by plasma methods, have been introduced at enterprises including Yakutautotrans (Yakutsk), Tyumen'transgaz (Yugorsk), the Yekaterinburg and others [1–3].

Technology and equipment for production of shot and powders of ferrous and nonferrous metals. Technology was transferred to LLC "Invest-Ural" (Nizhny Tagil, Sverdlovsk region, according to license agreement (Fig. 1). Licencing to company "CTRP" (Chelyabinsk) is in process.

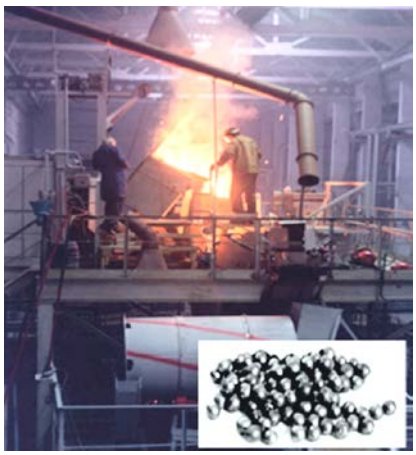

Fig. 1. *Production system for nonferrous and ferrous metal shot and powder at Akademicheskii Research and Development Center, Gran-Met Scientific Production Company.*

Researchers at Akademicheskii Research and Development Center and IM have created a fundamentally new waste-free system for the processing of molybdenum-bearing sulphide material [4, 5] (Fig.2). It is employed at a pilot plant producing rare earth elements, molybdenum trioxide, and calcium molybdate, with complete utilization of sulfur dioxide. Trial batches of molybdenum trioxide have been supplied to steel plants.

Fig.2 *Pilot plant to produce rare-earth elements, molybdenum trioxide, calcium molybdate and to make full utilization of sulfur dioxide*

Output production by plants of "Akademicheskii" engineering and technical center

- ✓ Antiwear additives: remetallizers of RiMET series (RiMET, RiMET-T, Motor HEALER), metal plaque lubricant Vympel;
- ✓ Ferromolybdenum FeMo, molybdenum trioxide MoO_3, calcium molybdate MoCa;
- ✓ Molded aluminum and brass pieces;
- ✓ Concentrates for precious metals obtaining;
- ✓ Precious metals (gold, silver, platinum);
- ✓ Combustion and heat-exchange equipment;
- ✓ Equipment for foamed concrete making;
- ✓ Metal beads with various typical sizes;
- ✓ Injection equipment for processing of metal melts.

At "Akademicheskii Research and Development Center (VMP Holding Company, associated with IM), on the basis of fundamental research into the evaporation and condensation of metals, a production technology was developed for ultrafine zinc powder and corresponding anticorrosion coatings [6, 7] (Fig.3). The coatings are used in oil and gas tanks and pipelines at the (Kuru space center (French Guyana) to protect the metal structures of the launch system for the Soyuz-ST rockets and in the construction of infrastructure (bridges, walkways, for example - Patriarchal bridge in Moscow, painting of load-bearing structures, constructions for the winter Olympics at Soch).

Fig. 32. *Production of metal powder by gas-phase synthesis and powder-based materials at "Akademicheskii" Research and Development Center: (a) production of zinc powder; (b) products based on bronze powder for the protection of frictional surfaces;(c) production of zinc-enriched paint.*

In collaboration with OOO Tekhnologii Tantalum, IM researchers have produced experimental batches of sintered tantalum nanopowder for use in tantalum capacitors by a new technology. The production conditions for these tantalum powders are consistent with the capabilities of OAO Elekond, which produces electrolytic high-voltage and chip capacitors. Nanopowders of other refractory metals and their carbides may be produced by this method, which is covered by two patents [8, 9]. It is possible to plate the powders so as to produce composite powders for additive technologies [10, 11].

A plasma system currently undergoing trials at IM could form the basis of a modern industrial version of the Korvet-6 plasma system equipped with a special system for powder preparation, with the possibility of maintaining the specified protocol in supersonic and hypersonic conditions [12, 13]. This system is intended for the application of external coatings at a rate of up to 30 kg/h (~150 m^3/h). Metals may be applied to paint coatings and even to an organic base (plastic, cardboard).

REFERENCES

1. Il'inykh, S.A., Kirnos, I.V., Krashaninin, V.A., and Gel'chinskii, B.R., Physical-chemical properties of coatings obtained by the method before and supersonic plasma spraying of metal powders and their compositions, Izv. VUZov, Poroshk. Metall. Funkts. Pokrytiya, 2015, no. 1, pp. 49–54.

2. Gel'chinskii, B.R., Il'inykh, S.A., Krashaninin, V.A., and Zalesova, O.L., Protection of metal products working in chemically aggressive conditions by creating combined corrosion_resistant coatings, in Mezhd. nauchno_tekhn. konf. "Novye materialy i tekhnologii glubokoi pererabotki syr'ya – osnova innovatsionnogo razvitiya ekonomiki Rossii," 25–28 iyunya 2012 g., Tezisy dokladov (Int. Sci._Tech. Conf. "New Materials and Technologies of Deep Processing of Raw Materials as the Basis for Innovative Development of Russian Economics," June 25–28, 2012, Abstracts of Papers), Moscow: Vseross. Inst. Avtom. Mashinostr., 2012.

3. Il'inykh, S.A., Gel'chinskii, B.R., Krashaninin, V.A., and Zalesova, O.L., Combined corrosion wear-resistant coating to protect the product from abrasive effects in chemically aggressive media, in *Tr. XXI Vseross. nauchno_tekhn. konf. s mezhd. Uchastiem "Bystrozakalennye materially i pokrytiya," 27–28 noyabrya 2012 g.*(Trans. XXI All_Russ. Sci._Tech. Conf. with Int. Participation "Rapidly Quenched Materials and Coatings," November 27–28, 2012), Moscow, 2012, pp. 74–78.

4. Kozhevnikov, G.N., Sitdikov, F.G., and Vodop'yanov, A.G., RU Patent 2296802, Byull. Izobret., 2007, no. 10.

5. Kozhevnikov, G.N., Sitdikov, F.G., and Vodop'yanov, A.G., RU Patent 2291110, Byull. Izobret., 2007, no. 1.

6. Leont'ev, L.I., Zalazinskii, G.G., Gel'chinskii, B.R., Zhuchkov, V.I., Lopatin, V.N., and Selivanov, E.N., Processes and equipment for dispersal of metals and injection of materials, Metallurgist (Moscow), 2009, vol. 53, no. 1, pp. 105–113.

7. Zolotukhina, L.V., Zapevalov, A.Y., Zhidovinova, S.V., Arefyev, I.G., and Gel'chinskii, B.R., The effect of super- and nanodispersed powders of zinc and copper alloys in plastic greases on the structure and triboengineering properties of steel surfaces, J. Frict. Wear, 2011, vol. 32, no. 2, pp. 107–112.

8. Kostylev, V.A., Leont'ev, L.I., Lisin, V.L., and Petrova, S.A., RU Patent 2397279, Byull. Izobret., 2010, no. 23.

9. Kostylev, V.A., Leont'ev, L.I., Lisin, V.L., and Petrova, S.A., RU Patent 93805, 2010.

10. Varaksin, A.V., Lisin, V.L., Kostylev, V.A., Leont'ev, L.I., Zakharov, R.G., and Petrova, S.A., Electrochemical production of nanoscale and ultrafine powders of metals and metal carbides, Butlerovskie Soobshch., 2014, vol. 37, no. 1, pp. 76–83.

11. Varaksin, A.V., Lisin, V.L., Kostylev, V.A., Leont'ev, L.I., Zakharov, R.G., and Petrova, S.A., Production of composite powder containing carbides of metals, Butlerovskie Soobshch., 2015, vol. 43, no. 8, pp. 102–110.

12. Kirnos, I.V., Chusov, S.A., Il'inykh, S.A., Gel'chinskii,B.R., Krashaninin, V.A., and Chachin, A.I., Design and creation of experimental stand for supersonic spraying of powdered materials, in Mater. XIV mezhd. Nauchno-tekhn. seminara, 24–28 fevralya 2014 g. (Proc. XIV Int. Sci. Tech. Seminar February 24–28, 2014), Kyiv: ATM Ukr., 2014, pp. 83–86.

13. Kirnos, I.V., Chusov, S.A., Gel'chinskii, B.R., Il'inykh, S.A., and Chachin, A.I., Problems and prospects of development of supersonic plasma spraying of composite materials, in Tr. VII mezhd. simp. po teoreticheskoi i prikladnoi plazmokhimii, Ples, Rossiya, 3 – 7 sentyabrya 2014 g. (Trans. VII Int. Symp. on The oretical and Applied Plasma Chemistry, Ples, Russia, September 3–7, 2014), Ivanovo: Ivanovsk. Gos. Khim. Tekhnol. Univ., 2014, pp. 2/

IMPROVEMENT OF OPTICAL CHARACTERISTICS OF COMPONENTS OF OPTOELECTRONIC DEVICES IN THE HARSH CONDITIONS OF THEIR FUNCTIONING BY USING ELECTRON BEAM TECHNOLOGY

УЛУЧШЕНИЕ ОПТИЧЕСКИХ ХАРАКТЕРИСТИК ЭЛЕМЕНТОВ ОПТИКО-ЭЛЕКТРОННЫХ ПРИБОРОВ В ЖЕСТКИХ УСЛОВИЯХ ИХ ФУНКЦИОНИРОВАНИЯ ПРИ ПОМОЩИ ЭЛЕКТРОННО-ЛУЧЕВОЙ ТЕХНОЛОГИИ

PhD, Associate Professor Yacenko I. V[1]. , d. Eng. Sc., Professor Antoniuk V. C.[2], d. Eng. Sc.,
Associate Professor Kyrychenko O. V.[3] , d. Eng. Sc. Gordienko V. I. [4] , d. Eng. Sc. , Professor Vashchenko V. A [1]
Cherkasy State technological university[1] , Ukraine, National Technical University of Ukraine " Kiev Polytechnic Institute name of Igor Sikorsky"[2], Cherkassy Institute of Fire Safety named after Heroes of Chornobyl[3],
Ukraine, State Enterprise scientific-production complex "Photoprylad"[4], Ukraine
E-mail: irina.yatsenko.79@mail.ru

Summary: *The optimal parameters of the ranges of the electron beam are found (heat density, velocity, displacement), within which there is improvement of the physical and mechanical properties of surface layers of optical elements: there is no formation of negative defects on their surfaces which become atomically smooth (residual microscopic ridges do not exceed 0.5… 1.5 nm); the microhardness of the surface increases, hardened layers are formed with compressive stresses. This leads to the reduction of the light scattering coefficient of surface layers of elements and increase of their coefficient of infrared radiation transmittance and, ultimately, to the improvement of metrological characteristics and reliability of devices under intensive external thermal action.*
KEYWORDS: OPTOELECTRONIC DEVICES, OPTICAL GLASS, OPTICAL CERAMICS, ELECTRON BEAM, OPTICAL CHARACTERISTICS

1. Introduction

The areas of application of modern opto-electronic devices, which constantly expand, acutely raise the problem of enhancing of their effective functioning under harsh conditions.

Optical elements of devices under these conditions are subjected to intense external influences (elevation of heating temperature, external pressures, percussive thermal actions under conditions of supersonic airflow and axial rotation of the optical elements (hemispherical fairings, flat visibility windows etc.)).

These external influences lead to the formation on the surface of optical elements and their surface layers of cracks, chips, undulating surfaces, which violate the flatness of the elements, and other negative defects. Thereat physical and mechanical properties of the surface layers of optical elements deteriorate, and, ultimately, their optical characteristics that affect the metrological characteristics and reliability of optoelectronic devices when they are functioning under the conditions of external thermal actions [1-4].

Existing methods of improving optical characteristics of optical-electronic devices (laser range finders of sighting complexes, laser medical devices, IR-homing and tracking devices, space and aerospace grade mirrors etc.) do not always provide their normative values, especially under harsh operating conditions.

New possibilities of improvement of optical characteristics of devices are opened due to the targeted change of the physico-mechanical and thermal properties of the surface layer of optical elements by modifying it. One of the effective methods of surface treatment of optical materials is the moving electron beam, which allows to modify the surface layers of optical elements by changing its physico-mechanical properties, which influence the optical characteristics of elements, metrological characteristics and reliability of devices [5 – 13].

Phenomena connected with the influence of technological parameters of forming and physico-mechanical characteristics of the surface layer of the optical elements of the devices are not fully studied and not systematized.

This determinates the relevance of development property management methods of working surfaces of optical elements of devices by using electron-beam finishing methods of optical elements that improve the physical and mechanical properties of surface layers, increasing their optical characteristics, and resistance to external thermal and mechanical influences, that allows to increase accuracy, extend measuring ranges and improve the reliability of the functioning of the devices under intensive external thermal actions.

Therefore, the aim of this work is to improve the optical characteristics of the elements of optoelectronic devices by their finish electron beam processing.

2. Characteristics of optical elements and research methods

For experimental studies modern methods of physico-chemical analysis were used [5, 14, 15]: methods of scanning electron microscopy (SEM) and transemission electron microscopy (TEM) to study surface structure and surface layers of optical elements, as well as determine the thickness of melted layers ; methods of atomic force microscopy (AFM) and micro identification by Vickers for the measurement of the residual voids on the surface of optical elements, as well as its microhardness; shooting techniques in x-rays of diffractometers DRONE 2.0 and DRONE 3.0 for measurements of thermal stresses in the surface layers of optical elements; methods with using spectrophotometers of close (λ = 0,76…2,5 μm) and far (λ = 2,5…25 μm) of IR ranges for the measurement of transmittance factor of IR waves of optical elements; contact methods (chromel-alumel thermocouples, temperature measurement range up to 1600 K) and contactless methods (photoresistors, temperature measurement range up to 1600 K) to measure the surface temperature of the optical elements.

For finish electron beam processing of surface layers of optical elements aiming to improve their physical and mechanical properties advanced installation was used (fig. 1) in the part of developed tooling for automated measurement and control of temperature of the surface, as well as sensing the electron beam, which is protected by patents (patent of Ukraine № 57551, patent of Ukraine № 91523) [5, 6].

The following empirical dependencies on density of thermal influence in its center from managed parameters of electron beam installation (relative accuracy of 5…8%) were found out in the result of the research on sensing the electron beam by the known method of rotary probe [5]:

$$F_n(x) = \sqrt{\frac{k_0(I_л,l)}{\pi}} \cdot \frac{I_л \cdot V_y}{B \cdot erf\left[b(I_л,l) \cdot \sqrt{k_0(I_л,l)}\right]}, \quad (1)$$

$$k_0(I_л,l) = 1{,}237 \cdot 10^7 - 6{,}587 \cdot 10^5 l - 3{,}725 \cdot 10^4 I_л + 1{,}518 \cdot 10^2 I_л l, \quad (2)$$

$$b(I_л,l) \frac{1{,}75}{\sqrt{k_0(I_л,l)}}, \quad (3)$$

where F_n – the density of the thermal influence in the center of the electron beam, Wt/m^2; k_0, $2b$ – concentration ratio (severity of the thermal pulse) and the thickness of the electron beam, m; $I_л$ – beam current, mA; V_y – external voltage, qt; l – the distance from the processed surface of the optical element, m. Found out, that for working ranges of changing of stated parameters of installation ($I_л$ = 50…300 mA, V_y = 6...8 qt, l = 0,04...0,08 m) the following variation ranges of energy caracteristics of electron beam are realized: k_0 = (0,5…5)·10^7 m^{-2}; $2b$ = (0,5…1,5)·10^{-3} m; F_n = 10^6…10^9 Wt/m^2. Herein beam travel speed changed within V = 0…0,1 m/s.

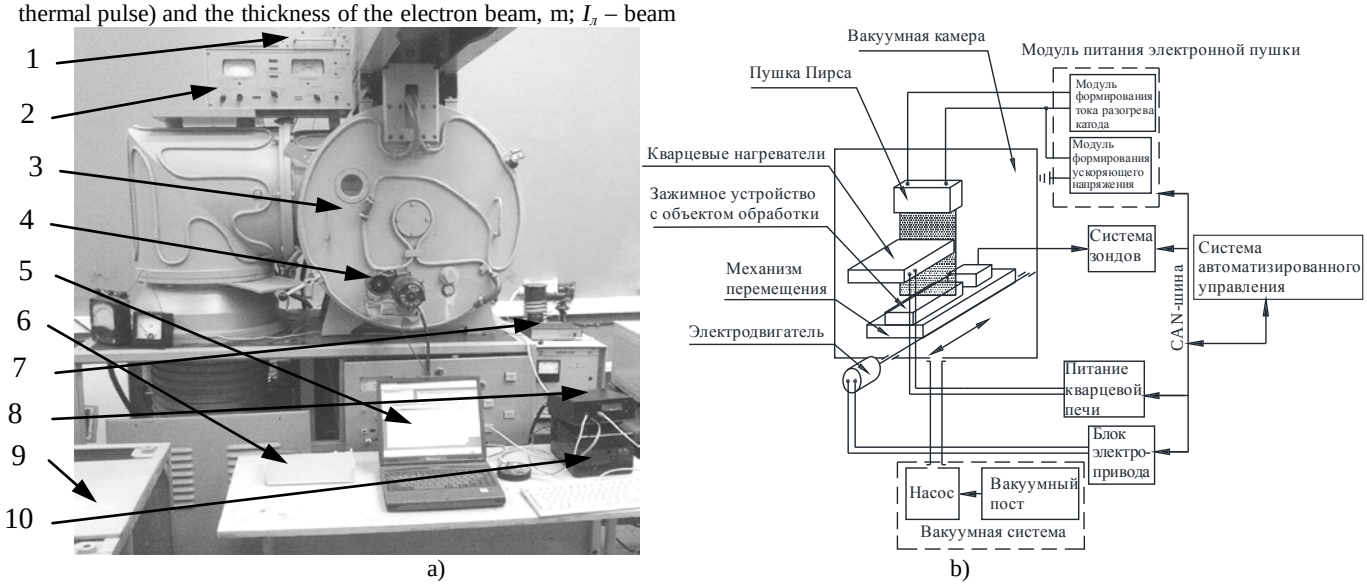

Fig. 1. Appearance (a) and schema (b) installations for the finishing electron-beam processing of optical elements, which improves the physical-mechanical properties of their surface layers: 1 – vacuum gauge magnetic locking VMB-8 (ВМБ-8) ; 2 – gauge ionized-thermocouple VIT-3(ВИТ-3); 3 – vacuum chamber; 4-electric mechanism of transfer mechanism of optical elements; 5 – PC control; 6 – modules of temperature measurement in the treatment area and sensing electronic flow; 7 – thermal management system of optical elements based on device RIF-101 (РИФ-101); 8 – central unit of automatic control system; 9 – power supply and control system of electronic gun of Pierce; 10 – electric motor control.

For pilot studies they used samples of optical elements of optoelectronic devices [14-18]: plane-parallel plates, rectangular, cylindrical and spherical elements elements, dual curvature elements from optical glass (K8, K108, K208, BK10 (БК10), TF110 (ТФ110)) and optical ceramics (KO1, KO2, KO3, KO5, KO12) (fig. 2).

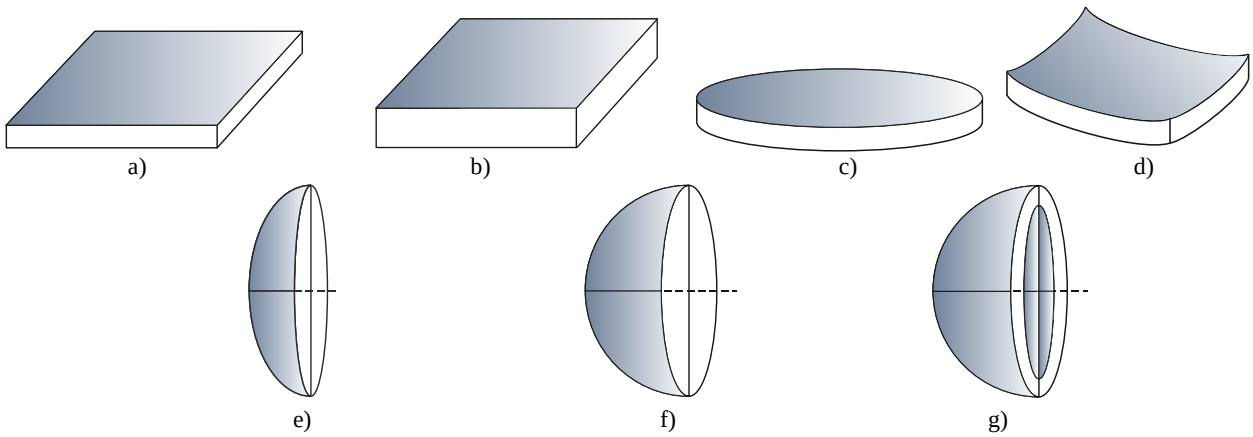

Fig. 2. General view of the optical elements of devices: flat-parallel plates (a), rectangular elements (b), disks (c), plates of double curvature (d) (substrates, light scattering screens in micro optics, integrated and fiber optics; elements of aerospace mirrors) and spherical elements (e) – (g) (lenses, hemispherical fairings).

3. Results and discussions

Optimal variation ranges of the parameters of the electron beam are defined: heat density F_n = 7·10^6...8·10^8 Wt/m^2 and velocity V = 5·10^{-3}... 5·10^{-2} m/s, within which there is improvement of parameters of surface layers of optical elements.

Electron-microscopic studies of surfaces of optical glass elements showed that after machining the most characteristic is the presence of microflaws – cracks up to 0.1 ... 0.7 μm deep, scratches with length up to 2 ... 5 μm, bubbles in size 10^{-3}...10^{-2} μm.

After the electron beam processing the bubble sizes (diameters) on the surface of elements reduction in 2 ... 4 times, while other wavinesses less than 1 ... 2 microns are not observed,

that means in electron beam processing the surfaces of elements as would be "cleaned up", tiny defects are eliminated.

In this case, when you increase the heat density F_n from $5 \cdot 10^6$ Wt/m^2 to $7 \cdot 10^7$ Wt/m^2 the area of specified defects decreases in 1,8...2,7 times.

Study of the skanogramms of grinding surfaces from elements' chipping before and after electron beam processing, show that in the first case the height of voids is 30 ...40 nm, while the latter is reduced to 0,5...1,2 nm.

Electron beam parameters influence on the height of residual voids is defined: increasing of heat density of electron beam F_n from 10^7 Wt/m^2 to $8{,}5 \cdot 10^7$ Wt/m^2 for the speed of its movement V = $8 \cdot 10^{-3}$...$5 \cdot 10^{-2}$ m/s, leads to a reduction of the height of the residual voids from 3...5 nm до 1,0...1,5 nm (fig. 3 under V = $5 \cdot 10^{-2}$ m/s (1); V = $8 \cdot 10^{-3}$ m/s (2)).

It has been established that the maximum thickness of melted layer h_m can reach values 250 ... 300 μm, that may exceed the maximum allowable quantities of voids h^* = 150...200 μm, which leads to violation of flatness and geometric shape of the optical element (fig. 4 for optical glass ВК10 (БК10) (1) and (2) TF110 (ТФ110) when heat density values F_n = $5 \cdot 10^8$ Wt/m^2 и $F_n = 3 \cdot 10^8$ Wt/m^2)).

In this case, the value h_m significantly depends on the F_n and its rate of travel V: increase of F_n from $7 \cdot 10^6$ Wt/m^2 to $8 \cdot 10^8$ Wt/m^2 leads to an increase in the thickness of melted layer from 25 μm up to 230 μm; increase in running speed of the electron beam from 10^{-3} m/s до 10^{-2} m/s leads already to reduction of the depth of melting from 200 μm to 30 μm.

Found out that the electron beam generated surface layers of elements from optical glass have chemically changed structure. Thus, the analysis of the structures of layers of elements from optical glass К8, К108, К208, ВК10 (БК10), TF 110(ТФ110) showed reduced concentrations of potassium (K) and sodium (Na), which is a consequence of the instability of oxides K_2O and Na_2O, by depth action of the electron beam.

It is also shown that the electron beam processing of elements from optical glass in the result of melting of their surface layers causes the orientation adjustment near the surface of the silicon-oxygen net of the glass, which becomes close to the structure of quartz glass. Mainly this is due to the removing of ions of K, Na, as well as other elements - modifiers under the conditions of the effect of high temperatures on the surface of the elements (up to 1500…1600 K). Ultimately, this improves heat resistance of elements from optical glass.

It is determined that the effect of the electron beam on the elements of optical ceramics (F_n = 10^6...$2 \cdot 10^7$ Wt/m^2, V = 10^{-3}...$2 \cdot 10^{-2}$ m/s) leads to the increase of the microhardness of its surface depending on the parameters of the electron beam: increase of F_n from 10^6 Wt/m^2 to $1{,}5 \cdot 10^7$ Wt/m^2 leads to the increase of microhardness of ceramics surface in 1,5...1,7 times, and decrease V from $1{,}5 \cdot 10^{-2}$ m/s до 10^{-3} m/s leads to the increase of microhardness of ceramics surface in 1,3... 1,4 times (fig. 5).

It is determined that the thickness of hardened layer (Δ), where there are major structural changes and the microhardness increases of the processed material for electron beam parameters changes in the ranges from 70...90 μm to 210...230 μm in thickness of processed units $4...6 \cdot 10^{-3}$ m (fig. 6).

The value Δ depends on the parameters of the electron beam: increase of F_n from 10^6 Wt/m^2 to $2 \cdot 10^7$ Wt/m^2 leads to an increase in the thickness of hardened layer in 1,8...2,6 times, while increasing of the ray speed from $1{,}5 \cdot 10^{-3}$ m/s до $2 \cdot 10^{-2}$ m/s reduces the thickness of hardened layer in 1,7...2,5 times.

It is shown that regardless of the nature of ceramics (КО1, КО2, КО3, КО12, КО5) in the surface layers of the elements that are handled by the electron beam, for the considered ranges of density changes of heat (up to 1, $5 \cdot 10^7$ Wt/m^2) and travel speed (up to $2 \cdot 10^{-2}$ ms) notable phase changes are not observed, but the increase of the size of the crystalline grains of the material takes place. By relative expansion of lines in radiographs it is found that almost irrespective of the crystallographic directions in crystal lattices of ceramics after electronic processing there occurs noticeable change of microdeformations and mosaic block sizes (table 1).

Data from table 1 shows that the effect of the electron beam to the surface of the optical element of optical ceramics leads to the increase of mosaic blocks and the reduction of the microdeffects of lattice: value of mosaic blocks from the original to processed by electron beam of optical elements increases by 3,9 times for elements from КО2, by 5,5 times for elements from the КО2, by 3,3 times for elements from КО12, by 4,7 times for items from КО3 and 7,7 times for elements with КО5 and the value of microdeffects decreases in 3,7 times for elements from КО1, in 5,4 times for elements from the КО2, in 4,2 times for elements from КО12, in 5,5times for elements from КО3 and 5,9 times for elements from КО5.

Thereat it is found that regardless of technological modes of processing (meanings of F_n and V for the observed ranges of their change) of elements from optical ceramic in all cases, there is an increase in the size of mosaic blocks and reduction of microdeffects of their crystal lattices, i.e. as a result of electronic processing there appear more coarse-grained surface layers with strains in crystalline lattices.

Resulting from the carried out researches it was determined (fig. 7, 8) that, as a result of electron beam processing of optical elements there is an increase in such an important optical characteristics that significantly affects the metrological characteristics of opto-electronic devices as transmittance factor of infrared radiation $k_\lambda(\lambda)$ (λ – wave length) in each range of infrared transparency of optical elements (table 2).

For the elements of optical glass К8 and ВК10 (БК10) the strongest increase of the coefficient k_λ (for 20 ... 30%) is observed for the range changes λ = 0,76…2 μm and λ = 3…4 μm. For elements from optical ceramics КО1, КО2 и КО5 (values k_λ for ceramic КО3 and КО12 remain unchanged) the strongest increase of the coefficient k_λ (up to 30 ... 40 %) is observed for λ = 0,76…4 μm.

It is determined that $\overline{\Delta\lambda} = \dfrac{\Delta\lambda^{обр}}{\Delta\lambda_0} \approx 1{,}08…1{,}15$ ($\Delta\lambda^{обр}$, $\Delta\lambda_0$ – for the elements, that are processed and not processed by electron beam электронным accordingly), so is observed small expansion range of infrared transparency of optical elements.

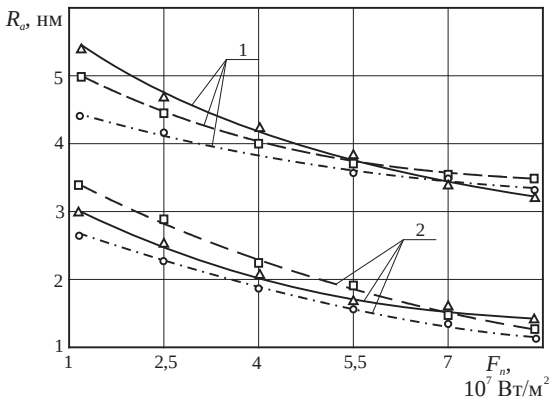

Fig.3. Height dependence of residual voids on the surface of elements of optical glass К8 (——), ТF110 (ТФ110) (– – –) and ВК10 (БК10) (– · – ·) from the density of heat effect of electron beam for its different travel speeds: $V = 5\cdot10^{-2}$ m/s (1); $V = 8\cdot10^{-3}$ m/s (2) (Δ, ○, □ – experimental data).

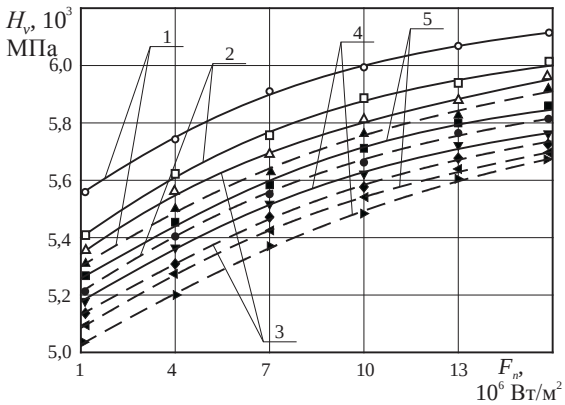

Fig.5. Dependence of microhardness surface of elements from optical ceramics КО12 (1), КО2 (2), КО1 (3), КО5 (4) и КО3 (5) at $V = 7\cdot10^{-3}$ m/s (———) и $V = 1{,}5\cdot10^{-2}$ m/s (– – –) from the density of heat effect of electron beam (Δ, ○, □, ▲, ■, ♦, ▼, ●, ►, ◄ – experimental data).

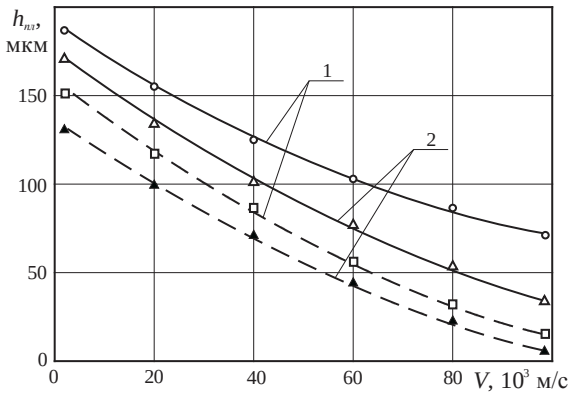

Fig. 4. The dependence of maximum thickness of melted layer in elements of optical glass ВК10 (БК10) (1) and TF110 (ТФ110) (2) at $F_n = 5\cdot10^8$ Wt/m^2 (——) and $F_n = 3\cdot10^8$ Wt/m^2 (– – –) from travelling speed of electron stream (Δ, ○, □, ▲ – experimental data).

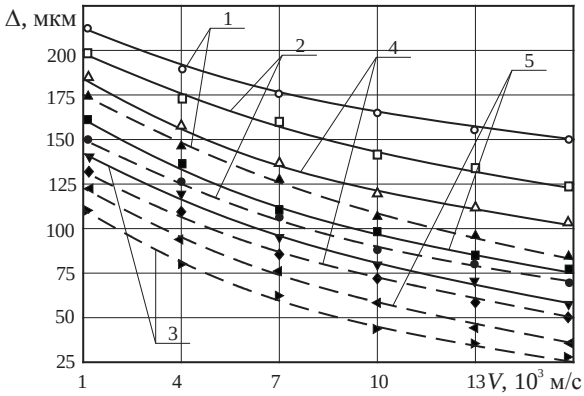

Fig. 6. The dependence of thickness toughened layers of elements from optical ceramics КО12 (1), КО2 (2), КО1 (3), КО3 (4) and КО5 (5) at $F_n = 1{,}5\cdot10^7$ Wt/m^2 (———) and $F_n = 2\cdot10^6$ Wt/m^2 (– – –) from the travelling speed of electron beam (Δ, ○, □, ▲, ■, ♦, ▼, ●, ►, ◄ – experimental data).

Table 1

The results of experimental data processing on the extension of lines on radiographs, mosaic block sizes (D) and change in the settings of a crystal lattice ($F_n = 3\cdot10^6$ Wt/m^2, $V = 3\cdot10^{-3}$ m/s)

Setting	Coarse probe			
	Physical expansion of the two lines		Block size D, Å	Change in the settings of a crystal lattice $\frac{\Delta d}{d}\cdot10^{-4}$
Ceramics	$\beta_1\cdot10^{-3}$, rad	$\beta_2\cdot10^{-3}$, rad		
КО1	1,472	1,734	1150	3,421
КО2	1,283	1,452	980	1,643
КО12	1,514	1,812	1240	3,810
КО3	1,120	1,320	890	1,225
КО5	1,132	1,289	760	1,117
Processed probe				
КО1	0,687	0,231	4430	0,873
КО2	0,321	0,108	5250	0,291
КО12	0,746	0,254	4110	0,992
КО3	0,224	0,986	4210	0,193
КО5	0,589	0,637	5850	0,987

Table 2

IR transparencies of optical elements $\Delta\lambda = \lambda_2 - \lambda_1$ at $H = 4\cdot10^{-3}$ m – for optical glass and $H = 10^{-2}$ m – for optical ceramics)

Element material / $\Delta\lambda$, μm	К8, ВК10	КО1	КО2	КО5
$\Delta\lambda = \lambda_2 - \lambda_1$, μm	5 – 0,76	7 – 2	12,5 – 2	8 – 0,76

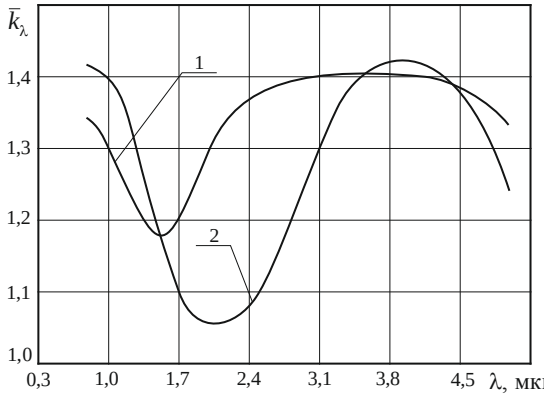

Fig. 7. The dependence of the relative coefficient of transmittance of infrared radiation through optical elements of glass K8 (1) and BK10 (БК10) (2) (density of flat layer of element H = $4\cdot10^{-3}$ m; T_0 = 300 K; $\bar{k}_\lambda = \dfrac{k_\lambda^{обр}}{k_{\lambda 0}}$, де $k_\lambda^{обр}$ – coefficient value k_λ after electron beam machining; $k_{\lambda 0}$ – its value before electron beam machining; F_n = $1{,}5\cdot10^7$ Wt/m^2, V = $7\cdot10^{-3}$ m/s) from the wave length.

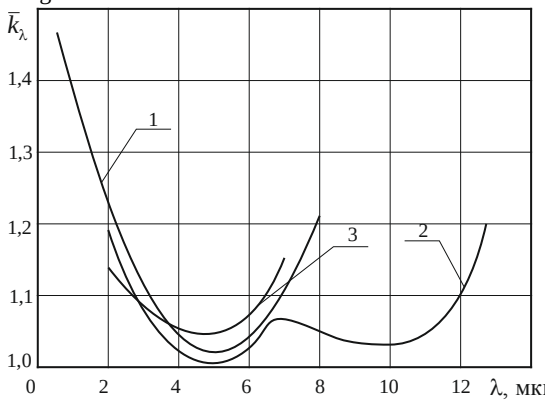

Fig. 8. The dependence of the relative coefficient of transmittance of infrared radiation by optical elements from ceramics KO5 (1), KO2 (2) and KO1 (3) (density of flat layer of element H = 10^{-2} m; T_0 = 300 K; F_n = 1, $5\cdot10^7$ Wt/m^2, V = $7\cdot10^{-3}$ m/s) from wave length.

Increase of transmittance of infrared radiation for elements from optical glass occurs as a result of reduction in the number and size of negative defects on the surface and in the surface layers (scratches, cracks, bumps, bubbles, depressions etc.) under the influence of the electron beam, which leads to their penetration. The consequence of this is a reduced number of residual voids h (nm) on their surfaces and increase of the depth of melting h_m (μm) up to the maximum permissible values of h^*. Therefore there is a one-to-one correspondence between the coefficient k_λ and such important physico-mechanical properties of the surface layers of the elements as h and h_m, which are presented in Fig. 9.

For items from optical ceramics the increase of k_λ occurs as a result of the structural changes of the surface layers (increasing sizes of mosaic blocks, layers become more compact, etc.), resulting in an increase of microhardness of their surfaces H_v and the formation of hardened layers having thickness Δ.

Therefore, there are also a one-to-one correspondence between the coefficient $\bar{k}_\lambda$ and parameters and H_v and Δ, dependencies between which are presented in Fig. 10.

It is determined (table 3) that after finishing electron beam processing of surfaces of optical elements of the devices out of beam parameters installed for optimal ranges of their use, deviations from the geometrical form from configured match those accepted in opto-electronic tool engineering. Thereat the surface purity of optical elements in the class P after electron beam processing increases up to one grade of purity (e.g. for photographic lenses from class VI to class V; for mirrors – with IV to III, etc.).

As a result of electron-beam processing of optical elements without reflow occurs homogenization of chemical composition of the chemical composition of hydrolysis products (dissolution of K_2O и Na_2O at depth effects of the electron beam up to 2...4 μm), which fill the defective surface layer, that remains after the standard mechanical processing, which leads to an improvement of the optical properties of the surface layers of the elements, namely to the reduction of their surface light scattering coefficient (wave length λ = 632,8 nm) (fig. 11).

In the result of the conducted research was outlined the influence of electron beam parameters to the coefficient k_c: at the increase of the parameter F_n from $7\cdot10^6$ Wt/m^2 to $3{,}9\cdot10^7$ Wt/m^2 and reduction of the parameter V from $5\cdot10^{-2}$ m/s to $5\cdot10^{-3}$ m/s the value k_c decreases in 1,3...1,5 times. In addition, reduction of the travelling speed of the electron beam leads to the increase of density influence of its thermal action in 1,2...1,3 times.

It is found out that the thermal action of the moving electron beam to the optical elements leads to their surface melting to a depth of 50 ... 200 μm, complete elimination of defective layers and reduction of micro relief of optical surfaces up to 0.5 ... 1 nm. The usage of masking and photo-and electron lithography enables create on the surface of optical elements functional micro-profiles in the form of grids, lattices, focusing lenses, and so on at a pitch of up to 100 μm.

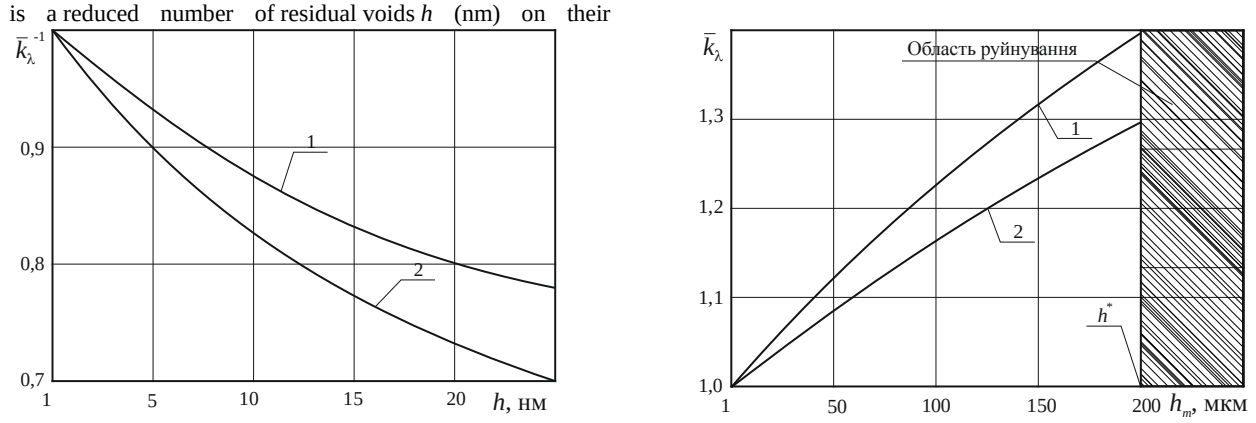

a) b)

Fig. 9. The influence of residual voids h (a) and thickness of melted layer h_m (б) to value $\bar{k}_\lambda$ for the elements from optical glass BK10 (БК10) (1) and K8 (2) (λ = 1,06 μm).

Thus, in the light of modern technology used in optic-electronic tool engineering, electron beam processing of optical elements is defined as potentially able to improve optical characteristics of elements of optoelectronic devices (increased transmittance of infrared radiation, light

scattering coefficient decrease of their surfaces, etc.), to increase their quality (compliance of geometric form with the configurated, increase of the purity and smoothness of the surface, etc.) as well as getting on the surface functional micro-profiles using electronic beams which can be used as the element base in microoptics, fiberoptics and integrated optics, optoelectronics, functional electronics etc.

In addition, the undeniable advantage of electron-beam technology is its environmental friendliness and ability to obtain microelements with improved physicomechanical properties and optical characteristics, the use of which in opto-electronic devices helps to improve their metrological characteristics and reliability under harsh operating conditions, on the common board from optical material in a single technological cycle.

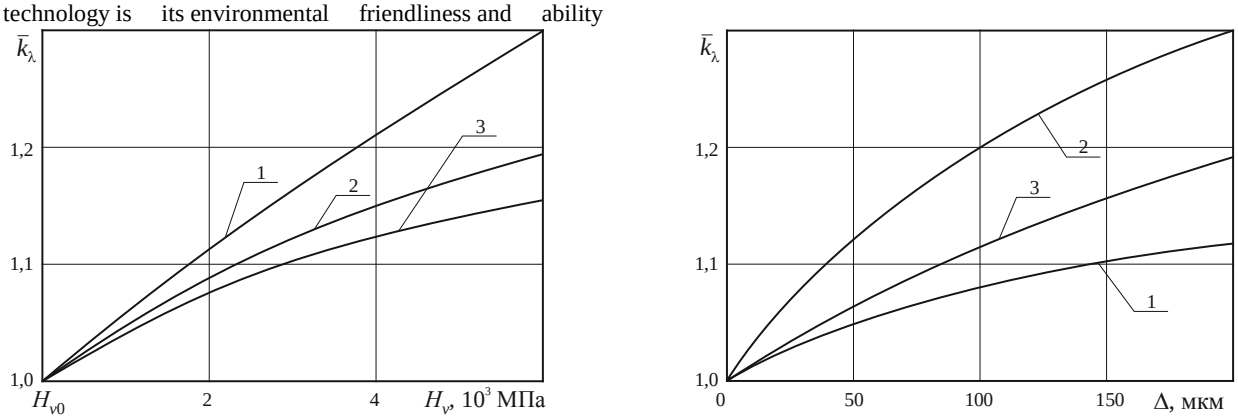

a) b)

Fig. 10. The influence of microhardness of a surface H_v (a) and the thickness of the strengthened layers Δ (б) to value $\bar{k}_\lambda$ for the elements from optical ceramics KO5 (1), KO2 (2) and KO1 (3) (λ = 1,06 μm).

Table 3

The tolerance value on quality optical elements which unprocessed and processed electron beam ($F_n = 7 \cdot 10^7$ Wt/m^2, $V = 2 \cdot 10^{-3}$ m/s)

Tolerances to the surfaces of Optical elements by / Elements of opto-electronic devices		Curvature N_0, $N^{обр}$		Form ΔN_0, $\Delta N^{обр}$		Cleanliness level P_0, $P^{обр}$	
		N_0	$N^{обр}$	ΔN_0	$\Delta N^{обр}$	P_0	$P^{обр}$
Lens	red dot sights and astronomical	1 – 3	3	0,2 – 0,3	0,2	VIII	VII
	aerial photography	1 – 3	3	0,1 – 0,5	0,5	VI	V
	photographic	3 – 5	5	0,3 – 0,5	0,3	VI	V
Viewers, loops		3 – 5	3	0,5 – 0,1	0,5	V	IV
Prisms	visual	0,5 – 1	0,5	0,1 – 0,3	0,1	III	II
	refracting	2 – 4	2	0,5 – 1	0,5	IV	III
Colour-filters behind and before the viewer		5 – 10	5	0,8 – 2	0,8	III	II
Mirrors		1 – 2	2	0,2 – 0,3	0,3	IV	III

Nota bene. The following names are taken: N_0, ΔN_0, P_0, $N^{обр}$, $\Delta N^{обр}$ и $P^{обр}$ – the values of the indicators of quality of raw optical elements and processed by electronic beam, respectively.

4. Conclusions

1. New experimental data is obtained on the influence of electron beam parameters on physico-mechanical properties of the surface layers of optical elements: optimal ranges of density of heat ray, and the speed of its movements are defined, within which there is maximum improvement (more than 3 ... 5 times) of basic properties (reduction of the area of negative defects on the surface, etc.), decrease of residual voids onn the surface, increase in its microhardness, formation of hardened layers, etc.) that allows to increase the stability of the external elements to thermal and mechanical influences, thus increasing the reliability of the devices.
2. For the first time it is determined, that by controlling the physical and mechanical properties of the surface layers of optical elements using a mobile electron beam it is possible to improve optical characteristics: increase the transmittance of infrared radiation and reduce the coefficient of light scattering of surfaces of elements) that allows to improve metrological characteristics of optoelectronic devices.
3. It is defined that after finish electron beam processing of the surfaces of optical elements of devices, variations in their geometric form from the specified match those accepted forms in optical-electronic tool engineering, and the purity of elements' surface in class P increases for lenses from VI to class V; for eyepieces from V to IV class; for prisms and mirrors – class IV to III, which increases the metrological characteristics and reliability of devices by their operation.
4. It is obtained that with the help of mobile electron beam by using masking, photo- and electronic lithography, it is possible to create on the surface of the optical elements the functional micro-profiles in the form of grids, lattices, microlens focusing with the pitch up to 100 μm, that can be used as element base in microptics, fiber optics, integrated optics and optoelectronics.

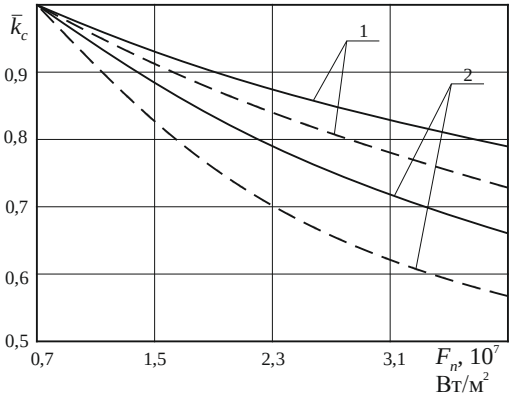

Fig. 11. Dependence of relative light scattering coefficient of working surfaces of optical elements from glass К108 (1) и ВК10 (2) the density of thermal action of electron beam for different speeds of its movement (the thickness of a flat layer of the element $H = 4 \cdot 10^{-3}$ m; $T_0 = 300$ K; $\bar{k}_c = \frac{k_c}{k_{c0}}$, where k_c – current value; k_{c0} – value k_c under $F_n = 7 \cdot 10^6$ Wt/m^2): —— – $V = 5 \cdot 10^{-2}$ m/s; – – – – $V = 5 \cdot 10^{-3}$ m/s.

5. References

1. Яценко И. В. Упреждение возможных разрушений оптических обтекателей ИК-приборов в условиях выстрела и полета // Ежемесячный научно-технический и производственный журнал “Наноинженерия”, 2015. – № 12(54). – С. 26 – 31. (Яценко И. В., Антонюк В. С., Ващенко В. А., Цыбулин В. В.)

2. Яценко І. В. Попередження можливих руйнувань оптичних елементів точного приладобудування в умовах зовнішніх термодій // Журнал нано- та електронної фізики, 2016. – т. 8. – № 1. – С. 01027 – 01032. (Яценко І. В., Антонюк В. С., Ващенко В. А., Цибулін В. В.)

3. Яценко І. В. Визначення критичних значень параметрів зовнішніх термодій на оптичні елементи точного приладобудування // Вісник Національного технічного університету України “Київський політехнічний інститут”, 2016. – № 51(1). – С. 71 – 75. (Яценко І. В., Антонюк В. С., Кириченко О. В., Ващенко В. А.)

4. Яценко І. В. Визначення критичних значень параметрів електронного променю при поверхневому оплавленні оптичних елементів точного приладобудування // Журнал нано- та електронної фізики, 2017. – т. – № 1. – С. . (Яценко І. В., Антонюк В. С., Ващенко В. А., Цибулін В. В.)

5. Ващенко В. А. Основи електронної обробки виробів з оптичних матеріалів. Монографія. – К.: Наукова думка, 2011. – 562 с. (Ващенко В. А., Яценко І. В., Лега Ю. Г, Кириченко О. В.)

6. Яценко І. В. Дослідження залежностей енергетичних характеристик СЕП від його керованих параметрів при впливі на вироби мікрооптики і інтегральної оптики // Сб. “Труды Одесского политехнического университета”, 2009. – вып. 2(32). – С. 143 – 149.

7. Yatsenko I. V. Experimental and statistical models of impact determination of the electron beam parameters on surface layers properties of optical elements in precision instruments building // “Pratsi. Odes’kyi politechnichnyi universytet”, 2016. – Issue 1(48). – P. 63 – 69.

8. Yatsenko I. Influence of parameters by electronic ray on properties of superficial layers of optical elements of exact instrument-making // International journal for science and innovations for the industry “Innovations in discrete productions”, ISSN 114-8907, YEAR III, ISSUE 1/2015, Sofia. – P. 13 – 15. (Yatsenko I., Antoniuk V., Bondarenko M., Vashchenko V.)

9. Yatsenko I. Improvement of technical and operational characteristics of devices with optical elements by preliminary electron beam treatment of their surface // International journal for science and innovations for the industry “Machines. Technologies. Materials”, ISSN 1313-0226, YEAR X, ISSUE 6/2016, Bulgaria. – P. 47 – 50. (Yatsenko I., Antoniuk V., Kiritchenko O., Vashchenko V.)

10. Yatsenko I. Increasing the resistance of precision instrument-making elements from optical glass to external thermo-influences by preliminary electron-beam processing of surfaces // International journal for science and innovations for the industry “Innovations in discrete productions” ISSN 1314-8907, YEAR IX, ISSUE 1/2016, Bulgaria. – P. 9 – 12. (Yatsenko I., Antoniuk V., Kiritchenko O., Vashchenko V., Tsybulin V.)

11. Yatsenko I. Improving the reliability instruments of measuring and thermal control of objects of different physical nature by the finish of electron beam processing surfaces of optical elements // International journal for science and innovations for the industry “Innovations in discrete productions” ISSN 1314-8907, YEAR X, ISSUE 2/2016, Bulgaria. – P. 11 – 14. (Yatsenko I., Antoniuk V., Kiritchenko O., Vashchenko V., Tsybulin V.)

12. Антонюк В. С. Підвищення фізико-механічних параметрів елементів з оптичних керамік фінішною електронно-променевою обробкою // Сучасні технології в машинобудуванні. Збірник наукових праць. – Харків: НТУ “ХПІ”, 2016. – Вип. 11. – С. 74 – 86. (Антонюк В. С., Яценко І. В., Кириченко О.В., Ващенко В. А.)

13. Яценко І. В. Покращення техніко-експлуатаційних характеристик приладів з оптичними елементами шляхом збільшення їх коефіцієнта пропускання ІЧ-випромінювання // Сб. Инженерия поверхности и реновации изделий. Материалы 16 Международной научно-технической конференции, 29 – 31 травня 2016 г, г. Затока – Київ: АТМ України. – С. 185 – 187. (Яценко І. В., Антонюк В. С., Кириченко О. В., Ващенко В. А.)

14. Яценко І. В. Підвищення метрологічних характеристик та надійності приладів для вимірювання та теплового контролю об’єктів різної фізичної природи шляхом електронно-променевої обробки їх оптичних елементів // Матеріали ІІ Всеукраїнської науково-практичної конференції “Приладобудування та метрологія: сучасні проблеми, тенденції розвитку”, 6 – 7 жовтня 2016 р., м. Луцьк. – С. 100 – 101. (Яценко І. В., Антонюк В. С., Гордієнко В. І., Кириченко О.В., Ващенко В. А.)

15. Окатов М. А. Справочник оптика-технолога. – СПб.: Политехника, 2004. – 679 с. (Окатов М. А., Антонов Э. А., Байгожин А. Б.)

16. Зверев В. А. Оптические материалы. Учебное пособик для конструкторов оптических систем и приборов. – СПб.: Издательство СП НИУИТМО, 2009. – 243 с. (Зверев В. А., Кривопустова Е. В., Точилина Т. В.)

17. ГОСТ 11141-84. Детали оптические. Классы чистоты поверхностей. Методы контроля.

18. Вильчинская С. С. Оптические материалы и технологии – Томск: Изд. Томского политехнического университета, 2011. – 107 с. (Вильчинская С. С., Лисицын В. М.)

.

ADHESION STRENGTH EVALUATION OF CERAMIC COATINGS ON CAST AND SELECTIVE LASER MELTED Co-Cr DENTAL ALLOYS USING TENSILE SPECIMENS

Assoc. Prof. Ts. Dikova[1a], Assoc. Prof. N.A. Dolgov[2b], Assist. Prof. Dzh. Dzhendov[1c], Assos. Prof. M. Simov[3d]

[1]Faculty of Dental Medicine, Medical University of Varna, 84 Tsar Osvoboditel Blvd, 9000 Varna, Bulgaria
[2]Pisarenko Institute for Problems of Strength, Nat. Ac. Sci. of Ukraine, 2 Timiryazevskaya Str., 01014 Kiev, Ukraine
[3]Medical College, Medical University of Varna, 84 Tsar Osvoboditel Blvd, 9000 Varna, Bulgaria
E-mail: [a]tsanka_dikova@abv.bg, [b]dna@ipp.kiev.ua, [c]jendo_jendov@abv.bg, [d]maksim_simov@abv.bg

***Abstract**: Studying the fracture characteristics of porcelain coatings plays a main role in selection of materials for metal-ceramic restorations. The aim of this work is to study the effect of the substrate manufacturing process on the adherence of the porcelain. The coatings of porcelain IPS.Inline (Ivoclar Vivadent) are fused onto dental Co-Cr alloys fabricated via casting (Biosil F) and Selective Laser Melting (SLM) (Co212-f). The adhesion strength of the ceramic coatings is studied under tensile load of flat specimens. The interfacial shear strength is determined using experimental results. The shear stress distributions in the metal-ceramic interface at the critical load are evaluated by analytical approach. It is established that the interfacial shear strength values of ceramic coating are 67.5 MPa for cast Biosil F alloy and 83.8 MPa for SLM Co212-f alloy. The higher shear strength of the porcelain to the SLM samples is due to the nearly two times higher surface roughness, which is reason for increasing both the mechanical and the chemical adhesion. The nature of the fracture of the ceramic coating on the Co-Cr alloys, produced by casting and SLM, is similar and is mixed adhesive–cohesive mode. The higher adhesion strength of the porcelain coating to the SLM dental alloy is a good precondition for the SLM application in production of metal-ceramic fixed partial dentures for areas with heavy loads*

Keywords: DENTAL Co-Cr ALLOYS, CASTING, SELECTIVE LASER MELTING, HARDNESS, ADHESION STRENGTH

1. Introduction

Metal ceramic dental construction consists of metal framework, covered with porcelain layers. For better aesthetics, the thickness of the porcelain layer should be higher - between 1.2-2.0 mm, while the metal framework should be thinner - about 0.5 mm [1]. That is why, the metal alloys, used for metal-ceramic dental restorations, have to possess high mechanical properties. The Co-Cr dental alloys are mostly used for manufacturing of metal frameworks due to their high hardness and strength, high corrosion and abrasive resistance. The properties of Co-Cr alloys depend on the microstructure, its morphology and composition, the γ-ε phases' ratio, the presence of carbides and intermetallic inclusions [2,3]. Cr and Mo are added for strengthening of the solid solution of Co-Cr alloys [4,5]. The chromium is a carbide-forming element and contributes to the formation of carbides in the microstructure, which lead to increase of the hardness and wear resistance. From the other hand, Cr additionally increases the corrosion resistance of Co-Cr alloys by forming of passive oxide layer on the surface of the detail.

The microstructure of metal alloys depends on the manufacturing process. Since the beginning of the last century, the lost-wax centrifugal casting is the technology mostly used for production of dental constructions from metal alloys. However, this technological process consists of many manual operations, thus leading to low dimensional accuracy and low quality of the restoration as a whole. The new CAD/CAM systems and additive technologies offer a number of advantages: digital design of the construction, simulation of the functions, fast and controllable manufacturing processes and no waste production from various materials [6]. Selective Laser Melting (SLM) is additive manufacturing process, characterizing with layer-by-layer building of the object from metal powder using laser beam. It is necessary to work with optimal technological regimes (laser power, layer's thickness, scanning speed and distance between individual melted traces) to obtain construction with high physical and mechanical properties. The high heating and cooling rates in the SLM process as well as the heating of the layers beneath the working surface above the transition temperatures lead to formation of the specific fine microstructure [7]. Meacock et al. [8] reported that the microstructure of biomedical Co-Cr-Mo alloy, produced by laser powder microdeposition, is homogeneous, comprised of fine cellular dendrites. The average hardness was 460 HV0.2, which is higher than the values obtained by the other fabrication process. Barucca et al. [9] investigated Co-Cr-Mo parts, produced by direct metal laser sintering. They established that microstructure consists of γ and ε phases. The ε phase is formed by athermal martensitic transformation and it is distributed as network of thin lamellae inside the γ phase. The higher hardness is attributed to the presence of the ε-lamellae grown on the $\{111\}_\gamma$ planes that restricts the dislocations movement in the γ phase.

In a metal-ceramic dental construction a good bond between the ceramic and metal is essential and it is achieved by the interactions of the ceramic with metal oxides on the surface of metal and by the roughness of the metal coping. There are two types of bonds on the metal-ceramic interface - chemical and mechanical [10,11]. The chemical bond is a result of chemisorption by diffusion between the surface oxides on the alloy and in the ceramic. The mechanical bond is carried out by the penetration of ceramic material into a rough metal surface, thus mechanically is interlocked with the metal. Therefore, the topography of a ceramic-metal interface plays an important role in the adhesion. The increased area, associated with a rougher interface, also provides larger area for chemical bonds to form. The minimum acceptable bond strength of metal-ceramic of 25 MPa is defined in the standard ISO 9693-1:2012 [12]. Most of the researchers confirm that the adhesion strength of the porcelain coating to the SLM Co-Cr dental alloys is comparable to that of the cast alloys and is higher than required in the standard [13-15]. Depending on the investigation method, the bond strength for the cast and the SLM Co-Cr dental alloys is 72.9 MPa and 67.0 MPa [14] or 54.17 MPa and 55.78 MPa accordingly [15]. Only Wang H. et al. [16] stated that there are statistically significant differences of the porcelain bond strength to the cast and SLM Co-Cr samples (37.7 ± 6.5 MPa and 46.8 ± 5.1 MPa respectively).

The SLM technological process is comparatively new and the data for the adhesion strength of the porcelain coating to the SLM Co-Cr dental alloys are insufficient and contradictory. The aim of the present paper is to study and evaluate the adhesion strength of ceramic coatings on cast and SLM Co-Cr dental alloys using tensile specimens.

2. Materials and methods

2.1. Samples manufacturing

Two groups of tensile test specimens (five samples in each group) were prepared by lost-wax casting and SLM using Co–Cr dental alloys. The first group was intended for tensile test, while the second – for adhesion strength evaluation. The cast samples were produced by centrifugal casting of Co-Cr alloy "Biosil" with chemical composition, given by the producer (Table 1). The SLM samples were fabricated directly from the virtual 3D models using SLM125 machine of the "SLM Solutions", Germany. The machine is equipped with continuous Nd:YAG laser which worked with power 100 W and laser spot diameter 0.2 mm. The metal powder of Co-Cr alloy Co212-f ASTM F75 (Table 1) was melted in layers with 0.03 mm thickness unless the desired construction was obtained. During manufacturing process, the laser at first scanned the outer contour of the layer of the first specimen's part; next, it hatched the area within the boundaries at an angle of 45° with a pitch of 0.13 mm. After that, it passed to the same layer of the next specimen's part, thus fabricating the whole layer. The SLM technological regime, recommended from the company producer was used. The specimens have a thickness of 2.2 mm for cast alloy and 2.07 mm for SLM.

Table 1.
Chemical composition of the alloys used.

Alloy	Chemical composition (wt %)							
	Co	Cr	Mo	Si	Mn	C	Fe	Ni
ASTM F75	Bal.	27–30	5–7	<1	<1	<0.35	<0.75	<0.5
Biosil, Degudent	64.8	28.5	5.3	0.5	0.5	0.4	–	–
SLM Co212-f ASTM F75	65.2	28.3	5.48	0.754	–	–	0.164	–

The both sides of the samples, intended for adhesion strength evaluation, were covered with 1.5 mm porcelain layer (IPS.Inline One, Ivoclar Vivadent) using the technology, recommended from the company producer of dental ceramic (Fig. 1). For better porcelain adhesion, the cast samples at first were sandblasted with SiO_2 particles (250 μm) and cleaned with steam jet. In order to maintain the original roughness, the SLM samples were only cleaned with steam jet. Five porcelain layers were put on the both sides of the samples: 1-st and 2-nd opaquers, 1-st and 2-nd dentcisal and a glaze. The samples were fired after each porcelain layer with regimes, given in Table 2.

Table 2.
Regimes of firing of different porcelain layers of one-layer metal-ceramic IPS.Inline One.

Ceramic layers	Firing temperature T (°C)	Closing time t (min)
1-st opaquer	930	6
2-nd opaquer	930	6
1-st dentcisal	910	4
2-nd dentcisal	900	4
Glaze	850	6

2.2. Surface roughness measurement

The arithmetic average of the surface profile R_a was measured in transverse and longitudinal directions of the samples with *Taylor Hobson Surtronik 3*. Five measurements in three areas of each direction on both sides of the samples were used for calculation the average value of R_a.

2.3. Adhesion strength evaluation

Uncoated specimens (pure substrate) and coated specimens were pulled uniaxially at room temperature using a testing machine (*FM*-1000) with a strain gauge attached to monitor the strain levels

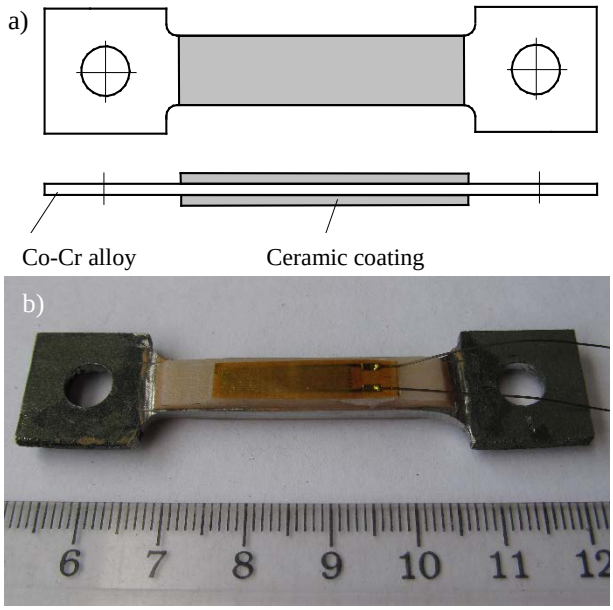

Fig. 1. *Scheme of the sample for evaluation the adhesion strength of ceramic coating to the Co-Cr alloys (a) and macroscopic photo of SLM tensile test specimen with porcelain coating and strain gage (b).*

(Fig. 1-b). The uniaxial tensile test allows the determination of Young's modulus of the porcelain layer and the substrate. The difference between the tensile response of coated specimen and uncoated one allows determining of the elastic modulus of the porcelain coating. Differences in Poisson's ratios between substrate and coating can be neglected [17]. The method for determining the elastic modulus of the coating is given in details in the previous investigations of Dolgov [18]. During the tensile test the coated specimens are subjected to an increasing tensile strain, causing cracking and delamination of the coating. Different analytical models exist to calculate the maximum interfacial shear strength [19]. In current study, the maximum interfacial shear strength τ (units of MPa) is calculated as [20]:

$$\tau = \frac{k\varepsilon}{1/(E_s H) + 1/(E_c h)} \tanh(kl), \quad (1)$$

where:

$$k = \sqrt{L \cdot \left(\frac{1}{E_s H} + \frac{1}{E_c h} \right)} \quad (2)$$

$$L = 2\left(\frac{G_s}{H} \cdot \frac{G_c}{h} \right) \Big/ \left(\frac{G_s}{H} + \frac{G_c}{h} \right) \quad (3)$$

E_s, E_c – elastic modulus of the substrate and the coating respectively; G_s, G_c – shear modulus of the substrate and the coating respectively; $2H$, h – thickness of the substrate and the coating respectively; ε – substrate strain at which occurs delamination of the coating; l – crack spacing in a fragmented coating.

The samples surface after manufacturing and adhesion testing was investigated by optical microscopies *Olympos SZ51* and *XJL-17A*.

3. Results obtained

3.1. Surface roughness

The data about the surface roughness of the samples, produced by casting and SLM, are given on Fig. 2. The surface of the SLM samples is nearly two times higher (R_a = 5.89 μm) comparing to the cast and sandblasted (R_a = 2.67 μm). The higher surface roughness

of the SLM alloy is due to the specific features of the manufacturing technology.

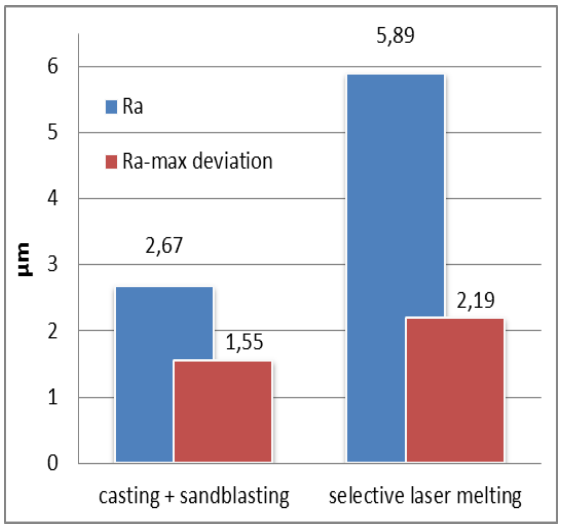

Fig. 2. *Arithmetic average of the surface profile R_a and its maximal deviation of Co-Cr samples produced by different technologies.*

3.2. Adhesion strength

Typical load versus strain graphs for samples with ceramic coating are shown in Fig. 3. The load–strain curves for the cast and SLM alloys is also shown for comparison.

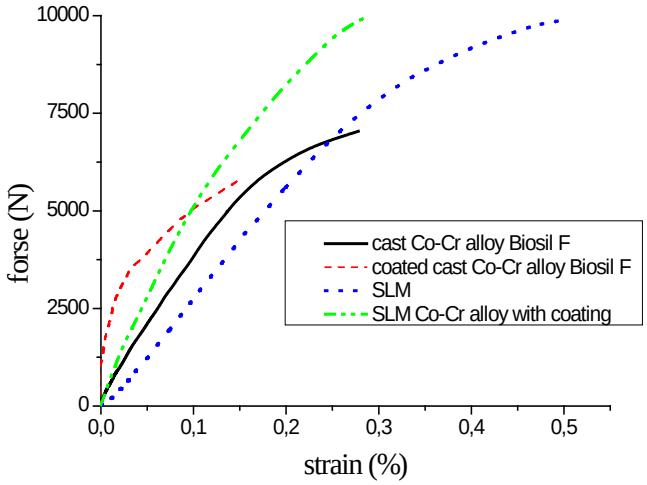

Fig. 3 *Typical load versus strain graphs for uncoated samples and samples with porcelain coatings.*

Due to the features of the casting process, the Co-Cr samples are characterized with the inhomogeneous microstructure, defining inhomogeneous properties. During the tensile test, with the load increase at first the network of multiple cracks appears in the coating, which is perpendicular to the direction of the applied force. After cracking of the coating, the delamination of the ceramic coating from the substrate occurs (Fig. 4). It should be noticed out that the coating is not completely detached from the cast alloy. There are islands of the porcelain on the surface of the sample. The uneven structure of the islands of the ceramic coating suggests uneven adhesion of the ceramics to the metal. After the test, the surface of the Biosil F alloy is cleaner than the surface of the SLM Co212-f alloy.

The fracture character of the SLM samples is similar. In the test process, after reaching the critical length of the crack spacing, the porcelain delamination occurs, followed by the adhesion failure of the coating from the substrate. However, these samples characterize with smaller cracks' spacing of the ceramic coating. A uniform network of lines with crack spacing of about 1 mm can be clearly seen. These are most likely opaque porcelain islands residues on the metal substrate. The network of lines, remained after the delamination of the ceramic coating, allows indirect evaluation of the adhesion strength. In the samples with smaller crack spacing, the adhesion strength is higher.

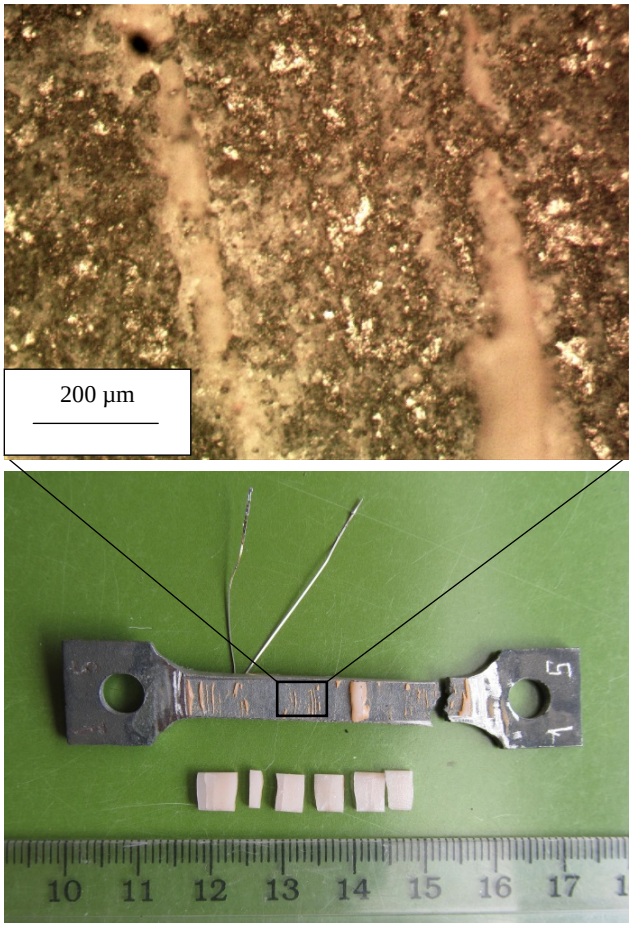

Fig. 4. *Cast sample with multiple cracking porcelain coating after tensile test.*

The results of the adhesion strength calculations and elastic characteristics of the metal-ceramic systems are given in Table 3. They show that the adhesion strength of the ceramic coating to the SLM Co212-f alloy is 23% higher than that of the ceramic to the cast Biosil F alloy (83,1 MPa and 67,5 MPa respectively), thus confirming the results of Lin Wu et al. [15] and Nan Xiang et al. [21].

Table 3.
Mean interfacial shear strength, elastic modulus and failure mode of metal-ceramic systems.

Substrate	Process	Modulus of elasticity *E* (GPa)		Interfacial shear strength τ, (MPa)	Coating failure mode
		Substrate	Coating		
Biosil F	Conventional casting	209	63	67,5	Cohesive or mixed cohesive-adhesive
Co212-f ASTM F75	SLM	213	72	83,1	Mixed cohesive-adhesive

4. Discussion

The bond between the ceramic and dental alloys is mainly two types – micro-mechanical and chemical [10,11,21]. Since the manufacturing technology of the porcelain coating to the cast and SLM dental alloys is the same, it is most probably that the stronger adhesion to the SLM substrate is due to the higher roughness of its surface. This hypothesis is confirmed by the surface examination of the samples after tensile testing. It is clearly seen that the non-melted alloy's powder acts as natural retentive beads. They retain a larger quantity of porcelain on the surface of the SLM sample, thus increasing the mechanical adhesion. Additionally, the higher surface roughness of the SLM specimens provides a larger surface area of ceramics interaction with the metal, which improves also the chemical adhesion. On the surface of the SLM detail, an intermediate layer is formed which consists of the elements of alloy and ceramic [15]. Since the chemical bond is decisive for the adhesion strength between the metal alloy and the ceramics, this boundary layer has a decisive impact on its enhancement. Ultimately, the adhesion strength of ceramic to the SLM Co-Cr alloy samples is significantly higher than that of the cast samples due to the increase in both the mechanical and the chemical components. Due to differences of the loading specimen configurations, used in the tensile testing and standard three-point bending (ISO 9693-1:2012), no direct comparison should be made of interface shear stress measuring by both tests.

5. Conclusion

The present study is focused on the evaluation of the adhesion strength of ceramic coating to CoCr alloy.

- Adhesion strength of a ceramic coating to a SLM Co212-f alloy is higher than the service requirements and 23% greater than that of ceramics to the Biosil F cast alloy (83.1 MPa and 67.5 MPa respectively). This is mainly due to the almost twice-higher roughness of the surface of the SLM samples, which leads to increase both mechanical and chemical components of the adhesion.

- The failure character of the ceramic coating to Co-Cr alloys, manufactured by casting and SLM, is similar and is of the adhesive-cohesive mode.

- The higher adhesion strength of the porcelain coating to the SLM Co-Cr dental alloys is a good prerequisite for their application in the production of metal-ceramic fixed partial dentures.

6. References

1.IPS Empress System, Instructions for use, Ivoclar Vivadent AG, (2006), 52 p.
2.Kurosu Sh., Nomura N., Chiba A., Effect of sigma phase in Co-29Cr-6Mo alloy on corrosion behavior in saline solution, Materials Transaction, 47/8 (2006) 1961 – 1964.
3.Yanjin Lu, Songquan Wu, Yiliang Gan et al., Investigation on the microstructure, mechanical property and corrosion behavior of the selective laser melted CoCrW alloy for dental application, Materials Science and Engineering C, 49 (2015) 517 – 525.
4.Bellefontaine G., The corrosion of CoCrMo alloys for biomedical applications, MSc thesis, School of Metallurgy and Materials, University of Birmingham, Jan 2010, 88p.
5.Podrrez-Radziszewska M., Haimann K., Dudzinski W., Morawska-Soltysik M., Characteristic of intermetallic phases in cast dental CoCrMo alloy, Archives of Foundry Engineering, 10/3 (2010), 51 – 59.
6.Dikova Ts., Dzhendov Dzh., Simov M., Katreva-Bozukova I., Angelova S., Pavlova D., Abadzhiev M., Tonchev T., Modern trends in the development of the technologies for production of dental constructions, Journal of IMAB, 21(4) Oct-Dec (2015), 974 – 981.
7.Dikova Ts., Dzhendov Dzh., Simov M., Microstructure and hardness of fixed dental prostheses manufactured by additive technologies, Journal of Achievements in Mechanical and Materials Engineering, 71, Issue 2, August (2015), 60 – 69.
8.Meacock C.G., Vilar R., Structure and properties of a biomedical Co–Cr–Mo alloy produced by laser powder microdeposition, J. Laser Appl. 21 (2009) 88 – 95.
9.Barucca G., Santecchia E., Majni G. et al. Structural characterization of biomedical Co-Cr-Mo components produced by direct metal laser sintering, Materials Science and Engineering C, 48 (2015) 263 – 269.
10.Anusavice K.J. Philips' Science of Dental Materials, Elsevier (2003), 806 p.
11.Dikova Ts., Dental Materials Science, Lectures and laboratory classes notes, Part II, MU-Varna, Varna (2014), 150 p.
12. ISO 9693-1 : 2012 Dentistry – Compatibility testing – Part 1: Metal-ceramic systems.
13.Li J., Chen C., Liao J., et al., Bond strengths of porcelain to cobalt-chromium alloys made by casting, milling, and selective laser melting. J. Prosthet Dent. Forthcoming. DOI: 10.1016/j.prosdent.2016.11.001.
14.Akova T., Ucar Y., Tukay A., et al., Comparison of the bond strength of laser-sintered and cast base metal dental alloys to porcelain. Dent. Mater., 24 (2008), 1400 – 1404.
15.Wu L., Zhu H., Gai X., Wang Y., Evaluation of the mechanical properties and porcelain bond strength of cobalt-chromium dental alloy fabricated by selective laser melting. J. Prosthet. Dent., 111 **(**2014), 51 – 55.
16.Wang H., Feng Q., Li N., Xu S., Evaluation of metal-ceramic bond characteristics of three dental Co-Cr alloys prepared with different fabrication techniques. J. Prosthet. Dent., 116 **(**2016), 916 – 923.
17.Dolgov N.A., Lyashenko B.A., Effect of Poisson's ratio on the limiting stressed state of a coating. Strength of materials, 34 (1) (2002), 49 – 53.
18.Dolgov N.A., Method for determining the modulus of elasticity for gas thermal spray coatings. Powder metallurgy and metal ceramics, 43 (7 – 8) (2004), 423 – 428.
19.Dolgov N.A., Analytical methods to determine the stress state in the substrate–coating system under mechanical loads. Strength of materials, 48 (5) (2016), 658 – 667.
20.Уманский Э.С., Ляшенко Б.А., Условия адгезионной и когезионной равнопрочности жаростойких покрытий. Космические исследования на Украине, 6 (1975), 58 – 64.
21.Nan Xiang, Xian-Zhen Xin, Jie Chen, Bin Wei, Metal–ceramic bond strength of Co–Cr alloy fabricated by selective laser melting. Journal of Dentistry, 40 (2012) 453 – 457.

PECULIARITIES OF METALIZED SURFACES MODIFICATION OF SILICON ELEMENTS OF MICROELECTROMECHANICAL SYSTEMS WITH LOW-POWER ELECTRONIC FLOW

ОСОБЕННОСТИ МОДИФИЦИРОВАНИЯ МЕТАЛЛИЗИРОВАННЫХ ПОВЕРХНОСТЕЙ КРЕМНИЕВЫХ ЭЛЕМЕНТОВ МИКРОЭЛЕКТРОМЕХАНИЧЕСКИХ СИСТЕМ НИЗКОЭНЕРГЕТИЧЕСКИМ ЭЛЕКТРОННЫМ ПОТОКОМ

PhD. Bondarenko M.[1], PhD Bondarenko I.[1], Prof. dr. eng. Antonyuk V.[2], Telezhynskyi D.[3], Andriienko V.[4]
Faculty of Electronically Technologies[1], Department of International Relations [3] – Cherkassy State Technological University, Ukraine
Faculty of instrument-making [2] – National Technical University of Ukraine «Ihor Sikorsky Kyiv Polytechnic Institute», Ukraine
Faculty of Information Technologies and Systems[4] – Cherkassy State Technological University, Ukraine

Abstract: *The practical possibility of the atomic force microscopy method to evaluate uniformity of thin metal coatings on silicon wafers after electronic processing has been shown in the paper. It is established that after processing of metallized surfaces of silicon plates Kp0 by an electronic flow of continuous form, the microroughness decreases in 10-15 times and the* Adhesive *strength increases in 1.8-2 times. At the same time, it is noted that the surface of metal coatings on silicon after electronic processing has a more homogeneous structure and released from microdefects, unlike metallized coatings without electronic processing.*

KEYWORDS: *MICROELECTROMECHANICAL SYSTEMS (MEMS), SILICON PLATES, METALIZED SURFACES, ELECTRON- BEAM MODIFICATION, ATOMIC-FORCE MICROSCOPY*

1. Introduction

Structural features, thickness and microrelief of metallized coatings on silicon elements of microelectromechanical systems (MEMS) determine their performance characteristics, depending on the method of production. A device for electron beam polishing of wares has been described in the paper [1], which makes it possible to realize a combined method: the application of metal coatings and the subsequent processing of these coatings by a continuous electronic flow.

In modern instrument making for the MEMS wares production, thin (up to 1 mkm) metal coatings on silicon are widely used. Such coatings, obtained, in particular, by evaporation in vacuum, have properties (high adhesion strength, reflective power, etc.), which allow them to be used as functional wear-resistant coatings in precision instrument making [2].

The method for the production and the microrelief features of thin coatings determine the performance characteristics of MEMS elements linked with the instability of their properties over time. As shown in works [3, 4], the reasons for such instability are the dimensional effects (inequality of the coating thickness, surface structure) and the operating conditions of these elements (aggressiveness of the external environment, time and operating temperature, mechanical interaction with other elements).

The possibility of metallized surfaces modification by an electronic flow of the continuous form has been shown in the work [5]. Besides, the technical and operational, chemical and tribometric properties of coatings on silicon substrates have been improved.

At the same time, the method of atomic force microscopy possesses essential advantages in the research of the microrelief of metallized surfaces modified by an electronic flow, namely: high accuracy of fixed microroughnesses of the surface (up to units of angstroms) and sensitivity of the measuring console ($\approx 10^{-8}$ N), and this method refers to non-destructive research methods that do not require preliminary preparation of the material of the research and pretend to the rapid research.

The aim of the work is the study using atomic force microscopy of the microrelief of thin metal coatings on silicon plates modified by an electronic flow, whose surfaces are used in precision instruments industry for the production of MEMS elements.

2. Experimental method

The plane-parallel plates of circular form (20 mm in diameter and 0.5 mm in thickness) made of silicon Kp0 were metallized by aluminum.

Metallization and electronic modification was carried out on a special laboratory machine (Educational and Scientific Center "Micronanotechnologies and Equipment", ChSTU, Cherkassy), containing the evaporator and Pierce electronic gun.

The silicon plate, preheated to a temperature of 630 K, by using of revolving traveling mechanism it was located in a vacuum chamber above the evaporator unit, where for 5-8 sec the metallization of its surface was carried out under the following modes: the heating current of the evaporator is I = 115-125 A; voltage on the evaporator is U = 20-22 V; distance from the evaporator to the plate surface is h = 120 mm.

After the ending of metallization process, the plate moved unceasing over the electronic gun. At the same time, a low-energy electronic flow of continuous form (width 3.0 mm, length 60.0 mm) affected the metallized surface. Electronic processing was carried out at the following modes: accelerating voltage is 3.5 ... 4.0 kV; the current of the electronic flow is 175 ... 200 mA; the current of cathode heating is 14.5 A; The electron flow rate is 4.5 ... 5.0 cm / s; the distance from the anode of the electronic gun to the working surface is 40 mm; single pass processing.

The microgeometry of the surface of the deposited coatings and the "coating-plate" boundary was investigated by atomic force microscopy method using the "NT-206V" instrument, (manufacturer:
ALC "Microtestmashiny", Belarus) with silicon probes "Ultrasharp CSC12", microposition system and built-in optical long-focus Logitech microscope.

3. Results and discussion

As a result of the conducted researches it is established that the gold coverings on silicon plates received by evaporation in vacuum are non-uniform, have the increased porosity and contain microdefects of a surface (cracks, points and etc.), Fig. 1.

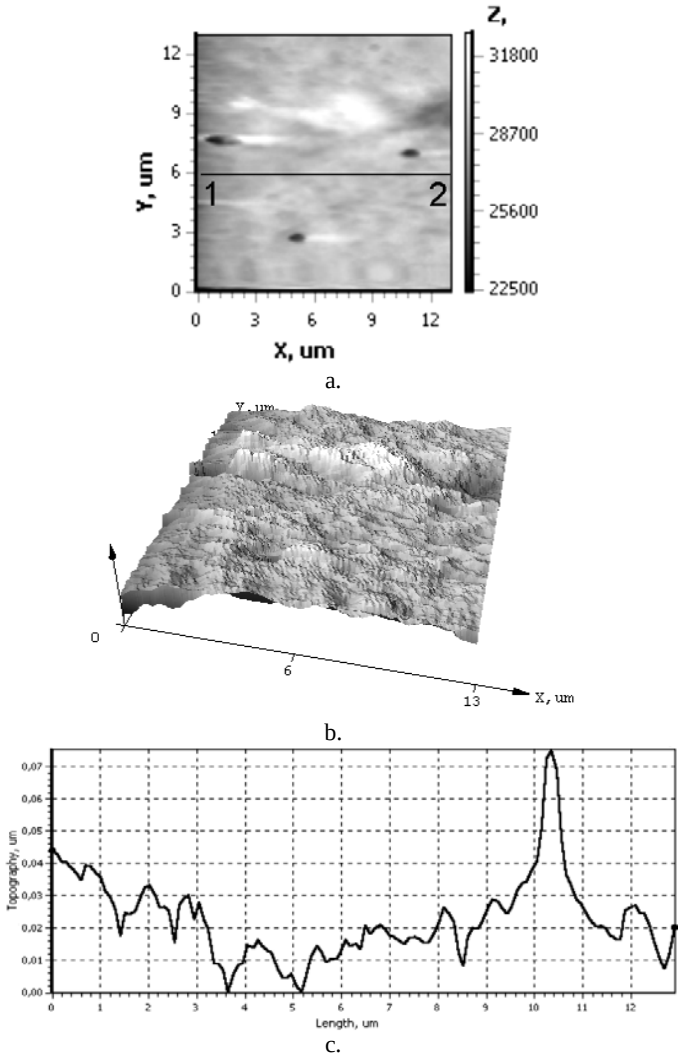

Fig.1. The topogram (a), the microrelief (b) of the surface of the metal coating (Au) on the 13×13 mkm section on a silicon plate Kp0 and a profile along the line 1-2 (c).

At the same time, the average roughness of a surface of such coverings makes 50-75 nanometers. The adhesive strength of the metal coating to the board was set by the method described in [6] and was 20-25 MPa.

After metallized surfaces processing by a low-energy electron stream of the ribbon shape, the metal coating melts, which somewhat reduces the residual microroughness (up to 35-50 nm), and its partial fusion into the surface layer of silicon increases the adhesive strength of the coating to 34-45 MPa, Fig.1.

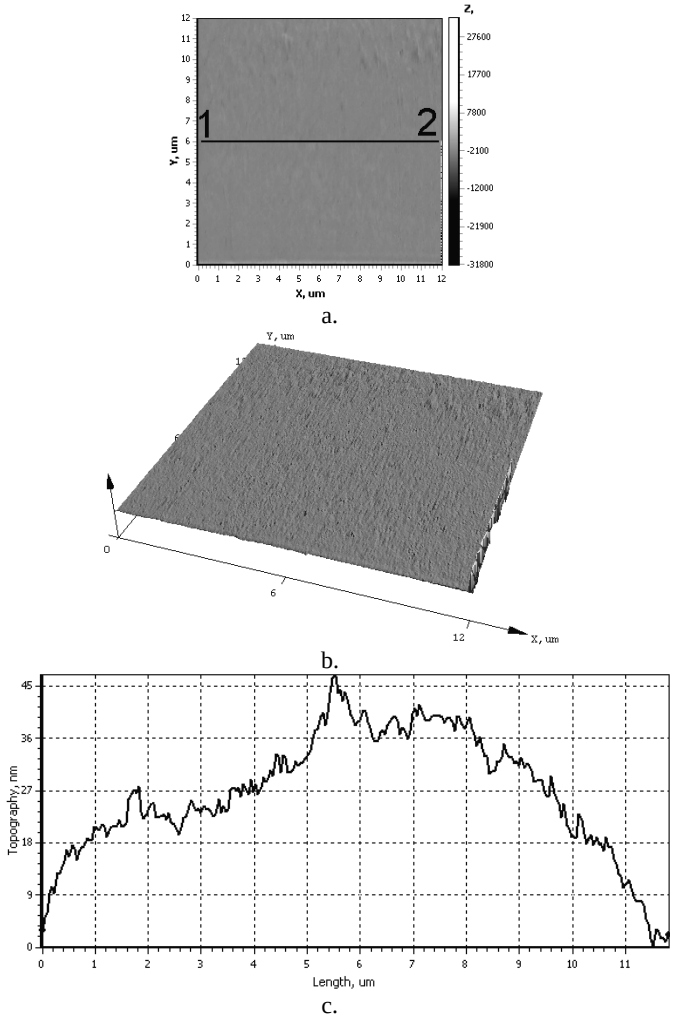

Fig.2. The topogram (a), microrelief (b) of the surface of the metal coating (Au) on the 13×13 micron section on a silicon plate Kp0 and a profile along the line 1-2 (c) after modification by an electronic stream.

4. Conclusion

The practical possibility of atomic force microscopy method to estimate uniformity of thin metal coverings on silicon plates after electronic processing which are used in precision instruments industry is shown.

Using atomic force microscopy method, it was established that after processing of the metalized surfaces of silicon plates Kp0 by a low-energy electron stream of the ribbon form, microroughness decreases from 50-75 nm (metalized surface) to 3.5-5 nm (metalized surface after electron processing) and Adhesive strength increases from 20-25 MPa to 34-45 MPa.

At the same time it is noticed that the surface of metal coverings on silicon after electronic processing has more homogeneous structure and it is saved from microdefects unlike the metalized coverings without electronic processing.

5. Literature

1. Bondarenko M.A. Yzučenye mexanyzma formyrovanyja ul'tratonkyx funkcyonal'nyx pokrytyj na optyčeskom stekle pry kombynyrovannoj elektronno-lučevoj mykroobrabotke (*Study of the mechanism of formation of ultrathin functional coatings on optical glass in combined electron-beam microprocessing*) / M.A.Bondarenko, Ju.Y.Kovalenko, Ju.Ju.Bondarenko, S.A.Bylokon y dr. // Sovremennye problemy fyzyky kondensyrovannoho sostojanyja, nanotexnolohyj y nanomateryalov: III meždunar. nauč. konf., 15-16 maja 2014: mater.dokl.– Almaty: Kazax unyversyteti, 2014. – S.64-65.
2. Yatsenko I. Influence of parameters by electronic ray on properties of superficial layers of optical elements of exact instrument-making / I.Yatsenko, V.Antonyuk, M.Bondarenko, V.Vashchenko // Innovations in engineering: Intern. scien.-tech. conf., 9-12 september 2015. – Burgas, Bulgaria. – Vol. 20/183. – 2015. – pp. 64-66.
3. Antonyuk V.S. Formation of Wear-Resistant Coatings on Silicon Probes for Atomic Force Microscopy by Thermal Vacuum Evaporation / V.S.Antonyuk, S.O.Bilokin,

M.O.Bondarenko, Yu.Yu.Bondarenko [etc.] // Journal of superhard materials. – 2015. – Vol.37. – No. 2. – pp.112-119.
4. Bondarenko M.O. Doslidžennja mexaničnyx xarakterystyk elementiv pryladiv točnoho pryladobuduvannja metodom atomno-sylovoji mikroskopiji (*Investigation of mechanical properties of elements Precision Instrument by atomic force microscopy*) / M.O.Bondarenko // Visnyk Čerkaskoho deržavnoho texnolohičnoho universytetu. Serija: Texnični nauky. – Čerkasy: ČDTU, 2015. – #2 – S. 21-28.
5. Pokryttja u pryladobuduvanni (*Coverage of instrument-making*) [Tekst]: monohrafija / V.S.Antonyuk, H.S.Tymčyk, Ju.Ju.Bondarenko, Ju.I.Kovalenko, M.O.Bondarenko ta in. // K.: NTUU «KPI», 2016. – 360 s.
6. Bondarenko M.A. Yssledovanye poverchnosty kremnyja posle mykroobrabotky nyzkoenerhetyčeskym lentočnym elektronnym potokom (*Investigation of the silicon surface after microprocessing by a low-energy ribbon electron beam*) / M.A.Bondarenko, Ju.Ju.Bondarenko, O.V.Svyrydova // Rastrovaja elektronnaja mykroskopyja y analyt. metody yssledovanyja tverdych tel: XIX Ros. sympoz., 1-4 yjunja 2015 h: tezysy dokl., h.Černoholovka, 2015.

DEVELOPMENT OF MATHEMATICAL MODELS OF THERMAL PLASMA PROCESSES

Prof. Frolov V. D.Sc., Ivanov D. Ph.D.
Institute of Energy and Transport Systems – Peter the Great Saint-Petersburg Polytechnic University, Russian Federation
eie@spbstu.ru

Abstract: *Application of a mathematical modelling of thermal plasma processes is effectively during development and optimization of electric power equipment as well as electro technological equipment. In the field of electric power industry such devices are: circuit breakers (simulation of arc extinction in the arc chamber); multi-chamber arresters for lightning protection of overhead power lines (simulation of arc discharge in a chamber of the arrester), and others. In the field of electro technological equipment such devices are: DC (and AC) arc plasma torches for air-plasma spraying of coating, metal welding and cutting; ICP (inductively coupled) plasma torches for nanomaterials production, fine powder treatment, plasma-chemical technologies and others. The article describes the main stages of the development of mathematical models: a study of the features of the physical process that allows us to formulate the basic assumptions of the model (stationary or non-stationary process, 2D or 3D geometry, laminar or turbulent flows and others); construction of the computational domain and of the mesh; setting the boundary conditions. Examples of results of calculations are shown. Recommendations on the use of specialized software are presented.*

Keywords: MATHEMATICAL MODELING, PLASMA PROCESSES, ELECTRO TECHNOLOGICAL EQUIPMENT

1. Introduction

In the field of electric power industry the operation of such electrical apparatuses as automatic switches, arresters, etc. is connected with an extinction of electric arc. For example, the use of multi-chamber arresters with electrodes placed into a chamber made of dielectric material is a promising way to protect overhead transmission lines from lightning overvoltages. When lightning current goes through the arrester, electric arcs appear in discharge chambers and they form the plasma jets from chambers.

In the field of electro technological equipment processes based on the use of arc plasma torch and radio-frequency (RF) inductively coupled plasma (ICP) torch are widely used. These are processes such as air-plasma spraying of coating, welding and cutting of metals, treatment of fine powder with various purposes, plasma-chemical technologies, etc.

Thus, during the development and optimization of electric power equipment and electro technological one the main subject of research are thermal plasma processes which are characterized by plasma parameters such as temperature and velocity as well as their variation in time.

To achieve this goal it is necessary to identify qualitative and quantitative relationships between the efficiency of the process (it can be an extinction of electric arc with minimal time or, conversely, generation of stable electric arc) on the one hand, and the geometry of the device and its operation parameters on the other hand. To determine those relationships it is necessary to carry out a large amount of experimental research which requires large time and material costs. Another way of obtaining that information is mathematical modeling of thermal plasma processes in arc and RF plasma torches.

2. Mathematical model

At present time a large number of mathematical models of plasma processes have been developed including a disturbance of thermal equilibrium, a plasma turbulence, etc.

The basic equations in a simplified model of plasma (it is assumed that plasma is in a state of local thermodynamic equilibrium, it is laminar and optically thin), express the fundamental conservation laws (of energy, momentum and mass), and for the elementary volume are written as follows [1]:

- energy equation:

$$\nabla\cdot\left(\rho\vec{\upsilon}h\right)=\sigma E^2-u_{rad}-\nabla\cdot\left(-\frac{\lambda}{c_p}\nabla h\right) \qquad (1)$$

- motion equation:

$$\nabla\cdot\left(\rho\vec{\upsilon}\vec{\upsilon}\right)=-\nabla p+\vec{F}_B+\rho\vec{g}+\nabla\cdot\left(\mu\nabla\vec{\upsilon}\right) \qquad (2)$$

- continuity equation:

$$\nabla\cdot\left(\rho\vec{\upsilon}\right)=0. \qquad (3)$$

Equations (1) – (3) include:

- plasma parameters such as enthalpy h that related to temperature T; velocity $\vec{\upsilon}$; pressure p;

- thermophysical plasma properties such as density ρ; thermal conductivity λ; specific heat c_p; viscosity μ; electrical conductivity σ; specific radiation power u_{rad};

- electromagnetic values such as electric field intensity E; electromagnetic force $\vec{F}_B=\vec{J}\times\vec{B}$.

Since plasma exists in an electromagnetic field the system of equations (1) – (3) is supplemented by Maxwell's system of electromagnetic equations:

$$\begin{cases}\nabla\times\vec{E}=-\dfrac{\partial\vec{B}}{\partial t}, & \nabla\cdot\vec{E}=\dfrac{\rho_{el}}{\varepsilon_0},\\ \nabla\times\vec{H}=\vec{J}, & \nabla\cdot\vec{B}=0,\end{cases}$$

where $\vec{E}$ и $\vec{H}$ are electric and magnetic field intensities; $\vec{B}$ is magnetic induction; $\vec{J}$ is current density; ρ_{el} is volume density of electrical charge; ε_0 is electric constant.

For thermal plasma processes the Maxwell's system of equations reduces to equations for the scalar (φ) and vector ($\vec{A}$) potentials:

$$\begin{aligned}&\nabla\cdot\left(\sigma\,\nabla\varphi\right)=0,\\ &\sigma\frac{\partial\vec{A}}{\partial t}+\frac{1}{\mu_0}\nabla\cdot\vec{A}=\vec{J},\end{aligned} \qquad (4)$$

where $\vec{J}=\sigma\left(-\nabla\varphi+\vec{\upsilon}\times\vec{B}\right)$, $\vec{B}=\nabla\times\vec{A}$.

Thus, equations (1) – (4) represent a system of equations that need to be solved simultaneously to obtain the distributions of the required quantities – plasma parameters, namely, temperature, velocity, pressure, electromagnetic quantities. The region of existence of the plasma is taken as a computational domain.

Boundary conditions for each required quantity are set at each boundary of the computational domain on the basis of the simplest physical considerations.

As already mentioned the system (1) – (4) includes thermophysical properties of plasma. For the main gases used in plasma processes the dependence of these properties on temperature (usually at atmospheric pressure) is given in the scientific literature [2-4]. The difficulty in solving system (1) – (4) lies in the fact that the temperature in the plasma torches varies in the range 300–20000 K, and with this temperature change the properties of the plasma vary by several orders of magnitude.

There are many software packages that allow modeling thermal plasma processes. The most famous commercial programs are ANSYS (CFX, Fluent), Comsol Multiphysics. The indisputable advantages of these programs are: the breadth of application (from the aerospace design to the biomedical application), relative simplicity (most of the functions and equations are already written, one just need to learn how to use them correctly) and high workflow productivity (a competent specialist can create a working model within a few hours).

In addition, usually it is possible to improve existing models with own code. For example, in the ANSYS Fluent software package it is possible to add user defined functions (UDF) written in the C programming language. This allows you to focus on a detailed description and investigation of the specific features of thermal plasma processes, while using ready-made procedures for those parts of the calculation that are common to other standard models (for example, using standard methods for solving systems of linear algebraic equations).

Examples of the application of various software products for the calculation of thermal plasma processes are presented below.

3. Modeling of thermal plasma processes in an arc plasma torch for spraying in Comsol Multiphuysics

A two-dimensional axis-symmetrical mathematical model of the plasma torch has been studied. The torch geometry corresponding to the real experimental set-up is presented in Fig. 1. The mesh is shown in Fig. 2. The mesh for calculation consists of 5098 elements.

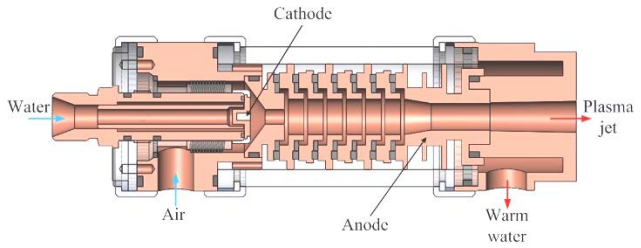

Fig. 1 *Design of DC plasma torch with inter-electrode sections*

Fig. 2 *Mesh for calculation*

Two models have been implemented in the software Comsol Multiphysics [5]: laminar plasma flow model and turbulent plasma flow model (SST-model).

The distributions of the gas temperature for arc current 200 A, laminar and turbulent flow are shown in Figs. 3–4.

Maximal gas temperature is 30 000 K. The shape of the temperature distribution for the model of turbulent flow is confirmed by frame from high-speed shooting – see Fig. 5.

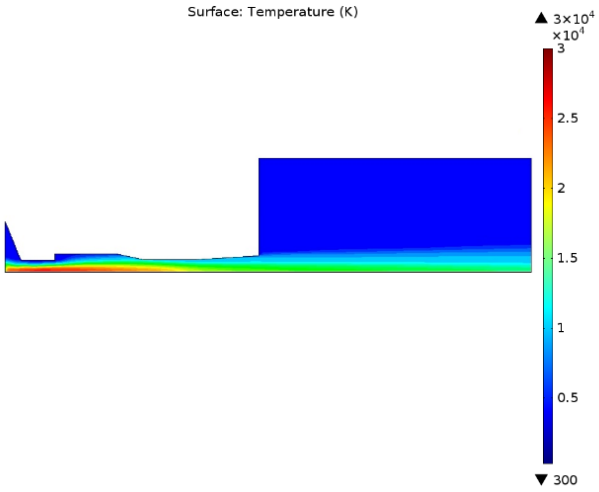

Fig. 3 *Temperature distribution in plasma torch: laminar flow*

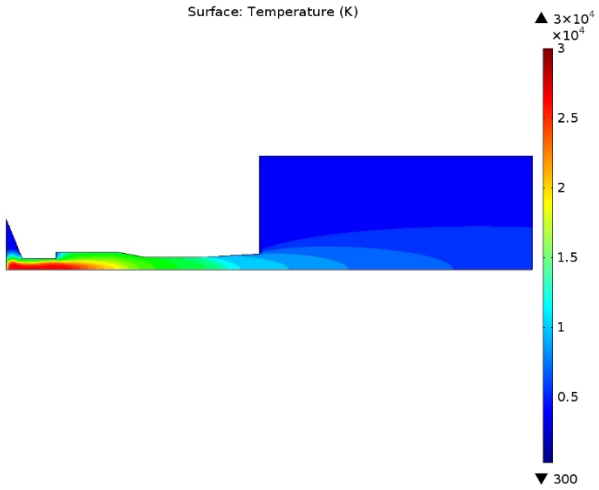

Fig. 4 *Temperature distribution in plasma torch: turbulent flow*

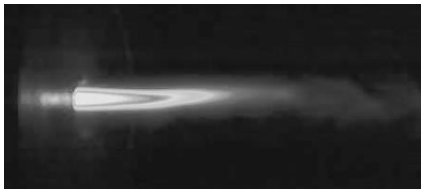

Fig. 5 *Image of plasma jet*

4. Examples of thermal plasma modeling in ANSYS Fluent

Discharge chamber of multi-chamber arrester. The multi-chamber arrester consists of a large number of series-connected chambers (Fig. 6), in which electrical breakdown leads to an arc discharge generation [6]. Such discharge is accompanied by erosion of the electrode material and by evaporation of the discharge chamber material. Thus pressure increases in the chamber that leads to appearance of plasma jet from the discharge chamber and to arc extinction.

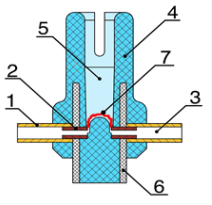

Fig. 6 *Design of discharge chamber of multichamber arrester: 1 – outer tube, 2 – inner tube, 3 – cavity, 4 – silicone rubber, 5 – discharge slot, 6 – fiber-glass plastic sleeve, 7 – arc*

To simulate plasma processes a three-dimensional nonstationary mathematical model was developed with the following features:

- The thermophysical properties of plasma were calculated taking into account an erosion of the electrodes material and an ablation of the discharge chamber walls [7], in the model they are included as dependences on temperature at a constant pressure of 10 atm;

- The case of tungsten electrodes and a silicone rubber chamber (ratio of Si: O: C: H = 1: 1: 2: 6, W: O = 1: 10) was considered;

- Evaporation of the discharge chamber material was taken into account as a source of mass;

- The motion of plasma is turbulent, the SST model was used to simulate turbulence.

The computational domain and the mesh for calculation are shown in Fig. 7.

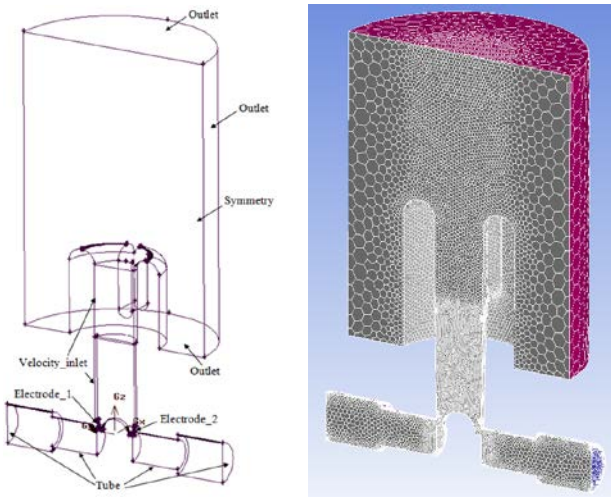

Fig. 7 *The computational domain of discharge chamber and the mesh for calculation*

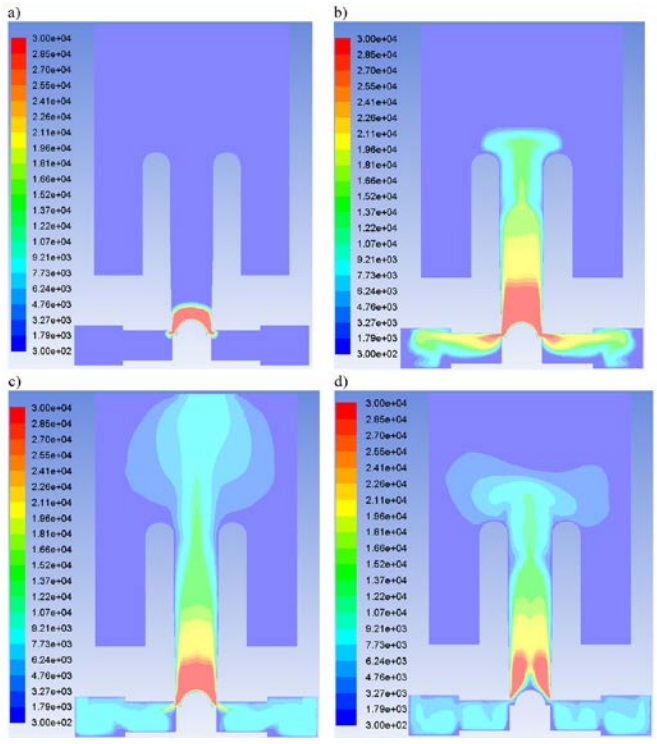

Fig. 8 *Distributions of plasma temperature (T, K)in the discharge chamber at different points of time: a – 2 μs, b – 30 – μs, c – 140 μs, d – 210 μs*

The computational domain includes a space surrounding the outlet of the discharge chamber which allows to calculate a process of formation of plasma jet from the discharge chamber. As a calculation region, it is convenient to take only half the space of the discharge chamber and the surrounding space since this space has a plane of symmetry (this is the plane of Fig. 6).

An electrical potential difference is defined on electrodes surfaces as boundary condition for the electromagnetic problem so that a discharge current through the chamber corresponds to the experimentally obtained dependence at each moment of time.

Results of simulation i.e. distributions of plasma temperature at different points of time are shown in Fig. 8.

Analysis of the simulation results shows that the presence of cavities joined to the main volume of the discharge chamber by small openings leads to the fact that at the initial stage of discharge, when pressure inside the discharge chamber exceeds pressure inside the cavities, plasma begins to spread into these cavities. The pressure inside the cavities is increased as long as it begins to exceed the pressure in the discharge chamber, which is lowered due to propagation of the discharge towards the outlet of the discharge chamber. It occurs in about 140-150 μs after the start of discharge. Thereafter, the gas accumulated in the cavities with lower temperature than the discharge core, begins to move in the opposite direction, i.e. from cavities to the discharge chamber. After 160 μs it leads to cooling of the central part of the discharge, which undoubtedly contributes to the extinction of the electric arc. This conclusion is confirmed by the results of experimental observations.

Combined plasma torch for nanomaterials production. A combined plasma torch consists of a series-connected a DC arc plasma torch and a RF ICP plasma torch. In this case, plasma jet of the arc plasma torch is fed to the inlet of the RF ICP plasma torch. That design provides an ignition of RF plasma and a reduce the power of the RF discharge. The combined plasma torch was studied for a technology of titanium dioxide nanopowder production.

To simulate the processes in the combined plasma torch and in the reactor a two-dimensional axisymmetric model was developed. The computational domain was divided by a mesh into 300,000 cells. Argon was used as the plasma-forming gas at a pressure of 1 atm.

To select the plasma torch operation mode that provides the evaporation of initial TiO_2 powder a series of calculations was carried out. The power of the arc discharge varied in the range of 10-15 kW, the power of RF discharge was in the range of 20-40 kW, the gas flow rate was in the range of 20-100 slpm, the inductor frequency of 1.76 MHz and 5.28 MHz was used.

Calculations showed that the use of the frequency of 5.28 MHz for such a design is more efficient.

An example of the calculation results is shown in Fig. 9 (arc discharge power is 12 kW, RF discharge power is 20 kW, gas flow rate is 60 slpm).

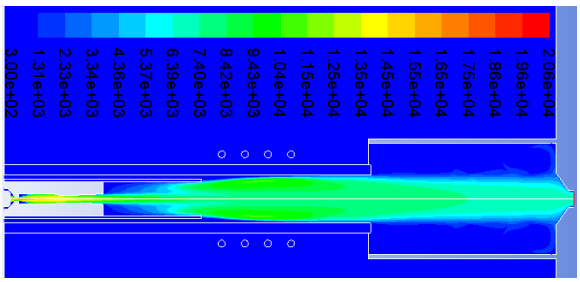

Fig. 9 *Distribution of plasma temperature in the combined plasma torch*

Modeling of a plasma jet loaded with fine powder. The treatment of fine powder (in this case – titanium dioxide powder) in a plasma jet has to simulate using a three-dimensional model. The reason of it is the disturbance of the plasma jet axial symmetry by the lateral feeding of a flow of carrier gas loaded by fine powder.

Initial powder was TiO2 with a mean diameter of 15 μm.

A series of calculations was carried out with the constant start velocity of powder feeding (10 m/s) and different powder feed rate (2–5 kg/h). Also calculations were made for the constant powder feed rate (4 kg / h) and different start velocity (5, 8, 10, 12 and 15 m/s) [8]. These calculations were made in order to find the optimum feed rate and start velocity of titanium dioxide. In those calculations the parameters of plasma jet (temperature and velocity at the inlet of the computational domain – the plasma reactor) correspond to the parameters of plasma jets created by the combined plasma torch.

Calculations showed that without feeding the powder the plasma jet has an axial symmetry which is significantly disturbed when the powder is fed through the feed-through line.

Best results (optimal trajectory of particles and its heating) were obtained at a powder feed rate of 4 kg/h and a start velocity of 10m/s (see Fig. 10).

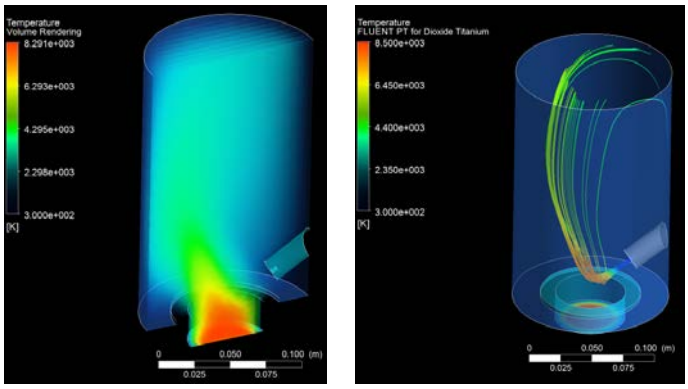

Fig. 10 *Distribution of plasma temperature T, K (left) and trajectory and temperature of TiO2 particles (right) for a powder feed rate of 4 kg h and a start velocity of 10 m/s*

5. Modeling of plasma processes using free software package OpenFOAM

The main disadvantage of commercial software packages is a high price. In addition, the researcher who uses such packages has to "play by someone else's rules", i.e. his capabilities are limited to existing models of the package. For researchers who need to solve non-trivial tasks the commercial packages envisage to create own models but this requires knowledge and programming skills that sharply raises the required skill level of the researcher and reduces the attractiveness of using such packages.

These disadvantages make one pay attention to free software. Currently in the field of free software there are a large number of programs that allow solving numerical simulation problems: Code_Aster, Code-Saturne, OpenFOAM and Elmer. All these software packages have a fairly extensive set of ready-made subroutines, but their main strength lies in a possibility to write own solution for any task.

An example of mathematical modeling of plasma processes using the free software package OpenFOAM is considered.

OpenFOAM (Open source Field Operation And Manipulation CFD ToolBox) is a freely available tool for computational fluid dynamics for operations with scalar, vector, and tensor fields. The basis of the OpenFOAM is a set of libraries that provide tools for solving systems of partial differential equations both in space and in time. The working language of the code is C ++.

OpenFOAM package was applied to calculate a plasma process of TIG welding. In OpenFOAM there is no ready solver for such a task therefore its creation was the first step. As a basis the standard solver *buoyantSimpleFoam* was used, in which the energy equation, the motion equation and the continuity equation are solved together.

The solver *buoyantSimpleFoam* was modified as follows: the equations of the electromagnetic problem were added; the electromagnetic force was taken into account in the motion equation; Joule heating and radiation energy losses was taken into account in the energy equation; nonlinear dependences of thermophysical plasma properties on temperature was introduced into the model; specific for plasma boundary conditions were introduced.

For the calculation the following geometry of the TIG torch was used: the electrode diameter was 3 mm, the internal diameter of the nozzle was 9 mm, the distance from the cathode to the anode (welding parts) was 4 mm. The following operation mode was calculated: arc current was 100 A, argon flow rate was 5 slpm. This mode of operation can be used to weld aluminum plates with thickness of 2–3 mm [9]. The task was solved in a two-dimensional formulation.

The results of the calculation i.e. the distributions of the temperature and the axial velocity of plasma are shown in Fig. 11.

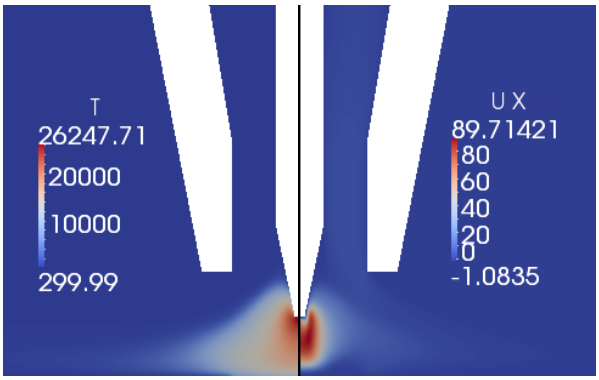

Fig. 11 *Distributions of the temperature (left) and the axial velocity (right) of plasma in TIG torch*

6. Conclusions

Various methods for calculating thermal plasma processes are studied at the Department of Electrical Power Engineering and Equipment of Peter the Great Saint-Petersburg Polytechnic University. The results of the research are used in teaching students, including in the preparation of master's theses.

For complex calculations of thermal plasma processes it is recommended to use specialized software: ANSYS Fluent, Comsol Multiphysics as well as the free software package OpenFOAM. Of course, it is necessary to check the applicability of the built-in models to the plasma conditions and, if necessary, to correct them.

References

1. S.V. Dresvin, D.V. Ivanov, V.Ya. Frolov. Method of calculation of thermal plasma processes. *Induction heating*. 2012. V. 4(22). P. 25-34 (in Russian).

2. V.S. Engel'sht, V.Ts. Gurovich, G.A. Desyatkov and others. Theory of the electric arc column. Novosibirsk: Nauka, 1990 (in Russian).

3. M.I. Boulos, P. Fauchais, E. Pfender. Thermal Plasmas: Fundamentals and Applications, Vol. 1. NY: Plenum Press, 1994.

4. S.V. Dresvin, D.V. Ivanov. Plasma physics. St. Petersburg Polytechnic University Publ. house, 2013 (in Russian).

5. V. Frolov, I. Murashov, D. Ivanov. Special Aspects of DC Air Plasma Torch's Operating Modes under Turbulent Flow Conditions. *Plasma Physics and Technology*. 2015. V. 2 (2). P. 129-133.

6. G.V. Podporkin Development of Long Flashover and Multi-Chamber Arresters and Insulator-Arresters for Lightning Protection of Overhead Distribution and Transmission Lines. *Plasma Physics and Technology*. 2015. V. 2(3). P. 241-250.

7. V.Y. Frolov, D.V. Ivanov, Y.V. Murashov, A.D. Sivaev. Calculation of the composition of plasma of an arc pulsed discharge in a multichamber arrester. Technical Physics Letters. 2015. V. 41(4). P. 310-313.

8. M.A. Shibaev. Study of combined plasma torch for plasma technology of nano titanium dioxide production. Master Thesis. SPbSPU, St. Petersburg, 2012 (in Russian).

9. Electrotechnological industrial installations. Ed. V.Ya. Frolov. St. Petersburg Polytechnic University Publ. house, 2009 (in Russian).

INVESSTIGATION OF MICROSTRUCTURAL AND MECHANICAL PROPERTIES OF DIFFERENT TYPE OF CASTINGS

Prof. Dr Cvetkovski. S. PhD.[1] Prof. Dr Kozinakov. D. PhD[2]
Faculty of Technology and Metallurgy – Ss Cyril and Methodius University, Skopje Republic of Macedonia [1]
sveto@tmf.ukim.edu.mk
Faculty of Mechanical Engineering – Ss Cyril and Methodius University, Skopje Republic of Macedonia [2]
sveto@tmf.ukim.edu.mk, dimitri.kozinakov@mf.edu.mk

Abstract:
In this research work are presented results and procedure for investigations different types of castings in order to check their properties according to appropriate standards, to identify type of unknown casting, to detect and analyze different type of defects in castings and to perform failure analyze in order to determine the reasons for fracture. Presented investigations are basic research activities which are performed almost in all research laboratories for investigations of castings.
They mainly consist of identification of visual inspection, investigation of chemical composition, investigation of mechanical properties and microstructural identification. Completing of the results from performed investigations and their analysis required information about investigated casting can be obtained.
In this research work are given result of investigations of three castings GJS- 450-10 cast iron, malleable cast iron and Hadfield steel casting.
KEYWORDS: NODULAR IRON, HADFIELD STEEL, TEMPER IRON, MICROUSTRUCTURE, MECHANICAL PROPERTIES, CHEMICAL COMPOSITION.

1. Introduction

Foundries produce ferrous and non-ferrous metal castings. Ferrous castings comprise iron and steel, while non-ferrous castings primarily include aluminum, copper, zinc, lead, tin, nickel, magnesium, and titanium. Castings are produced by melting, pouring, and casting the ferrous and non-ferrous metals. Many foundries cast both materials. Many different casting techniques are available. All involve the construction of a container (mold) into which molten metal is poured [1,2].
Two basic casting process subgroups are based on expendable and non-expendable mold casting.
- Expendable mold casting, typical to ferrous foundries although also used in non-ferrous casting, uses lost molds (e.g. sand molding).
- Non-expendable mold casting, adopted mainly in non-ferrous foundries, uses permanent molds (e.g. die-casting). Lost molds are separated from the casting and destroyed during the shakeout phase, while permanent molds are reused. A variety of techniques are used within these two mold casting processes depending on the melting, molding and core-making systems, the casting system, and finishing techniques applied [3].
A typical foundry process includes the following major activities:
melting and metal treatment in the melting shop; preparation of molds and cores in the molding shop; casting of molten metal into the mold, cooling for solidification, and removing the casting from the mold in the casting shop; and finishing of raw casting in the finishing shop.
Different types of melting furnaces and metal treatments are used to produce ferrous and non-ferrous materials depending on the type of metal involved [4,5].
Cast iron is typically melted in cupola furnaces, induction furnaces (IF), electric arc furnaces (EAF), or rotary furnaces. Cast steel is typically melted in electric arc furnaces or coreless induction furnaces. Cast steel metal treatment consists of refining (e.g. removal of carbon, silicon, sulfur and or phosphorous) and deoxidization [6].
Casting parts are implemented in the different industrial sectors as individual units or as a part of more complex structures or machines. So failure of casting in the exploitation conditions can cause huge material and financial damages. It means that quality of the casting must beat must be at very high level. Because of that many investigation has to be performed after production of casting. In this research work main idea was to present investigation of different casting to check their microstructural and mechanical properties or to perform failure analysis of fractured casting.

2. Material and investigation

2.1 Investigation of casting (sleeve) produced of GJS- 450-10 cast iron

These investigations were performed as an expertise on the request of the Court. Subject of investigation were sleeve and the wheel of Reno Cangoo broken during the car accident (figure 1). Performed investigation should answer the question what was the reason for fracture. Was the reason existing of previously formed crack in the sleeve which propagated during the accident, or the reason is intensity of stroke during the accident.
After delivering the broken part the team of Faculty of Technology and Metallurgy decided to perform the following investigations:

- Visual inspection of the broken surface
- Determination of chemical composition of the sleeve,
- Tensile test,
- Hardness measurement,
- Metallographic investigations.

Visual inspection

Visual inspection was performed after cleaning the fractured surface in the solution of hydrochloric acid and water because the surface was corroded. Inspection was performed by necked eye and by magnifying lens. Detailed inspection didn't discover existing of the crack in the casting which starts to propagate in the moment of accident.

a b

Figure 1(a and b) *Broken sleeve and wheel*

Investigation of chemical composition

For determination of chemical composition of the investigated part was used spectrometer type SPECTRO. Results of investigations are given in the table 1.

Table 1 *Chemical composition of the sleeve*

Element	C	Si	Mn	P	S
%	2.95	3.05	0.23	0.017	0.005

According results from analysis of chemical composition was concluded that investigated part is cast iron (carbon 2.95% and Si 3.05%)

Tensile testing

From the broken sleeve was prepared specimen for tensile testing Results from investigations are given in the figure 2. Obtained results showed that ultimate tensile strength is Rm = 466 Mpa, while elongation is A = 13%. Mechanical properties confirmed that sleeve is produced from GJS- 450-10 cast iron [7].

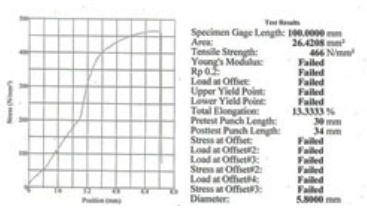

Figure 2 *Stress-strain diagram of investigated part (sleeve)*

Hardness measurement

Hardness measurement was performed on metallographic specimens figure HRB method was performed. Results of hardness measurement are given in the table 2. Measuring positions can be seen in the figure 3. It can be concluded that there is almost no difference in measured values. Obtained values correspond with the prescribed values (160-210 HRB) for this type of iron.

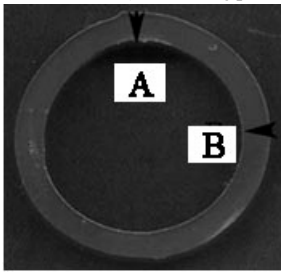

Figure 3 *Specimen for metallographic testing and hardness measurement*

Table 2 *Hardness values (HRB) of the investigated part*

A	B
173	174
176	173
174	173
171	174
171	174

Metallographic investigations

For metallographic investigation was prepared surface directly beneath Brocken surface. The idea is to detect if there is some casting defects in material. Standard metallographic preparation was performed, grinding and polishing after that. Polished specimens were analyzed using magnification of x100. The main idea was to detect type of graphite. As can be seen from the figure 4 graphite is in the form of nodules, pretty small and uniformly distributed in the matrix.

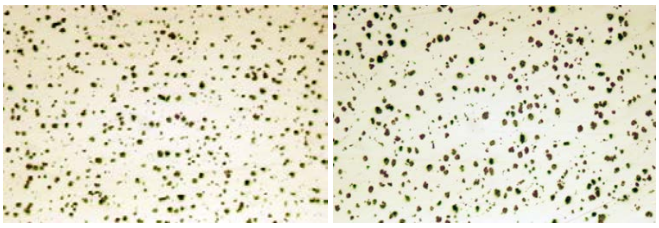

Figure 4 *Graphite nodules, polished specimen, x100*

The next step in the metallographic investigations was to etch the specimen with Nital and to reveal microstructure of the part. The picture of microstructure is presented in the figure 5. As can be seen from the figure 5, microstructure is fully ferritic.

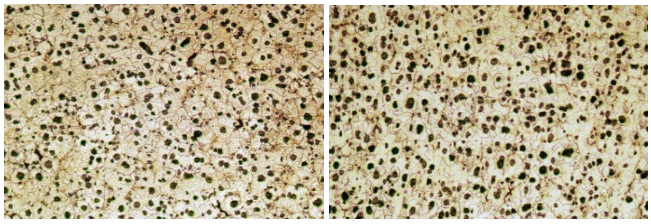

Figure 5 *Microstructure of investigated specimen, fully ferritic*

During visual inspection was not detected existing of formerly formed crack. From another point of view performed investigations confirmed that quality of the sleeve is very good. So the question is why sleeve fractured?

If we take a look at figure 5, the cross section of the sleeve at the place of fracture is not round at should be, but deformed. It indicates that fracture appeared as result of strong stroke during the car accident. Selection of this type of material is made by design engineers in the company. Performed investigation was confirmed by the literature dates too [8].

Figure 6 *Deformed cross section of the broken sleeve*

2.2 Investigation specimen from malleable cast iron

From metal processing company was delivered metal part with unknown chemical composition in order to be determined its composition and mechanical properties. The idea on the engineers n the company was to replace original parts with the new producer because original parts was very expensive To answer the this questions we perform the following investigations:

Determinations of chemical composition, hardness measurement and metallographic investigations

Determination of chemical composition

Chemical composition was performed on spectrometer type SPECTRO. Obtained results are presented in the table 3.

From the results of chemical composition could be concluded that concentration of carbon and sulphur is pretty high. Because of that checking of the content of these elements was made additionally on the LECO device and the same values were got. It was concluded

too that this is high alloyed cast iron because content of nickel is 10.48%

Table 3 *Chemical composition of investigated part (hollow cylinder)*

Element	%
C	5.0
Si	0.201
Mn	0.09
Ni	10.48
P	0.018
Cr	0.024
Cu	3.84
Mo	0.53
Ti	0.017

Hardness measurement

Hardness measurement was performed according to Brinell method (HRB) using hardness tester type "Avery". Measurement was done on the vertical cross section of the metallographic specimen. Obtained results from the hardness measurement are given in the table 4. It is obvious that hardness values are very low because of very long heat treatment.

Table 4 *Measured hardness values according to Brinell method*

Measuring points	1	2	3	4	5
Hardness (HRB)	70	72	75	73	71

Metallographic investigations

Metallographic investigations were performed on optical microscope type "MEIJI TECHNO". Standard procedure for preparation of specimens was performed. It means that after grinding and polishing of the specimen with suspension of Al_2O_3, etching with Nital was made. Prepared specimens were first investigated in polished condition at magnification of x100 to determine form of graphite (figure 7). As can be seen from the figure the free graphite is in the form of rosette. This form of graphite indicates that specimen is produced by malleable cast iron. Low values of hardness 70-75 HRB confirm this statement [].

Microstructure of investigated part was revealed by etching of specimen with Nital. As can be seen from the figure 8, microstructure is typical ferritic. It is concluded too that in the microstructure, near to graphic rosettes are detected carbides in the form of needles [9,10].

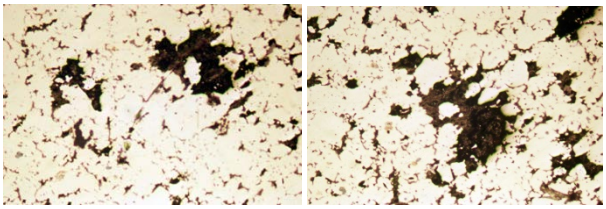

Figure 7 *The form of graphite in the investigated specimen – polished specimen, x100*

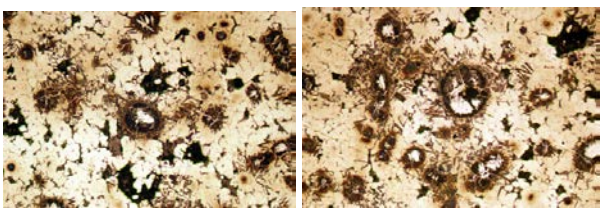

Figure 8 *Microstructure of investigated specimen – etched surface, 3% Nital*

Malleable cast iron is generally obtained from the white iron in which carbon is in the form of cementite During heat treatment cementite transforms in the form of graphite rosettes low values of hardness confirm that. Heat treating evolves in two phases. The first phase evolves at 900-1000 ^{0}C, while the second phase evolves at the temperature of 600-700 ^{0}C. Totally this process last more the 100 hours. Fractured surface of tempered iron could be white or dark. We found that fractured surface in our case is dark.

So, from the performed investigation was concluded that hollow section is produced from malleable cast iron with ferritic microstructure. Type of fractured surface is dark. High percent of nickel indicate that this is high alloyed iron. Low hardness values are result of performed heat treatment. Very high percent of carbon indicate that this is special type of temper iron.

2.3 Examination tooth of excavator

Tooth from excavator showed in figure 9a was delivered for investigation. Through performed investigation should be answered two questions:

- What is chemical composition of the tooth and
- What is the reason for breaking piece of the tooth?

The tooth was cut in few segments in order to perform necessary investigation

a

b

Figure 9 (a and b) *Investigated excavator tooth*

a. View of the tooth

b. Segments of tooth prepared cut for investigation

Determination of chemical composition

Results of performed chemical analysis are given in the table 5. Chemical analysis has to confirm if the composition of material fulfill requirement of EN 10349:2010. Comparing of obtained results in Table 5 and chemical composition given in the table 6 was concluded chemical composition correspond to G-x120Mn12 steel i.e. Hadfield steel with material number 1.3401. Some characteristics of investigated steel are given in the table 7.

Table 5 Chemical composition of investigated excavator tooth

Element	%
C	1.38
Si	0.68
Mn	12.76
Cr	0.36
Ni	0.13
Mo	0.014
S	0.012

Table 6 *Chemical composition of G-x120Mn12 steel according EN 10349:2010*

Element	%	
	min	max
C	1.1	1.3
Si	0.3	0.5
Mn	12	13
P		0.1
S		0.04
Cr		

Table 7 *Some characteristics of investigated material*

Material number	1.3401
Group	Structural steel
Subgroup	Steel with high percentage of Mn
Application	Parts for crushers

Microstructural analysis

For microstructural analysis of the investigated part metallographic specimens were prepared (figure 10). Typical microstructure is presented in the figure 11(a-c). It is obvious that microstructure is fully austenitic. On the austenitic grain boundaries are detected precipitated carbides. Detected carbides are spheroidal or elongated. Some spheroidal carbides are detected inside the austenitic grains, and they are coarser compared with the spheroidal carbides on the grain boundaries. Dominant carbides are elongated. Presence of carbide in the Hadfield steel was always noticed if the carbon concentration is over 1%, and carbides formation is more intensive if carbide forming elements are present.

Figure 10 *Prepared specimens for metallographic investigations*

In some cases, mainly for homogenization and hardening, Hadfield steel is heated to the temperature of 1050 °C, keeping at this temperature for few hours and fast cooling in water after that. At this temperature solution of carbides in matrix happens. And fast cooling suppresses their appearing again.

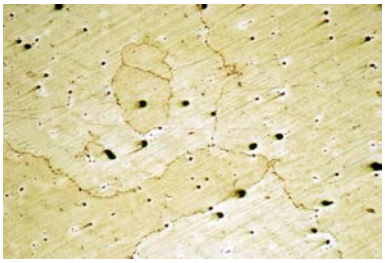

a

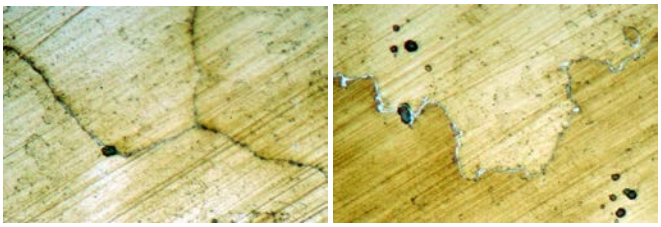

b c

Figure 11 *Microstructure of investigate excavator tooth*

Hardness measurement

Hardness measurement (figure 12) was performed at different specimens (pieces) of investigate material. It was concluded that hardness values are in the range of 120 to 150 HB which are pretty low values. Probably such low hardness values are obtained because heat treatment of this steel was not done. According standard hardness should be 200 HB at least. It is characteristic for Hadfield steel that its hardness increase during exploitation conditions (work hardening) to 250 HB and in extremely conditions to 500HB.

Figure 12 *Measuring of hardness on the metallographic specimen*

Visual inspection

Visual inspection of the tooth showed there is uncork part (figure 13a), at the back side of the tooth. At the fractured surfaces were noticed: segregation, pores and cracks (figure 13 b). It indicated that improper casting technology was performed.

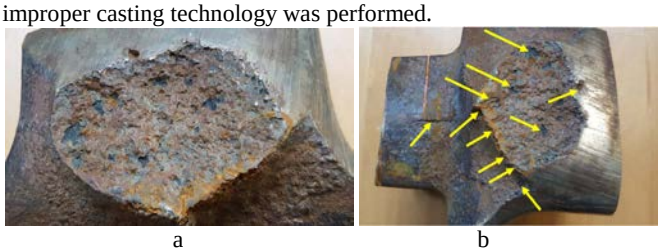

a b

Figure 13 Fractured surface from back side on the tooth

From the performed investigation of excavator tooth the following information's were obtained:

Excavator tooth was cast from the Hatfield steel. Its microstructure is fully austenitic inside the grains and on grain boundaries were detected carbides (spherical or elongated). Presence of carbides indicates that investigated part was not heat treated.

Increased concentration of carbides on the grain boundary or segregation mainly as results of presence of phosphorus increase brittleness of Hadfield steel [11].

Slow cooling between 400-800 °C is the reason for another type of brittles of the steel i.e. sensitation. As the most often founding defects in the Hatfield steel besides segregations are macro and micro pores [12].

3. Discussion

In this research work was presented procedure for investigation of different type of castings in order to determine their microstructural or mechanical properties, or to discover what was the reason for their failure in the exploitation conditions. Visual inspection, determination of chemical composition, tensile testing, hardness measurement and microstructural investigations are basic methods of investigation. To confirm some considerations nondestructive testing methods have to be performed too.

4. Conclusion

Results presented in this paper clearly showed that performed investigation could be always performed as basic investigations for identification of their properties or for performing failure analyze of damaged parts in exploratory conditions of different type of castings after their exploitation

5. Literature

[1] OTT D. 1997. Handbook, Casting and other defects. London.

[2] EMMIMA E. M. 2008. Integrated Management system in iron and steel foundry. PhD. Thesis. TU Košice.

[3] Qingdao Casting Quality Industrial Co., Ltd, Malleable Iron Property,http://www.castingquality.com/wpcontent/uploads/2009/7/malleable-iron-casting property.pdf
[4] Rajesh Rajkolhe, J. G. Khan, Defects, Causes and Their Remedies in Casting Process: A Review, International Journal of Research in Advent Technology, Vol.2, No.3, March 2014, E-ISSN: 2321-9637 375
[5] KASSIE A.A., ASSFAW S.B. 2013. Minimalization of Casting Defects. IOSR Journal of Engineering. Vol.3. Issue 5.
[6] Nikhil Yadav and D. B. Karunakar, EFFECT OF PROCESS PARAMETERS ON MECHANICAL PROPERTIES OF THE INVESTMENT CASTINGS PRODUCED BY USING EXPANDABLE POLYSTYRENE PATTERN, International Journal of Advances in Engineering & Technology, July 2011, IJAET, ISSN: 2231-1963
[7] CLAAS GUSS GmbH, Spheroidal cast iron EN-GJS, (formerly GGG), Technical Information No. 2, http://procast-guss.de/ html_e /pdf /THBl2_engl.pdf
[8] ACO Guss, Cast iron with nodular graphite (GJS) as per DIN EN 1563, Technical Material Data Sheet 1, www.acoguss.com/fileadmin/de_aco_eurobar/documents/Cast_iron_with_nodular_graphite__GJS__as_per_DIN_EN_1563.pdf
[9] GEETHA A/P MUNIANDY, AN INVESTIGATION OF MICROSTRUCTURE AND MECHANICAL PROPERTIES OF MALLEABLE CAST IRON USING METAL CASTING PROCESS, http://umpir.ump.edu.my/1400/1/Geetha_Muniandy_(CD_5040).pdf,
[10] Total Materia, Malleable cast iron, http://www.totalmateria.com/articles/Art96.htm
[11] Lihe Qian, Xiaoyong Feng and Fucheng Zhang, Deformed Microstructure and Hardness of Hadfield High Manganese Steel, Materials Transactions, Vol. 52, No. 8 (2011) pp. 1623 to 1628 2011 The Japan Institute of Metals
[12] Yuri N. Petrov, Valentin G. Gavriljuk, Hans Berns Fabian Schmalt, Surface structure of stainless and Hadfield steel after impact wear, Wear Volume 260, Issue 6, 10 March 2006, Pages 687–691

CORROSION BEHAVIOR OF COMMERCIALLY-PURE TITAMIUM WITH DIFFERENT MICROSTRUCTURES

КОРРОЗИОННОЕ ПОВЕДЕНИЕ ТЕХНИЧЕСКИ ЧИСТОГО ТИТАНА С РАЗЛИЧНОЙ МИКРОСТРУКТУРОЙ

Lead. Res., Dr. Semenov V.I.[1, 2, +], Prof., Dr. Huang S.-J.[3], Prof. Tontchev N.[4], Jun. Res. Valiev R.R.[2], Jun. Res. Belov P.A.[2], PhD Stud. Bogale D.[3], PhD Stud. Wang A.[3]

[1]SASI Institute for Strategic Studies, RB, Ufa, Russia
[2]Ufa State Aviation Technical University, Ufa, Russia
[3]National Taiwan University of Science and Technology, Taipei, Taiwan
[4]"Todor Kableshtov" Higher School of Transport, Sofia, Bulgaria
[+]corresponding author, e-mail: semenov-vi@rambler.ru

Abstract. This paper reports on the results of corrosion tests, using alternative methods, of Grade 4 CP Ti samples with coarse-grained (annealed) and ultrafine-grained structures after severe plastic deformation processing. The effect of microstructure on the corrosion of the material under study is demonstrated. It is revealed that the material with a UFG structure has a higher corrosion resistance, as compared to the samples with a CG structure.

KEY WORDS: *CORROSION; COMMERCIALLY PURE TITANIUM; COARSE-GRAINED AND ULTRAFINE-GRAINED STRUCTURE; SEVERE PLASTIC DEFORMATION.*

1. Gravimetric corrosion test

Introduction

Owing to a great interest in the production of high-strength implants for medical applications from commercially pure (CP) titanium, one turns, more and more often, to the technologies based on severe plastic deformation. These technologies enable producing a high-strength state due to the the formation of an ultrafine-grained (UFG) structure that contributes to a significant enhancement of mechanical and functional properties [1, 2].

Promising is the use of high-strength long-length materials with a UFG structure [3], in particular, from CP Ti [4] which can be used for the production of medical implants that are, in particular, in frictional contact in saline medium.

Relatively recently, studies focused on a comparative evaluation of the corrosion resistance of materials with a coarse-grained and UFG structure were initiated [5]. For instance, it was demonstrated in [6] that in the investigated materials (low- and medium-carbon steels), having a UFG structure after severe plastic deformation (SPD) processing by equal-channel angular pressing (ECAP), an increase in corrosion resistance is observed. It may be assumed that a similar effect should be expected for CP Ti as well.

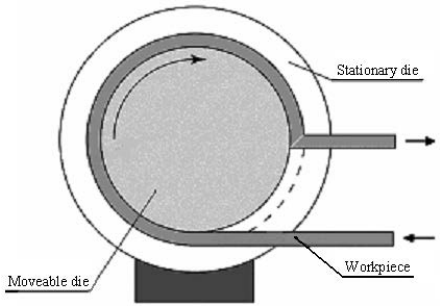

Fig. 1 Principle of the ECAP-Conform technique for the fabrication of long-length semi-products

After SPD processing, specimens with a length of 25 mm were cut out from the produced rods, for the deposition of ion-plasma coating and surface treatment by microarc oxidation. One specimen was left uncoated. In a similar manner, specimens were prepared from the annealed samples having a CG structure.

Corrosion tests were performed by immersion in 3.5% sodium chloride aqueous saline solution. Fig. 3 shows the diagram of the unit used to perform the corrosion tests.

The immersion tests were carried out in a waterproof thermostat during 28 hours at a temperature of 40±0.2°C.

There are known works on the fabrication of semi-products from CP Ti for medical applications, having a UFG structure, processed by SPD [7-9] followed by deposition of coatings from titanium nitride [7, 8] and diamond-like carbon with zirconium [9].

At the current stage of research, an express evaluation has been performed, of the corrosion properties of CP Ti, depending on the structural state and the presence of a coating on the surface of the investigated material in the coarse-grained (CG) and UFG states.

1.1. Material and research procedure

As the material for the study, CP Ti Grade 4 was used, with a CG structure in the annealed condition, and with a UFG structure in the SPD-processed condition. Fig. 1 shows the principle of the SPD technique employed to process the material.

The SPD processing of the material was conducted at a temperature of 400°C in 6 processing cycles, with rotation of the billet by 90° around its axis after each cycle. Fig. 2 shows the produced long-length samples from CP Ti Grade 4.

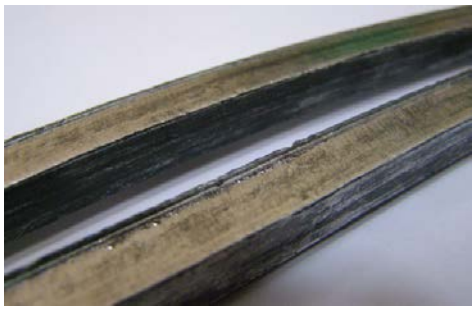

Fig. 2. CP Ti samples after SPD processing

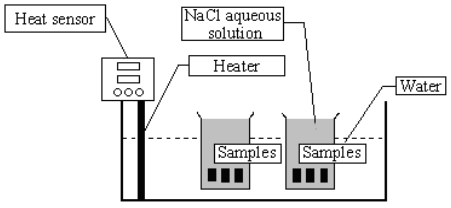

Fig. 3. Principle of the immersion tests

Metallographic studies were performed, using optical and transmission microscopes.

1.2. Research results

Given below are the results of the metallographic studies. Fig. 4 shows an example of microstructure transformation as a result of SPD processing.

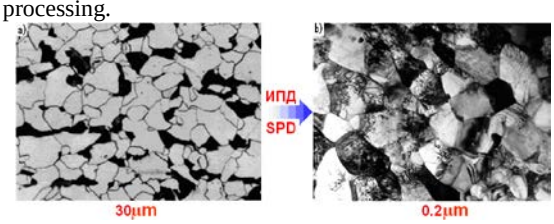

Fig. 4. Transformation of the material's microstructure as a result of SPD processing: a) coarse-grained structure of the material in the initial state; b) ultrafine-grained structure of the material after SPD processing

As a result of metallographic studies, it has been established that in the initial state the microstructure of CP Ti represents an equiaxed structure with a mean grain size of 30 μm. The deformation processing by ECAP leads to an efficient grain structure refinement, with the mean grain size equal to 0.2 μm.

As was already noted above, before conducting the corrosion tests, an ion-plasma coating of TiC composition was deposited on the surface of some specimens, and some specimens were processed by microarc oxidation. As a result of the processing by microarc oxidation of specimens with different microstructures, an oxide film of TiO composition was formed on the surface of CP Ti. When studying the film formed through the use of either technology, it was established that its thickness was 3±0.3 μm.

The results of corrosion tests are given in Table 1.

Table 1. Results of corrosion tests

Specimens / Mass, g	Coarse-grained structure (CG)			Ultrafine-grained structure (UFG)		
	Uncoated	Ion-plasma coating	Microarc oxidation	Uncoated	Ion-plasma coating	Microarc oxidation
Initial mass	9.003	8.960	8.436	9.185	9.133	8.787
28 hours	8.993	8.958	8.435	9.182	9.132	8.786
Mass loss, %	0.11104%	0.02232%	0.01185%	0.03266%	0.01095%	0.01138%

For the sake of visualization, the results of the corrosion tests are presented in the form of a bar chart in Fig. 5.

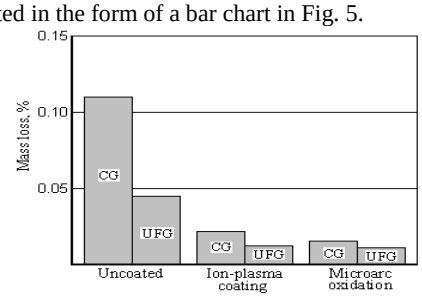

Fig. 5. The results of comparative corrosion tests: CG denotes the coarse-grained material after annealing; UFG denotes the ultrafine-grained material after SPD processing

As can be seen from the preliminary results of the corrosion tests (Fig. 6), the type of the applied coating (ion-plasma deposition and microarc oxidation) has practically no effect on the extent of corrosion damage. The differences between them fall within the statistical error. This may indicate a rather high protective capability of both coating types. At the same time, it is noted that the uncoated material after SPD processing in the UFG state has a considerably lesser degree of corrosion damage, as compared with the initial (annealed) state with a coarse-grained structure. The corrosion rate of the uncoated specimens from CP Ti Grade 4 in two structural states was evaluated. Fig. 6 shows the variation of mass loss depending on the time that the specimens were held in the 3.5% NaCl saline solution.

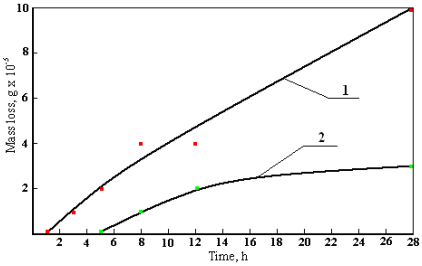

Fig. 6. Corrosion rate of CP Ti Grade 4: 1 denotes the CG structure after annealing; 2 denotes the UFG structure after SPD processing

As can be seen from this graph the specimens with a CG structure (curve 1) exhibit a much higher corrosion rate, as compared to the specimens with a UFG structure (curve 2) in the accepted time interval. The variation of mass loss for the CG material in the selected time range has a practically linear character. In contrast, for the specimens with a UFG structure there is observed an area with a small slope of the curve, which indicates a decrease in the corrosion rate. In addition, it is noted that for the specimens with a CG structure, the start of the corrosion process is recorded after the first hour of testing, whereas for the specimens with a UFG structure, the first signs of the starting mass loss are observed only after five hours of testing.

Presumably on the material with UFG structure in connection with more advanced and extended total grain boundary these layers form a dense, almost impermeable barrier, due to which corrosion is strongly inhibited or completely stopped. Passivation is carried out chemically or electrochemically. In the latter case, conditions are created when metal ions under the influence of current pass into a solution containing ions, the ability to form very slightly soluble compounds. This assumption requires further study of the corrosion behavior of commercially pure titanium with different microstructure in an aqueous solution of sodium chloride using electrochemical methods with the formation of anodic and cathodic curves.

These observations require more detailed investigations to study the mechanism of corrosion damage of CP Ti with different microstructures.

2. Electrochemical corrosion tests

Introduction

The high corrosion resistance of CP Ti is conditioned by its self-passivation. In a weak-acid medium, the corrosion of non-passivated Ti is the result of two coupled reactions: the anodic reaction Ti—2e = Ti^{2+} and the cathode reaction $2H^+ + 2e = H_2$.

2.1. Experimental procedure

The polarization curves were recorded according to the three-electrode scheme, using a silver-chloride reference electrode and a platinum auxiliary electrode. The samples were polished with abrasive papers of decreasing grit size and a diamond paste, afterwards they were degreased with a White Spirit solution and

installed into a three-electrode cell with a 3.5% NaCl + 3% CH_3COOH solution until the equilibrium potential was reached. The potential sweep was conducted from the equilibrium potential to ± 400 mV with a rate of 1 mV per second.

2.2. Results and discussion

In Fig. 7 the anodic reaction is displayed by the initial region of the curve, demonstrating a transition from active dissolution to the onset of passivation at the potential E_p and full passivation at the potential E_{fp}; for the UFG samples passivation occurs at larger potentials than for CG samples, but the current of passivation onset for the CG sample is slightly higher.

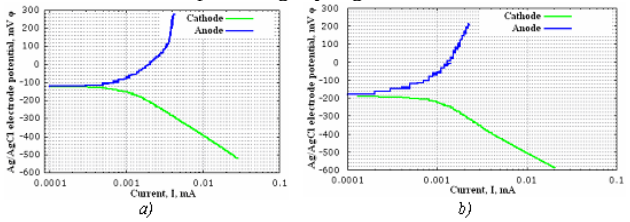

Fig. 7. Polarization curves for CP Ti: *a)* – with a CG structure; *b)* – with a UFG structure

The cathodic reaction of hydrogen evolution runs with a smaller overpotential. Consequently, the process of titanium's corrosion in a weak acid electrolyte takes place with anodic control.

The corrosion currents determined by the extrapolation of the Tafel regions of the anodic and cathodic curves amount to 0.97 μA and 0.62 μA, respectively, for the CG and UFG samples. Thus, the corrosion current of the CG sample in a weak acid electrolyte is 1.56 times higher than the corrosion current of the UFG sample (see table 2).

Table 2. Corrosion currents

Sample	Corrosion current, μA
UFG	0.62
CG	0.97

The features of the corrosion behavior of CP Ti in the CG and UFG states may be associated with the self-passivation phenomenon. For instance, the perimeter of grain boundaries in the UFG sample is larger than the one in the CG sample, while the surface binding energy of atoms is lower. At the same time, on the surface there forms a continuous and thick oxide film due to a large amount of free enthalpy. As it can be seen in fig. 7, the equilibrium potentials of corrosion are more positive (-1.2 V) for the CG sample (Fig. 7, *a*) and less positive (-1.85 V) for the UFG sample (Fig. 7, *b*).

Proceeding from this, not taking into account the passivating properties of the oxide film on titanium, the CG sample is supposed to possess a lower corrosion activity than the UFG sample. However, as demonstrated by the analysis of polarization curves, the corrosion current of the CG sample is more than 1.5 times higher than the corosion current of the UFG sample. In this connection, one may assume that the properties of the forming oxide film have a significant effect on the corrosion properties of CP Ti.

The differences in the formation of oxide passivating layer on Ti can be indirectly observed in the last third of the anodic branch of the polarization curves, displayed in fig. 7. As it can be seen in Fig. 7, *a*, the induced current continues to become further saturated, also after the overpotential of 0.2 V, and remains practically unchanged with increasing potential; this may indicate the maximum ionization current of Ti in this electrolyte solution. In Fig. 7, *b* the linear region is less expressed, but after it ends, the titanium, with increasing potential, continues to dissolve with growing induced current, its values being smaller than the ones for the CG sample; this may indicate larger diffusion limitations for the anodic process, created by the oxide film, in UFG Ti as compared to CG Ti.

In addition to the corrosion tests performed according to the two above-described procedures, clarifying tests in a salt spray chamber were conducted as an alternative method.

3. Corrosion tests in a salt spray chamber

3.1. Experimental procedure

The tests were performed in accordance with the ASTM G31 standard [10] in vapor atmosphere in a salt spray chamber, its schematic diagram being shown in Fig. 8. The size of the tested samples from CP Ti with CG and UFG structures was 9 x 25 x 9 mm. The concentration of the NaCl salt solution was 3.5%. The duration of the experiment was 10 days.

Corrosion resistance was evaluated on the basis of weight loss. The weight loss was recorded in accordance with the requirements of the ASTM G1 standard [11]. The samples were weighed on an analytical balance after withdawal from a reservoir and careful washing in distilled water with a soft brush, followed by removal of water with filter paper.

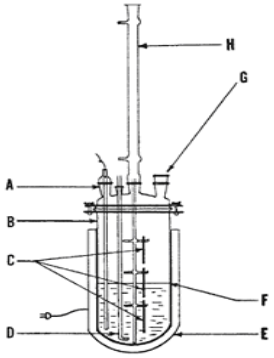

Fig. 8. Schematic diagram of the salt spray chamber. A – thermowell; B – reservoir with a solution; C – samples suspended on holders; D – air duct; E – reservoir heater; F – fluid surface; G – hole for the connection of the reservoir to an auxiliary device that may be required; H – reflux condenser.

The salt spray chamber is a reservoir that can be used as a universal and convenient apparatus for conducting simple corrosion tests. The configuration of the reservoir's upper portion is such that more complex devices can be added to it, depending on the specific test type.

3.2. Test results

The area of corrosion damage was estimated in accordance with the recommendations set forth in CNS8886 [12]. According to the quantitative evaluation, the larger is the score, the smaller is the corrosion area, and vice versa. The corrosion evaluation is presented in table 3.

Table 3. Corrosion area on the basis of the corresponding sorting [12]

Estimate of corrosion area, A (%)	Numerical score of corrosion damage (score points)
0.01	10
A ≤ 0.02	9.8
0.02 < A ≤ 0.05	9.5
0.05 < A ≤0.07	9.3
0.07 < A ≤ 0.10	9
0.10 < A ≤ 0.25	8
0.25 < A ≤ 0.50	7
0.50 < A ≤ 1.00	6
1.0 < A ≤ 2.5	5
2.5 < A ≤ 5	4
5 < A ≤ 10	3
10 < A ≤ 25	2
25 < A ≤ 50	1
50 < A	0

Fig. 9 shows the appearance of CP Ti samples with a coarse-grained microstructure after corrosion tests in a salt spray chamber.

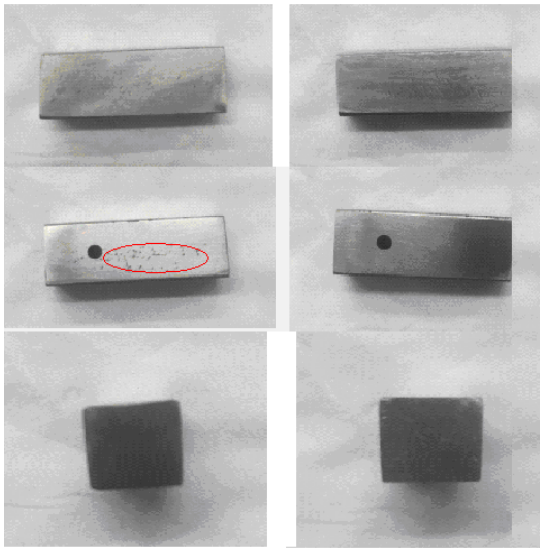

Fig. 9. Appearance of the samples with a CG structure after corrosion tests

Fig. 10 shows the appearance of the CP Ti samples with an ultrafine-grained microstructure after corrosion tests in a salt spray chamber.

As it can be seen in Fig. 9, the corrosion damage of the samples with a CG structure is represented primarily by small, but densely spaced, point defects, as well as by rather extensive continuous areas. Apparently, such a difference is conditioned by a dissimilar surface preparation (polishing) prior to the experiment. In Fig. 10 visible are more extensive widely-spaced point defects, caused by corrosion damage. The most illustrative regions of corrosion damage are marked in red on the samples with different microstructures.

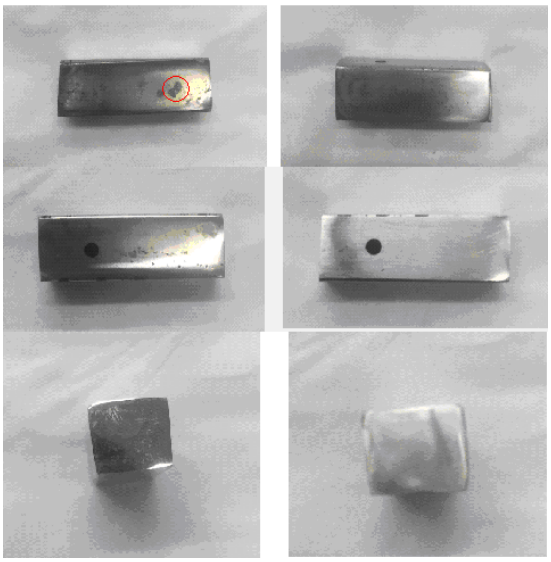

Fig. 10. Appearance of the samples with a UFG structure after corrosion tests

However, the weighing of the samples prior to and after the corrosion tests reveals that the weight loss for the material with a CG structure is much larger than the weight loss for the samples with a UFG structure.

Table 4 presents the experimental results of corrosion tests.

Table 4. Experimental results

Sample weight, g	CG structure	UFG structure
Prior to the tests	8.274	8.524
After the tests	8.2397	8.5112
Weight loss, %	0.415	0.150
Area of corrosion damage according to Table 3	$0.07 < A \leq 0.10$	$0.05 < A \leq 0.07$
Corrosion damage score	8.2	9.3

Analysis of the table reveals that for CP Ti with a CG structure the corrosion damage under salt spray conditions is more than 2.5 times larger than the corrosion damage for the SPD-processed material with a UFG structure. This confirms the results obtained earlier.

Fig. 11 shows an electronic image of a corrosion damage region on the surface of CP Ti with a UFG structure, together with chemical analysis data.

Table 5 presents the chemical compositions corresponding to the spectra shown in fig. 11.

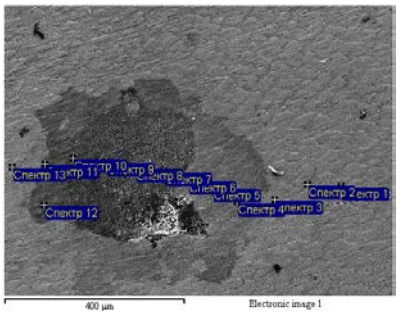

Fig. 11. Image of a corrosion damage region for the material with a UFG structure.

Table 5. Analysis of the chemical composition of the corrosion spot for CP Ti with a UFG structure.

Spectrum	O	F	Na	Si	K	Ca	Ti	Fe
Spectrum 1							100.00	
Spectrum 2							96.85	
Spectrum 3							100.00	
Spectrum 4	24.87		0.33				74.80	
Spectrum 5	25.51						74.49	
Spectrum 6	20.30	0.82	0.31				76.35	
Spectrum 7	23.00	1.18	0.79		0.28		74.75	
Spectrum 8	28.91	0.79	1.02	0.33	0.24	0.37	68.00	0.33
Spectrum 9	27.96	1.57	0.94				69.53	
Spectrum 10	25.64	0.99	0.42			0.20	68.47	0.29
Spectrum 11	26.92						70.70	

Spectrum 12	23.82		0.32				72.61	
Spectrum 13	15.85						81.01	
Max.	28.91	1.57	1.02	0.33	0.28	0.37	100.00	0.33
Min.	15.85	0.79	0.31	0.33	0.24	0.20	68.00	0.29

Proceeding from the above, the following factors can be mentioned that influence the corrosion behavior of CP Ti: grain size, the oxide film thickness, composition and continuity, electrolyte composition.

Conclusions

1. The type of the used coating (applied by ion plasma spraying or microarc oxidation) has practically no effect on the corrosion damage value of CP Ti samples.
2. The studied material (CP Ti) without coating in the ultrafine-grained state after SPD processing has a much smaller degree of corrosion damage, approximately 3 times smaller, as compared to the initial (as-annealed) state having a coarse-grained structure.
3. For the studied material with a UFG structure, a much lower corrosion rate is revealed in a 3.5% aqueous solution of sodium chloride in the observed time interval.
4. It has been estalished that the corrosion currents of CP Ti in the CG and UFG states in a weak-acid chloride electrolyte are different. The smaller is the grain size, the smaller is the corrosion current, which may be related to the self-passivation phenomenon and the regularities in the growth and structure of oxide films.
5. The corrosion behavior of CP Ti is influenced by grain size, oxide film composition and continuity, electrolyte composition.

ACKNOWLEDGEMENTS

The authors gratefully acknowledge the financial support under the joint Russian-Taiwanese research project RFBR No. 15-58-52015 HHC_a and MOST No. 104-2923-E-011-003-MY3.

REFERENCES:

[1]. R.Z. Valiev, A.P. Zhilyaev, T.G. Langdon, Bulk Nanostructured Materials: Fundamentals and Applications, 2014 by John Wiley & Sons, Inc., 456 pages.

[2]. R.Z. Valiev, Fabrication of nanostructured metals and alloys with unique properties by means of severe plastic deformation techniques. Rossiiskie Nanotekhnologii, 2006, Vol. 1, Nos. 1-2, pp. 208-216 (in Russian).

[3]. G.I. Raab, R.Z. Valiev, Equal-channel angular pressing of long-length billets. Izvestiya Vuzov. Tsvetnaya Metallurgiya, 2000, No. 5, pp.50-53 (in Russian).

[4]. Sergueeva, A.V., Stolyarov, V.V., Valiev, R.Z., Mukherjee, A.K. Advanced mechanical properties of pure titanium with ultra-fine grained structure//Scripta Materialia (2001), 45, 747–752.

[5]. N.A. Amirhanova, A.F. Razyapova, Investigation of Corrosion Properties St.3 in Coarse-Grained and Ultra Fine-Grained Conditions//Book of Abstracts on the International Symposium «Bulk Nanostructured Materials: from fundamentals to innovations» (BNM-2007), Ufa, 2007, p. 166.

[6]. G.I. Raab, V.I. Semenov, N.V. Savel'eva, E.F. Mustafina, Influence of thermo-mechanical treatment on structure and corrosion properties of carbon steels //Forging and Stamping Production. Material Working by Pressure. 2008. No. 12. pp. 34 – 36 (in Russian).

[7]. Chuan Ting Wang, Nong Gao, Mark G. Gee, et al. Processing of an ultrafine-grained titanium by high-pressure torsion: An evaluation of the wear properties with and without a TiN coating//Journal of the Mechanical Behavior of Biomedical Materials 17 (2013) pp. 166–175.

[8]. Chuan Ting Wang, Nong Gao, Mark G. Gee, et al. Tribology testing of ultrafine-grained Ti processed by high-pressure torsion with subsequent coating//J. Mater. Sci., Vol. 48, No. 13 (2013), pp. 4742-4748.

[9]. Chuan Ting Wang, Ana Escudeiro, Tomas Polcar et al. Indentation and scratch testing of DLC-Zr coatings on ultrafine-grained titanium processed by high-pressure torsion// Wear, Vol. 306, Nos. 1-2 (2013) pp. 304-310.

[10]. ASTM G31-72 (Reapproved 1999): Standard Practice for Laboratory Immersion Corrosion Testing of Metals, ASTM International.

[11]. ASTM G1-90 (Reapproved 1999): Standard Practice for Preparing, Cleaning, and Evaluating Corrosion Test Specimens, ASTM International.

[12]. Methods of Salt Spray Testing CNS8886, Bureau of Standards, Metrology & Inspection, M. O. E. A., R. O. C., 2002.

MICROALLOYED STEEL UNDER TENSION AND BENDING CONDITION

Doc. Ing. PhD. Mihaliková M. [1], Ing. Lišková A. [1], Ing. PhD. Elena Čižmárová E. [2]
Faculty of Metallurgy, Technical University in Košice, the Slovak Republic [1]
Czech Technical University in Prague, Faculty of Mechanical Engineering, the Czech Republic [2]

E-mail: maria.mihalikova@tuke.sk, anna.liskova@tuke.sk, elena.cizmarova@fs.cvut.cz

Abstract: *The article deals with the influence of the loading rate in the interval from 1 to 1000 mm/min on the mechanical properties of drawing steel sheet, used for the manufacture of automotive parts, under tension and bending conditions. It describes the aspects of material characteristics under tension and bending conditions, while bending tests were made on notched specimens (a modified impact bending test). With an increasing strain rate up to the critical value, the resistance of material against strain increases and hence the yield point and the tensile strength increase, the deformation ability, the deformation homogeneity, the structure and the substructure after deformation, etc. are changed. The paper presents knowledge that using a modified notch toughness test it is possible to achieve the formability characteristics corresponding to dynamic strain rates even under the static loading.*

Keywords: MICROALLOYED STEEL, MECHANICAL PROPERTIES, DRAWING STEEL SHEET, BENDING, STRAIN RATE, PRESSABILITY CHARACTERISTICS

1. Introduction

The influence of the strain rate on the material characteristics is systematically observed and the knowledge is generalized. With an increasing strain rate up to the critical value, the resistance of material against plastic strain increases and hence the yield point and the tensile strength increase, the deformation ability, the deformation homogeneity, the structure and the substructure after deformation, etc. are changed. At a supercritical strain rate, which is higher than the maximum dislocation movement rate, a brittle failure occurs [1-4]. The sensitivity of steel to the strain rate depends on its structure; therefore it is necessary to assess the sensitivity of individual steel grades to the strain rate [5]. The experimental determination of the influence of the strain rate on mechanical properties, as well as the interpretation of obtained results, is very demanding even today. Possibilities of replacing the tensile test at various strain rates with simpler tests are looked for. The notch toughness test, with a certain modification, can be included among such tests [6 - 8].

The increase of the production rate of pressings enables the productivity increase. This route is the most utilized nowadays and the strain rates are gradually approaching to rates corresponding to dynamic loading.

2. Material and Experimental procedures

Experiments were made on light-gauge steel strip with the gauge of 1 mm, made of galvanized microalloyed steel. Such steel strips have higher strength properties, but also good plasticity even at a low carbon content, due to microalloying with (Nb<0.008%) and Ti (Ti<0.01%) combined with controlled hot rolling, and they are used to manufacture loaded pressings for the automotive industry Table 1. The microstructure of the tested sheet consists of the ferritic matrix (see Fig. 1), in which the precipitates of microalloying elements are uniformly distributed.

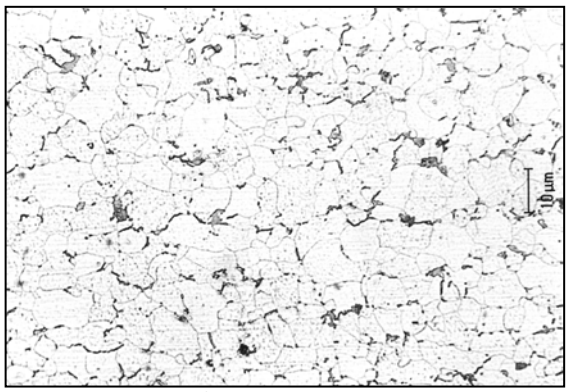

Fig. 1 *Microstructure of microalloyed steel.*

Table 1: *Chemical composition of tested steels*

%	C	Mn	Si	P	S	Al	Nb	Ti	V
steel	0,12	1,0	0,04	0,025	0,01	0,01	0,008	0,01	0,1

Samples were taken from the strip in the rolling direction and flat test specimens for the tensile test and test specimens for the modified bending test were made, (see Fig. 2 and Fig. 3).

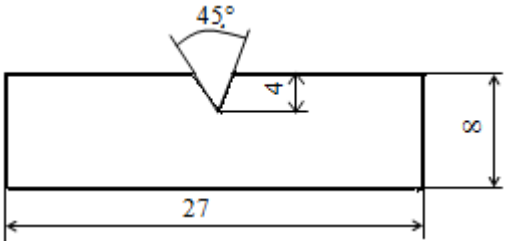

Fig. 2 *Shape and dimensions of the modified bending test (modified notch toughness test) specimen.*

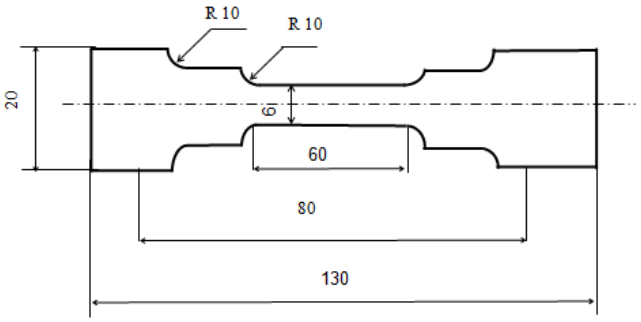

Fig. 3 *Shape and dimensions of the tensile test specimen.*

On the tensile machine INSTRON 1185, which makes it possible to record the loading diagram on a computer via a converter, tensile tests were carried out and using a fixture also modified bending tests (notch toughness test) were carried out (see Fig. 4). The distance of supports is in the modified. Bending test was 27 mm; the mandrel shape was identical with the of the Charpy hammer mandrel. The depth of the V notch was 0.5 x

Fig. 4 *Modified bending tests (notch toughness test).*

specimen height. The tests were carried out at four loading rates, namely 1, 10, 100 and 1000 mm/min. The following mechanical properties were evaluated: yield point, tensile strength, yield point in bending, ultimate bending strength, strain hardening exponent and stable plastic strain deflection (deflection from the force at the yield point up to the maximum bending force). These mechanical properties make it possible to determine basic characteristics for the assessment of the press ability of the tested sheet at selected loading rates. Table 2 shows mechanical properties microalloyed steel in static condition.

Table 2: *Mechanical properties of tested material in static condition.*

	Microalloyed steel
Thickness [mm]	1
Yield strength R_m [MPa]	410
Proof stress $R_{p0,2}$ [MPa]	340
Contraction A_5 [%]	20
Ductility Z [%]	49

3. Results and Discussions

3.1 Mechanical properties

The experimental results of the influence of the loading rate on the observed mechanical properties using the tensile test and the

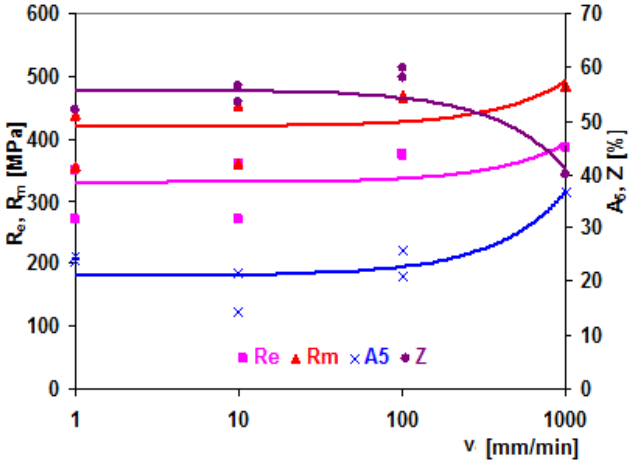

bending test (modified notch toughness test) are shown in Figure 5.

Fig. 5 *Dependence of mechanical properties on the loading rate in the tensile test*

The results show that the strength properties of the tested steel strip increase with an increasing loading rate (Fig. 5).

The influence of the loading rate on the yield point R_e and the tensile strength R_m in the tensile test can be described using the following formula (1) [9,10]:

$$R_V = R_{vo} + k.\log v/v_o \qquad (1)$$

Where:

-R_v is the yield point or the tensile strength at the loading rate v

-R_{vo} is the yield point or the tensile strength at the loading rate $v_o = 1.67.10^{-5}s^{-1}$

-**k** is a material constant expressing the sensitivity of the tested steel to the loading rate.

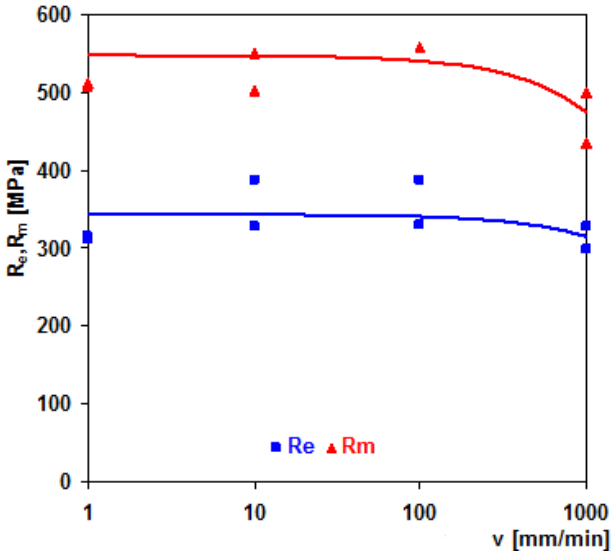

Fig. 6 *Dependence of mechanical properties on the loading rate in the modified bending test.*

Fig. 6 shows that in the modified bending test the course of the R_{eo}, R_{mo} – loading rate relationship is exponential, which means that the strain rate ε in this test is higher than 1 s^{-1}. Using calculations and microscopic measurements, the deformed area in the notch was determined and then the strain rate in the notch was calculated.

The relationship between the loading rate and the yield point in bending R_{eo} and the ultimate bending strength R_{mo} in the modified bending test is different from the tensile test and can be described as follows formula (2, 3) [9 -11]:

$$R\varepsilon = R\varepsilon + k.\log(\varepsilon/\varepsilon_o) \qquad (2)$$

at the strain rate up to 1 s^{-1}, and

$$R_\varepsilon = R\varepsilon + k.\log(\varepsilon/\varepsilon_o)^n \qquad (3)$$

at the strain rate from 1 to 10^2 s^{-1}.

One-way load of the material with a higher mechanical tension than a certain limit value causes the breakdown of the breakage and its gradual growth until the cohesion of the material, the parts of which are separated to form new free surfaces - fracture surfaces

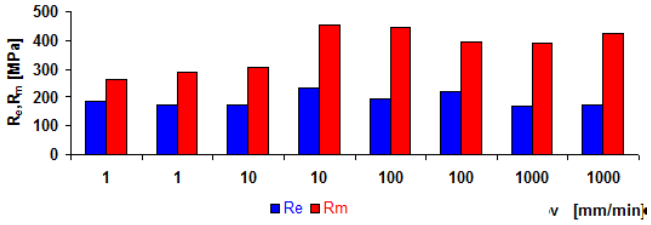

Fig. 7 *Dependence Re, Rm, from the load speed at modified bend test*

3.2 Fracture Analyses

In the fracture areas, we see a gradual, asynchronous loss of interatomic bonds under the effect of shear stresses. It is realized by skid movement of dislocations. The tested microalloyed steel is a ductile violation that arises from a hollow mechanism. Hole morphology is the result of a ductile material fracture

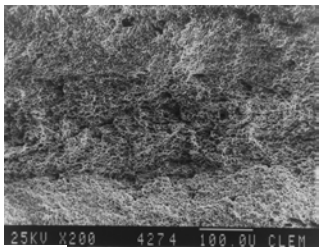

Fig. 8 *Fracture area at a load speed of 1mm/min 200x*

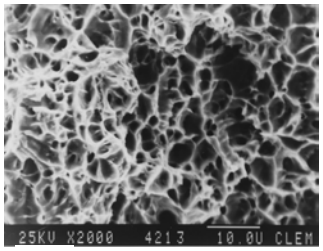

Fig. 9 *Fracture area at a load speed of 1mm/min 2 000x*

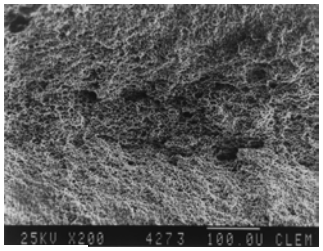

Fig. 10 *Fracture area at a load speed of 100 mm/min 200x*

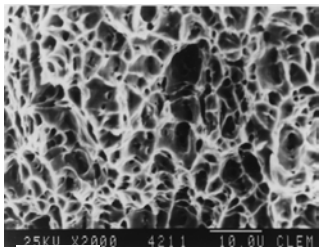

Fig. 11 *Fracture area at a load speed of 100mm/min 2 000x*

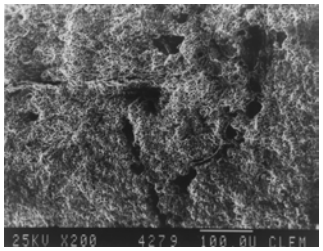

Fig. 12 *Fracture area at a load speed of 1000 mm/min 200x*

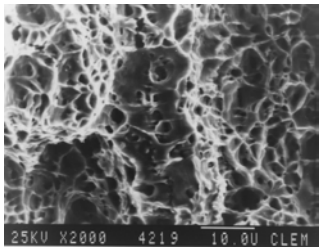

Fig. 13 *Fracture area at a load speed of 1000mm/min 2 000x*

Fig. 8, 9 at speeds 1 mm/min, the ductile fracture is an even morphological hole where the holes are deep. Cavity coalescence is visible in small magnifications. The fracture characteristic of (Fig. 10, 11) at a load speed of 100 mm / min is similar to that of 1 mm / min. More pronounced is the cavity coalescence in the direction perpendicular to the direction of the tension. At a load speed of 1 000 mm min, the angle of rupture is increased (Fig. 13), a fairly uneven surface is formed, the wells are smoother. (Fig. 12) we can see a large particle trap, because it did not manage to pass through the whole process of ductile morphology with a hole morphology.

At speeds load 1000 mm/min is visible indication (facets) intergranular ductile fracture.

The values of strength and plasticity properties determined using the modified bending test are, when compared with the tensile test, influenced by the loading method and the notch effect. This fact was taken into account in such a way that we put into line the values of the yield point and the strength values. A similar way was used for the strain hardening exponent n and the stable plastic strain deflection

On the basis of these considerations, Figure 5 shows the graph of the influence of the strain rate on the strength properties of the tested material in the tensile test and the modified bending test and Figure 7 shows the influence of the strain rate on the R_e/R_m ratio, the strain hardening exponent and the stable plastic strain deflection hr.

4. Conclusions

The paper analyses the influence of the loading rate ranging from 1 to 1000 mm/min on the mechanical properties of microalloyed steel under tension and modified bending conditions (modified notch toughness test). It results from the analysis that:

- the strain rate in the modified bending test is 2,3-times higher than that in the tensile test at the same loading rate, which means that using this test it is possible to determine material characteristics corresponding to dynamic strain rates at the static loading

- after making a correction resulting from the different loading and the notch effect, in the modified bending test it is possible to obtain the relationship between the material characteristics and the strain rate, corresponding to the uniaxial tension conditions

- with the increase of the strain rate in the interval from 100 to 1000 mm/min, the yield point and the yield point/strength ratio of the tested steel significantly increase.

- At the loading rates monitored, samples were broken by a ductile fracture, which is performed by a cavity mechanism. The result is the fracture morphology of the fracture surface. At 1000 mm / min load speeds, a hint of intercrystalline ductile violation is seen.

Load speed (1 to 1000 mm / min) affects strength and deformation characteristics only slightly, meaning that steel products can be formed at a high speed up to 1000 mm / min. This fact means shortening the production cycle and thus increasing the financial benefits.

5. Acknowledgement

This work has been supported by scientific grant. No VEGA 1/0549/14 and Ministry of Education, Youth and Sport of the Czech Republic, program NPU1, project No LO1207.

6. References

[1] Zubko P., Vojtko M., Pešek L., Német M., Bekeč P., Changes in mechanical properties and microstructure after quasi-static and dynamic tensile loading . Materials Science Forum, 782 (2014), 215-218.

[2] Suliga M., The influence of the high speed multipass drawing process on the fatigue strength of high carbon steel wires. Archives of Metallurgy and Materials 57 (2012) 4, 1171-1178.
[3] Pham M.S., Solenthaler C., Janssen K.G.F., Holdsworth S.R. Structure evolution and its effects on cyclic deformation response of AISI 316L stainless steel . Mater. Sci. Eng. A 3261 (2011), 3261-3269.
[4] Evin E. Tomáš, M. et al., The Deformation Properties of High Strength Steel Sheets for Auto-body Components. Procedia Engineering, 69, (2014), 758- 767.
[5] Hadasik E. et al., Rheological model for simulation of hot rolling of new generation steel strip for automotive application. Steel Research International 77 (2006), 12, 927-933.
[6] Mihaliková M., Német M., Increments of plastic strain and hardness HV10 of automotive steels sheets. Metalurgija 51 (2012) 4, 449-452.
[7] EN ISO 6892-1: 2009: Metallic materials. Tensile testing.
[8] EN ISO 148-1:2009 Metallic materials - Charpy pendulum impact test.
[9] Michel, J., Buršák, M., The influence of strain rate on the plasticity of steel sheets. Komunikacie 12 (2010), 4, 27-32.
[10] Buršák, M., Mamuzić, I., Michel', J., Contribution to evaluation of mechanical properties during impact loading. Metalurgija 47 (2008), 1, 19-23.
[11] Mihaliková M., Német M., Vojtko M., Impact of strain rate on microalloyed steel sheet fracturing, Acta Polytechnica, 54 (2014) 281-284.

FINITE ELEMENT MODELING OF INCREMENTAL SHEET METAL FORMING OF ALUMINUM ALLOY AL 1100

Samad Nadimi Bavil Oliaei, PhD.[1]*, Mahmoudreza Eivazzadeh, M.Sc.[2], Samad Dadvandipour, PhD.[3]
Department of Mechanical Engineering, Kizilcasar Mahallesi, Incek, Golbasi, Ankara, Turkey [1]
University of Science and Research Branch of Tehran, Iran [2]
Institute of Information Science, Faculty of Mechanical Engineering and Informatics, University of Miskolc-HUNGARY [3]

samad.nadimi@atilim.edu.tr, eivazzadeh.m.r@gmail.com, aitsamad@uni-miskolc.hu

Abstract: *Incremental sheet metal forming has been well-known as one of the flexible methods of forming metallic sheets, suitable for the production of prototypes or small batch sizes. Apprehending the deformation method in forming processes and selection of route parameters to avoid part failure are of vital importance, because marketing needs standard sound parts in a shortest possible time. This paper presents the study on the use of finite element modeling of incremental sheet metal forming of Al 1100 aluminum alloy to investigate the effect of tool diameter and step over on the forming induced stresses, part thickness distribution and forming forces. The results of finite element analysis are compared with experimental data while producing truncated pyramid parts. It has been shown that the developed finite element model is capable of providing reliable results in the prediction of the final thickness of the part, which matches the experimental results with a maximum discrepancy of 8%.*

Keywords: ALUMINUM ALLOY, INCREMENTAL FORMING, FINITE ELEMENT METHOD, FORMABILITY

1. Introduction

In sheet metal forming industry, the mass production of different parts is usually done by using accurate but expensive punches and dies. In mass production, because of the large quantities of the produced parts, the cost per part becomes significantly small, which makes these processes economically feasible for sheet metal forming industry. However, when small batch sizes or prototypes are required, the cost per part increases drastically. This increased cost makes the conventional methods based on dies and punches not feasible anymore. Therefore, it is necessary to develop and implement new developing techniques to satisfy the requirements imposed by the small batch production industries[1]. Incremental sheet forming (ISF), which originates from hybridization of stretch forming and conventional spinning processes[2], can be considered as a plastic forming process which meets the requirements of individual part or small-batch production, enabling the manufacturing of the desired shape through an incremental localized deformation[3].

In ISF process, the forming of a metal sheet is performed using the movements of a CNC controlled hemispherical head tool, which plastically deforms the blank according to a predefined path. The tool path generated with computer aided manufacturing (CAM) software, makes it possible to obtain complex geometries using a simply shaped tool[1,4,5]. In addition to eliminating a need for sophisticated forming tools, ISF results in an increased forming limit compared to pressing process[4]. Due to its unique advantages such as flexibility, cost effectiveness as well as reduced time-to-market and increased forming limit, ISF has gained a substantial attention from academia and industry as an important research area. According to Jackson & Allwood[4], and Jeswiet et al.[5], the first industrial emergence of ISF which is also called “diless forming”, dates back to 1960s in the USA. This method has been patented by Roux[6] and Leszak[7], while academic research lagging behind industrial application began in the early 1990s in Japan.

Depending on the complexity and desired accuracy of the workpiece, several variations of ISF have been developed in the last decades. In general ISF process can be classified into three groups, i.e. Single-Point Incremental Forming (SPIF), Two-Point Incremental Forming (TPIF), and Hybrid Incremental Forming (HISF).

SPIF, which is the simplest form of ISF, uses a simple tool to form the sheet, without requiring any supporting tool or die. The idea of using a fixed tool as a support has been introduced by Matsubara in 2001[8], where a very straightforward and compact tooling is devised and put on the bed of a CNC machine acting as a support during the forming process. The method which later called as TPIF has been successfully used in the forming of an aluminum sheet into cones and pyramids having an arbitrary number of sides with a minimum half-apex angle of 10°. The TPIF process may use a partial die or a full die. It should be mentioned that due to the reduced forming forces of ISF, it is possible to use soft materials such as plastics as partial or full dies, which can easily be produced by 3D printing techniques[9]. The term Asymmetric Incremental Forming (ASIF) is used to refer to both SPIF and TPIF[5].

Due to the unique advantages of ASIF, recently extensive researches are done to understand the mechanism of forming of ASFI and its potential applications for the fabrication of either prototypes or functional parts. The studies in the literature are mostly concentrated on three important quality measures of the process, namely geometric accuracy, surface quality and formability. Low part accuracy due to spring back and sheet bending has been considered as a limiting factor for the industrial application of ASIF[10], which is directly affected by the tool path generated by CAM software.

Finite element method has been used as an indispensable tool by several researchers to study ISF process. Cerro et al.[1] used FEM modeling of the ISF process of Al 1050-0 sheets during forming of pyramids with a 75° wall angle using the ABAQUS/Explicit software with shell elements. They reported a maximum difference of 5% between the peak values of the measured and predicted forming forces in the Z direction. The compromise between speed and accuracy of SPIF has been investigated by Yamashita et al.[11] using a dynamic explicit finite element code DYNA3D in forming quadrangular pyramids. The TPIF with full die has been studied by Attanasio et al.[12] to understand the effect of tool path type, step depth and scallop values on manufactured part characteristics. They investigated the surface quality, thickness distribution and geometric accuracy of a door handle of a commercial car made of FeP04 steel with a thickness of 0.7 mm. Their results showed that step depth and scallop height significantly influence the characteristics of the manufactured parts. They also presented some preliminary FEM simulations.

In the present paper, deformation behavior of Al 1100 aluminum alloy sheet metal in a single point incremental forming process (SPIF) is numerically simulated using ANSYS software. The effect of tool diameter and step over on the forming induced stresses; part thickness distribution and forming forces are

investigated. The results of finite element analysis are compared with experimental data while producing truncated pyramid parts.

2. Materials and Methods

In this study, SPIF of Al 1100 aluminum alloy is well-thought-out. Before conducting SPIF tests, the material properties are obtained using a standard uniaxial tensile test. An annealing process is carried out in the samples at 380 °C for 90 minutes. Fig. 1, illustrates the stress-strain curve for Al 1100 aluminum alloy. The material properties of this alloy are shown in Table 1.

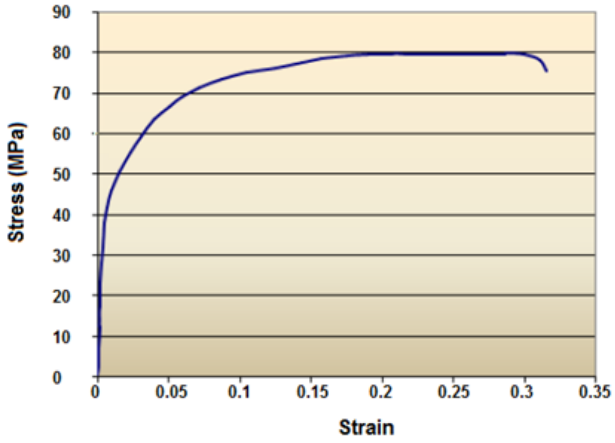

Fig. 1 *Stress-strain curve for aluminum alloy Al 1100*

Table 1: *Material properties of aluminum alloy Al 1100*

Elastic Modulus (GPa)	Poisson's Ratio	Yield Strength (MPa)	Ultimate Tensile Strength (MPa)	Elongation %
84	0.33	41	79.7	31.8

To do single point incremental forming, aluminum sheets with dimensions of 150×150×1 mm are prepared. A forming tool with a diameter of 10 mm with a hemispherical head is fabricated from a Stellite (cobalt-chromium alloy) with a hardness of 54 HRC and mounted on a CNC milling machine (FP4MK-MST). The hemispherical part of the forming tool has been ground and polished to reduce the friction. The aluminum sheet is fixed to the CNC milling machine using a dedicated fixture. Fig. 2 illustrates the forming tool and experimental setup used in this study. A CAM software is used to generate a tool path using parallel spiral outside-in strategy. The tool path is schematically shown in Fig. 3.

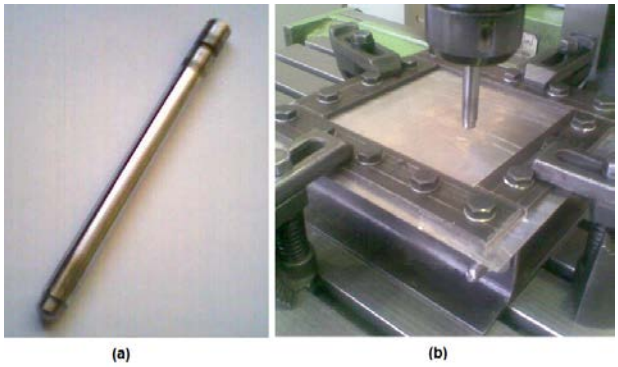

Fig. 2 *(a) Hemispherical tool, (b) Experimental Setup for SPIF*

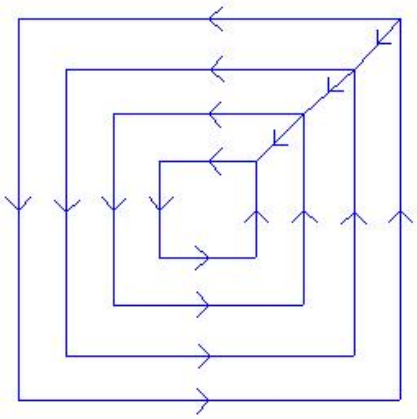

Fig. 3 *The tool path used in the incremental forming process*

The forming operations are performed at a feed rate of 60 mm/min with lubrication to reduce the friction and to avoid tool wear. The rotational speed is taken as 140 RPM. Fig. 4 illustrates a truncated pyramid part produced by SPIF process.

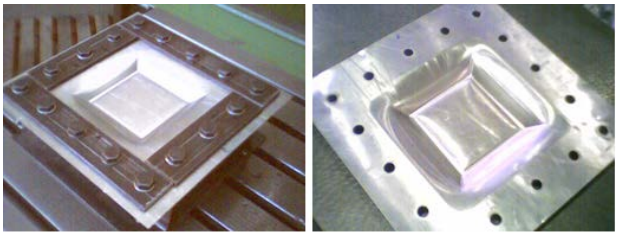

Fig. 4 *(a) Truncated pyramid part fabricated by SPIF process*

3. Finite Element Modeling of SPIF Process

In this study, finite element simulation of single point incremental sheet metal forming is performed using ANSYS software. The geometric model of SPIF process consists of four different parts, including forming tool, blank, blank holder and fixture as depicted in Fig. 5 (a). The fixture and blank holder are meshed using Solid 95 elements. The blank has been modeled using Visco Solid 107 element. The forming tool is modeled as an elastic body with a modulus of elasticity of 207 GPa. The meshed model of the assembly is shown in Fig. 5 (b).

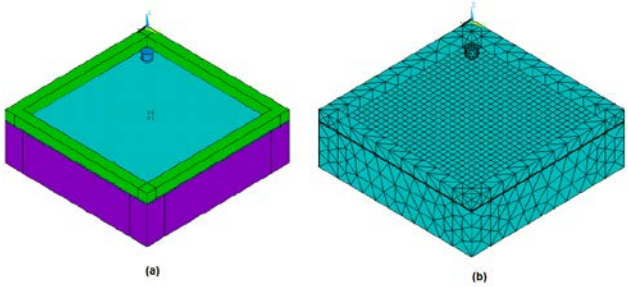

Fig. 5 *(a) Geometric model of the SPIF process, 5(b) Finite element model of the SPIF process*

A rigid-flexible surface-to-surface contact is defined using Target 170 and Contact 174 elements. Since in this process lubricant is used to reduce the friction between sheet and forming tool, a small Coulomb friction factor of 0.04 is used in the simulations. A step over of 10% of tool diameter is considered, meaning that after completing each loop the forming tool moves 1 mm from the current loop towards the center of the part to start the next loop. Fig. 6 illustrates the deformed shape of the sheet at the end of the simulation.

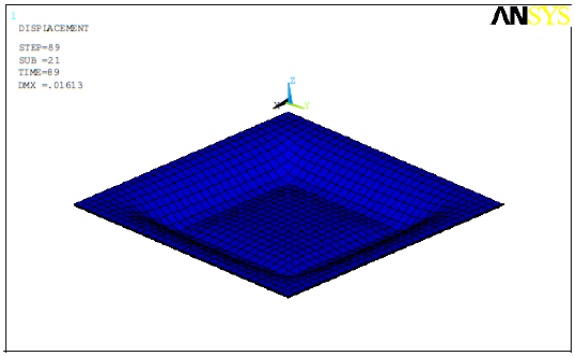

Fig. 6 *Deformed shape of the sheet after SPIF process*

The contours of von Mises stresses and strains are shown in Fig. 7 and Fig. 8, respectively. The results of simulations revealed that as the depth of part increases the level of stresses increases. The maximum stresses occur at the contact region between the forming tool and sheet during deformation.

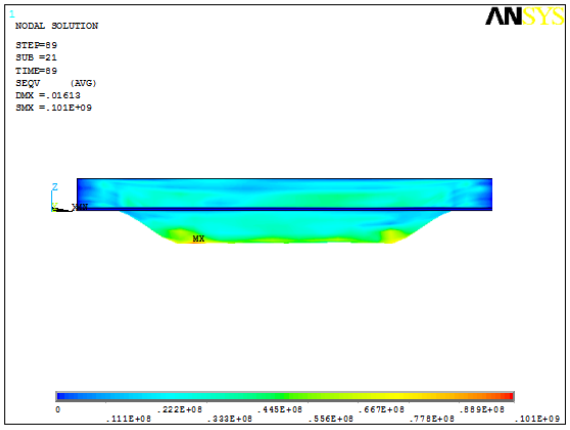

Fig. 7 *Forming induced von Mises stresses in SPIF process*

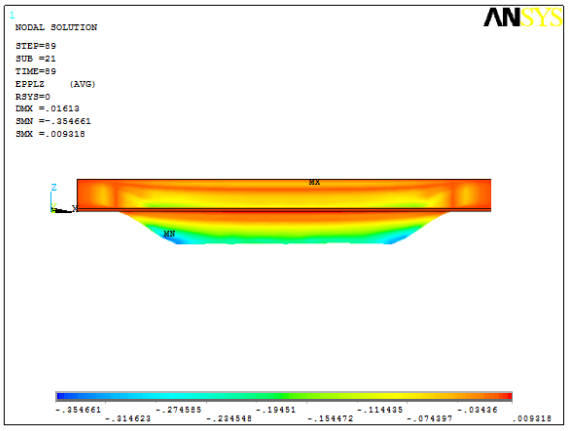

Fig. 8 *Forming induced strains in SPIF process*

The thickness of the part was measured at different positions to compare the results of simulations with experiments. Table 2 shows a comparison between experiments and finite element predictions. As is seen in Table 2, the minimum thickness in FEM predictions is about 0.65 mm, while it is 0.7 mm in experimental one, which shows the capability of the FEM model in the prediction of thickness reduction with a maximum error of 8%.

Table 2: *Measured thicknesses vs. calculated thicknesses*

Thickness FEM [mm]	0.65	0.73	0.81	0.89	0.97	0.99
Thickness Exp. [mm]	0.7	0.77	0.84	0.91	0.96	1

4. Analysis of the Effect of Forming Tool Diameter

The SPIF process was simulated with hemispherical head forming tools having three different diameters of 7 mm, 10 mm and 13 mm to analyze the effect of forming tool diameter in the incremental forming process. For each of forming tools, von Mises stresses, formed thickness and forming forces are obtained at a constant step over/outstep of 1 mm. The simulation results for each tool are shown in Table 3.

Table 3: *Results of simulations for different tool diameters*

Tool Dia. (mm)	Von Mises Stress (MPa)	Thickness (mm)	Maximum Forces (N)	
			F Feed	Fz
7	102	0.64	290	673
10	101	0.65	292	681
13	99	0.66	297	718

As it can be seen in Table 3, the increase in the forming tool diameter results in a decrease in the von Mises stresses and increase in the formed thickness of the workpiece. Therefore, we can conclude that with increasing forming tool diameter the possibility of failure reduces, which makes it possible to produce parts with larger depths. It can also be seen that, by increasing forming tool diameter both in-feed and in-depth forming forces increases.

5. Analysis of the Effect of Step Over

Step over is another important parameter which has a significant influence on the forming induced stresses and formability of the sheets during ISF process. In this study, the effect of step over on forming induced stresses and thickness reduction is considered. Two step over values of 10% and 20% are taken into account for a forming tool of 10 mm diameter, while other conditions are kept similar. The results revealed that by increasing step over from 10% to 20%, von Mises stresses increases from 101 MPa(Fig. 7) to 109 MPa (Fig. 9). The thickness of the part also reduced to 0.62 mm, meaning that as step over enlarges the formability of SIF decreases. Therefore, based on these results, in order to increase the formability, the step over values should be made as small as possible, however by selecting very small step over values, the processing time increases, which in turn reduces the productivity. Hence, the best compromise between step over and the process time is well-thought-out.

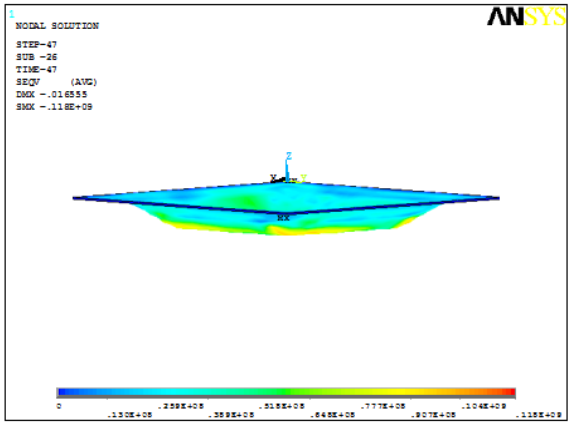

Fig. 9 *Analysis of the Effect of Step over process*

Conclusions

This paper aims at studying the use of finite element modeling of incremental sheet metal forming of Al 1100 aluminum alloy. To investigate the effect of some process parameters on residual stresses and part thickness distributions, the results of the finite element analysis are compared with experimental data while producing truncated pyramid shaped parts. It has been shown that the developed finite element model is capable of providing reliable results in the prediction of the final thickness of the parts, which matches the experimental data with a maximum discrepancy of 8%. The results of FE simulations revealed that with increasing forming tool diameter the possibility of failure reduces, which makes it possible to produce parts with larger depths. It has also found that by increasing forming tool diameter both in-feed and in-depth forming forces increases. The effect of step over on the formability of SPIF process of aluminum alloy Al 1100 has also studied. The results revealed that, as far as the productivity of the process is maintained, small step over values should be preferred to increase the formability and to reduce the forming induced stresses.

References

[1] I. Cerro, E. Maidagan, J. Arana, A. Rivero, and P. P. Rodriguez, "Theoretical and experimental analysis of the dieless incremental sheet forming process," *Journal of Materials Processing Technology*, vol. 177, no. 1, pp. 404-408, 2006.

[2] Y. Kumar and S. Kumar, "Incremental Sheet Forming (ISF)," *In Advances in Material Forming and Joining*, pp. 29-46, Springer India., 2015.

[3] T. J. Kim and D. Y. Yang, "Improvement of formability for the incremental sheet metal forming process," *International Journal of Mechanical Sciences*, vol. 42, no. 7, pp. 1271-1286, 2000.

[4] K. Jackson and J. Allwood, "The mechanics of incremental sheet forming," *Journal of materials processing technology*, vol. 209, no. 3, pp. 1158-1174.

[5] J. Jeswiet et al., "Asymmetric single point incremental forming of sheet metal," *CIRP Annals-Manufacturing Technology*, vol. 54, no. 2, pp. 88-114, 2005.

[6] P. Roux, *U.S. Patent No. 2,945,528. Washington, DC: U.S. Patent and Trademark Office.*, 1960.

[7] E. Leszak, *U.S. Patent No. 3,342,051. Washington, DC: U.S. Patent and Trademark Office.*, 1967.

[8] S. Matsubara, "A computer numerically controlled dieless incremental forming of a sheet metal," *Proceedings of the Institution of Mechanical Engineers, Part B: Journal of Engineering Manufacture*, vol. 215, no. 7, pp. 959-966, 2001.

[9] M. Amino, M. Mizoguchi, Y. Terauchi, and T. Maki, "Current Status of “Dieless” Amino's Incremental Forming," *Procedia Engineering*, vol. 81, pp. 54-62, 2014.

[10] H. Lu, M. Kearney, C. Wang, S. Liu, and P. A. Meehan, "Part accuracy improvement in two points incremental forming with a partial die using a model predictive control algorithm," *Precision Engineering*, 2017.

[11] M. Yamashita, M. Gotoh, and S. Y. Atsumi, "Numerical simulation of incremental forming of sheet metal," *Journal of materials processing technology*, vol. 199, no. 1, pp. 163-172, 2008.

[12] A. Attanasio, E. Ceretti, C. Giardini, and L. Mazzoni, "Asymmetric two points incremental forming: improving surface quality and geometric accuracy by tool path optimization," *Journal of materials processing technology*, vol. 197, no. 1, pp. 59-67, 2008.

[13] Y. H. Kim and J. J. Park, "Effect of process parameters on formability in incremental forming of sheet metal," *Journal of materials processing technology*, vol. 130, pp. 42-46, 2002.